UPM UNIVERSITI PUTRA MALAYSIA BERILMU BERBAKTI

PUTRA PERTANIAN UNTUK RAKYAT®

ISAMN 2025

9TH INTERNATIONAL SYMPOSIUM ON ADVANCED MATERIALS & NANOTECHNOLOGY

Proceeding

29 – 30 October 2025 I UPM, Serdang

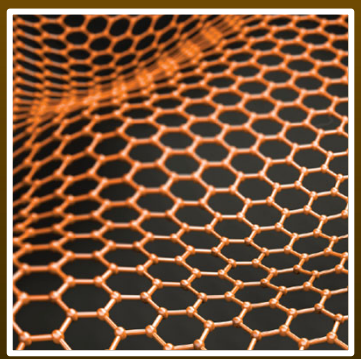

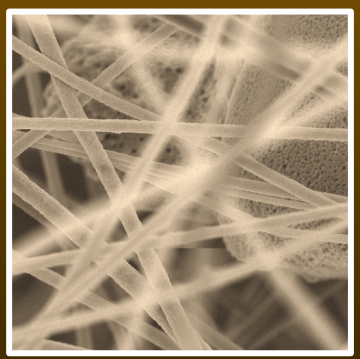

Theme:
Nanosciences for Sustainable and Inclusive Innovations for Planetary Well-being

Proceedings of 9th International Symposium on Advanced Materials and Nanotechnology

Publisher:

Institute of Nanoscience and Nanotechnology

Universiti Putra Malaysia

Vol. 1, 2025
eISSN : 2822-4655

@Universiti Putra Malaysia 2025

All rights reserved. No part of this e-proceeding maybe reproduced, stored in a retrieval system or transmitted in any form, or any means, electronic, mechanical, photocopying, recording or otherwise, without the prior permission of the copyright owner.

Chief Editor: Assoc. Prof. Dr. Mas Jaffri Masarudin
Editor: Dr. Rosnah Nawang
Mohd Ali Mat Nong

Publisher's address:
Institute of Nanoscience and Nanotechnology (ION2),
Universiti Putra Malaysia
43400 UPM Serdang
Malaysia

TABLE OF CONTENT

Proceeding of the 9th International Symposium on Advanced Materials and Nanotechnology (iSAMN2025), October 29-30, 2025

RF Magnetron Sputtered Aluminum Nitride Thin Films: Synthesis, Crystalline Quality, and Surface Characteristics

Zharah **Zapanta**[1,*], Hamdi Muhyuddin **Barra**[1,*], Sunny John **Lood**[1], Clarisse Jade **Estrada**[2], Soo Kien **Chen**[3], Johnny Jim **Ouano**[1], Florencio **Recoleto** Jr.[1], Arnel **Salvador**[4]

[1]Department of Physics, College of Natural Sciences and Mathematics, Mindanao State University – Main Campus, Marawi City, 9700, Philippines
[2]Department of Industrial Technology, North Eastern Mindanao State University, Cantilan, 8317, Philippines
[3]Department of Physics, Faculty of Science, Universiti Putra Malaysia, 43400 UPM Serdang, Selangor, Malaysia
[4]National Institute of Physics, College of Science, University of the Philippines, Diliman, Quezon City, 1101, Philippines Correspondence: hamdimuhyuddin.barra@msumain.edu.ph

*Corresponding author's phone: +639-557431631
E-mail: hamdimuhyuddin.barra@msumain.edu.ph
zapanta.zm58@s.msumain.edu.ph

Received: 13 November 2025; Accepted: 6 December 2025

ABSTRACT

Aluminum nitride (AlN) is a highly promising material due to its exceptional thermal, chemical, and piezoelectric properties, making it valuable for advanced applications such as optoelectronics, high-power electronics, and sensing technologies. When synthesized as a thin film, its crystalline quality and surface characteristics are significantly influenced by deposition parameters. Therefore, this study examines the effect of radio frequency (RF) power on the growth behavior of AlN thin films prepared using RF magnetron sputtering. The films were deposited on silicon (Si) substrates under RF powers of 100 W, 125 W, and 150 W. X-ray diffraction (XRD) results confirmed the presence of AlN (100) and (333) orientations. The diffraction peaks exhibited the highest intensity at 125 W, but decreased at 150 W. However, the full width at half maximum (FWHM) reached its minimum value of 0.031 at 150 W. Furthermore, atomic force microscopy (AFM) analysis revealed that surface roughness decreased with the highest RF power and displayed the smoothest morphology, with an RMS roughness (R_q) of 4.13 nm and an average roughness (R_a) of 2.18 nm.

Keywords— aluminum nitride, atomic force microscopy, rf magnetron sputtering, thin film, X-ray diffraction

1. INTRODUCTION

Aluminum nitride (AlN) thin films have attracted significant attention due to their wide range of applications in UV detectors and emitters[1,2], surface acoustic wave (SAW) devices, laser diodes, optoelectronic components, RF MEMS, and piezoelectric devices[3,4]. This growing interest arises from AlN's remarkable properties and its substantial contributions to these technologies over the past decades. Hence, AlN features a wide bandgap (6.2 eV), high film resistivity (~10^{15} Ω·cm), excellent thermal conductivity (up to 3.3 $W \cdot cm^{-1} \cdot K^{-1}$)[5], high breakdown field strength (≈5 $MV \cdot cm^{-1}$), low thermal expansion coefficient, and strong thermal stability[5–7]. In addition, its piezoelectric characteristics further enhance its versatility[8]. The performance of AlN thin

films is largely determined by their crystalline orientation, crystalline quality, and surface morphology, both of which are strongly influenced by the sputtering parameters used during deposition[9].

The fabrication of thin films can be achieved through various deposition techniques, including molecular beam epitaxy (MBE), dual ion beam sputtering (DIBS), metal–organic chemical vapor deposition (MOCVD), reactive evaporation, halide vapor phase epitaxy, and DC or RF magnetron sputtering. Among these methods, RF magnetron sputtering has been identified as one of the effective for synthesizing AlN thin films, offering high crystalline orientation, surface smoothness, and strong film adhesion.[9,10]

In this work, we focus on the optimization of AlN thin film growth via RF magnetron sputtering, highlighting the influence of RF power on its crystalline quality and surface characteristics, as the RF power has a significant impact on the mobility of adatoms, particularly on secondary atoms[9,10]. In systematically varying the RF power during the deposition process, this study aimed to examine its effect on the films' crystallinity and surface morphology.

2. MATERIALS AND METHODS

AlN thin films were deposited on Si (100) substrates with a diameter of 50.8 mm via RF magnetron sputtering (VTR-151M/SRF, ULVAC) using a pure aluminum (Al) disk (ULVAC) as a target. Prior to deposition, the chamber, target, and substrate were thoroughly cleaned. Then, the Si substrate and Al target were placed inside the chamber with a target-to-substrate distance of 50 mm. A base pressure of 5×10^{-4} Pa was achieved using a turbomolecular pump to minimize contamination. Then, to remove surface impurities from the target, a 5-minute pre-sputtering process was performed under argon (Ar) plasma. The deposition was then carried out at a substrate temperature of 450 °C, a working pressure of 2 Pa, and a nitrogen gas concentration of 70% for 20 minutes. Three samples were prepared at varying RF powers of 100 W, 125 W, and 150 W.

The crystalline structure of the films was analyzed using X-ray diffraction (XRD, Malvern PANalytical Empyrean Series 3, Cu Kα radiation), while surface morphology was examined via atomic force microscopy (AFM, Dimension Edge, Bruker) in tapping mode over a 3.0 μm × 3.0 μm scan area.

3. RESULTS AND DISCUSSION

3.1 Crystalline Quality

The XRD patterns of the AlN thin films are presented in Fig. 1, along with their corresponding Miller indices (hkl). As shown, the diffractogram exhibits two prominent peaks located at 2θ values of 33.1° and 61.9°, corresponding to the (100) and (333) planes of AlN, respectively, based on the ICSD reference code 96-153-5441. The (100) plane indicates a hexagonal AlN phase with an a-axis orientation, while the (333) plane corresponds to a cubic AlN structure. Among the samples, the film deposited at 125 W exhibited the highest degree of orientation, as evidenced by the significant increase in the (100) peak intensity, from 58 to 1589, compared with that of the 100 W film. However, when the RF power was further increased to 150 W, the (100) peak intensity sharply decreased to 256.

Moreover, FWHM, crystallite size, and lattice strain of the AlN films are provided in Table 1. The FWHM value for the (100) plane reached its minimum of 0.031 at 150 W. Thus, it is important to note that crystalline quality cannot be solely evaluated based on peak intensity; rather, it is more accurately represented by the FWHM, supported by additional factors such as film thickness, deposition rate, and surface morphology[9]. Hence, the decrease of the FWHM at 150 W indicates improving local ordering and larger crystallite formation[11]; however, it

showed that the highest lattice strain at 150 W may result from high RF power, causing more internal stress on the film.

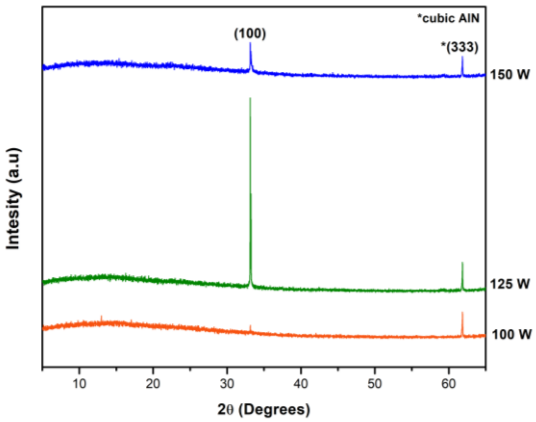

Fig. 1: X-ray diffraction patterns of AlN thin films deposited for different values of RF Power

Table 1: Structural parameters for the AlN films

Sample ID	hkl	FWHM (°)	D (nm)	Lattice strain (%)
AlN -1 (100 W)	100	0.0468	176.4	0.069
	333	0.0780	118.7	0.057
AlN -2 (125 W)	100	0.0468	177.1	0.069
	333	0.0780	118.7	0.057
AlN -3 (150 W)	100	0.0310	265.7	0.460
	333	0.0312	149.4	0.450

3.2 Surface Characteristics

The effect of RF power on the surface morphology of AlN thin films deposited on Si (100) substrates was analyzed using atomic force microscopy (AFM). Fig. 2 presents the two-dimensional AFM images of the AlN films at varying RF powers. A noticeable evolution in grain morphology was observed with increasing RF power. At 125 W, the film exhibited larger and more irregular grains, as clearly shown in Fig. 2b, whereas at 150 W, the grains became finer and more uniformly distributed, indicating an improvement in surface homogeneity (Fig. 2c).

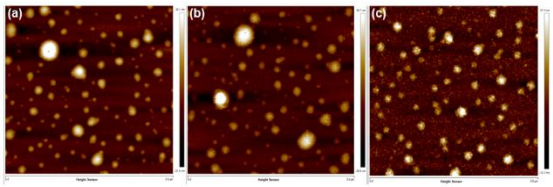

Fig. 2: 2D AFM images of the AlN thin films prepared at RF power of (a) 100 W, (b) 125 W, and (c) 150 W.

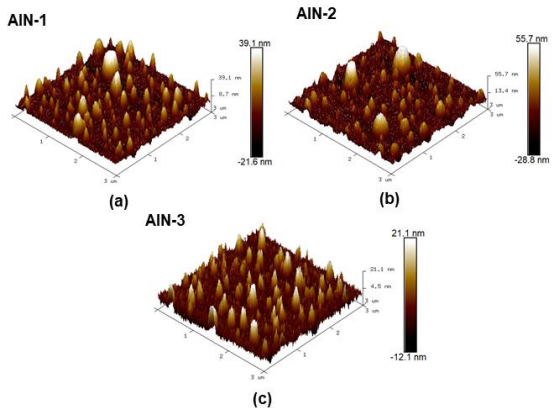

Fig. 3: 3D AFM images of the AlN thin films prepared at RF power of (a) 100 W, (b) 125 W, and (c) 150 W.

Quantitative surface parameters, including roughness and grain size, were obtained from AFM measurements and are summarized in Table 2. The root-mean-square (RMS) roughness values were 7.10, 9.80, and 4.13 nm, while the arithmetic mean roughness (Ra) values were 4.88, 6.17, and 2.81 nm for AlN-1, AlN-2, and AlN-3, respectively. These results reveal that surface roughness decreases markedly with increasing RF power, producing a smoother and denser film surface at 150 W. This reduction in roughness suggests enhanced adatom mobility and surface diffusion at higher RF power, promoting a more uniform and continuous film growth. Additionally, the average grain size decreased from 125 nm to 117 nm as the RF power increased, which can be attributed to higher nucleation rates and the coalescence of smaller grains under elevated energy input, resulting in a more compact and stable film structure.

Table 2. RMS roughness and grain size of AlN thin films influenced by RF Power

Sample ID	R_q (nm)	R_a (nm)	Grain size (nm)
AlN-1	7.71	4.88	125.143±52.877
AlN-2	9.80	6.17	124.694±66.177
AlN-3	4.13	2.81	117.838±31.657

4. CONCLUSION

A successful deposition of AlN thin film was achieved using the RF magnetron sputtering technique. In XRD analysis, it was confirmed the presence of two prominent orientations, namely (100) and (333) AlN planes. Hence, the diffraction intensity was strongest at 125 W but significantly decreased at 150 W, indicating a transition in the film's structural quality. Despite the reduction in overall crystallinity, the minimum FWHM value (0.031) obtained at 150 W suggests improved crystal alignment and the formation of larger coherent scattering domains. And the corresponding crystallite size also increased at 150 W, implying enhanced structural uniformity and improved ordering among the AlN grains. Additionally, AFM analysis further revealed decreased surface roughness, with Rq = 4.13 nm and Ra = 2.18 at 150 W, indicating a smoother film surface. Furthermore, the grain size was reduced to 117 nm at 150 W, signifying a denser and more compact surface morphology. Overall, higher RF power (150 W) improved surface smoothness and local crystallite growth, although it slightly compromised global crystallinity, suggesting an optimal trade-off between structural quality and surface uniformity.

ACKNOWLEDGEMENTS

The authors would like to thank **Mr. Earl Conan Casalme** of the National Institute of Physics, University of the Philippine - Diliman for carrying out the XRD analysis of the samples.

FUNDING

The authors acknowledge the support of the Commission on Higher Education and Philippine-California Advanced Research Institute (CHED-PCARI) under the LAKAS Program with project code LAKAS-2021-010

REFERENCES

(1) Ranacher, C.; Consani, C.; Tortschanoff, A.; Rauter, L.; Holzmann, D.; Fleury, C.; Stocker, G.; Fant, A.; Schaunig, H.; Irsigler, P.; Grille, T.; Jakoby, B. *Sensors (Switzerland)* **2019**, *19*, 2–11. doi:10.3390/s19112513

(2) Stewart, J. W.; Vella, J. H.; Li, W.; Fan, S.; Mikkelsen, M. H. *Nat. Mater.* **2020**, *19*, 158–162. doi:10.1038/s41563-019-0538-6

(3) Cimalla, V.; Pezoldt, J.; Ambacher, O. *J. Phys. D. Appl. Phys.* **2007**, *40*, 6386–6434. doi:10.1088/0022-3727/40/20/S19

(4) Aln, P.; Technology, C. M. **2010**, *19*, 570–580

(5) Claudel, A.; Chowanek, Y.; Blanquet, E.; Chaussende, D.; Boichot, R. **2021**, *2021*, 2019–2021. doi:10.1002/pssc.201000940

(6) Isarakorn, D.; Sambri, A.; Janphuang, P.; Briand, D.; Gariglio, S. **2010**, *055008*. doi:10.1088/0960-1317/20/5/055008

(7) Ruffnera, J. A.; Clema, P. G.; Tuttlea, B. A.; Dimosa, D. B.

(8) Meng, Y.; Chen, G.; Huang, M. *Nanomaterials* **2022**, *12*. doi:10.3390/nano12071171

(9) Iqbal, A.; Mohd-Yasin, F. *Sensors (Switzerland)* **2018**, *18*, 1–21. doi:10.3390/s18061797

(10) Sandeep, S.; Pinto, R. M. R.; Rudresh, J.; Gund, V.; Nagaraja, K. K.; Vinayakumar, K. B. *Crit. Rev. Solid State Mater. Sci.* **2025**, *50*, 161–188. doi:10.1080/10408436.2024.2406247

(11) Itoh, N.; Okamoto, K. **2011**, *1486*. doi:10.1063/1.339930

Effect of Zn Ion Concentration on Direct Heating Growth of ZnO Nanorods on Flexible Kanthal Mesh

Thi Anh **Le**[1], Thang Minh **Bui**[1], Diep Ngoc Le[1], Anh Van Thi **Le**[1], Dung My Thi **Dang**[1], Swee-Yong **Pung**[2*]

[1]Advanced Materials Technology Institute Vietnam National University Ho Chi Minh City, Viet Nam
[2]School of Materials and Mineral Resources Engineering, Engineering Campus, Universiti Sains Malaysia, Nibong Tebal 14300, Penang, Malaysia

*Corresponding author's phone: +60 13770 1308
E-mail: sypung@usm.my

Received: 30 September 2025; Accepted: 6 December 2025

ABSTRACT

This study aims to evaluate the effect of Zn^{2+} concentration on the growth of ZnO nanorods (NRs) on flexible Kanthal mesh (ZnO/mesh) via direct heating method. The morphology and structure of ZnO NRs were analyzed using Field Emission Scanning Electron Microscope and X-ray diffraction, respectively. Photocatalytic activity of ZnO/mesh was evaluated via the degradation of Rhodamine B dye. At an optimal concentration of 0.04 M, ZnO NRs with an average diameter of 87.6 nm completely covered the mesh surface. ZnO/mesh rapidly degraded 74.8% of RhB dye under UV light illumination. These finding highlight that precise control of Zn^{2+} ion concentration provides a simple and effective strategy to tailor the growth of ZnO nanorods on flexible substrates, paving the way for their potential applications in environmental remediation.

Keywords—ZnO nanorods; flexible, mesh, direct heating, photocatalytic

1.0 INTRODUCTION

Zinc oxide (ZnO) nanostructures have attracted significant attention due to their unique physical and chemical properties, making them promising candidates for diverse applications such as piezoelectric and triboelectric nanogenerators [1], photocatalysis [2], sensors [3], and optoelectronic devices [4]. In particular, the integration of ZnO nanorods (NRs) on flexible substrates enables the development of lightweight, bendable, and multifunctional devices suitable for next-generation technologies [5, 6]. For example, ZnO NRs grown on stainless steel meshes have been successfully employed in oxygen evolution [7].

Several synthesis methods have been reported for the growth of ZnO nanostructures on flexible substrates, including hydrothermal growth [8], chemical bath deposition [7], vapor-phase methods [9], and direct heating approaches [10]. Among these, the direct heating method provides a rapid, simple, and cost-effective route to synthesize nanomaterials directly on the substrate surface without the need for complex equipment [10, 11].

In wet chemical methods, such as hydrothermal, electrochemical and direct heating synthesis, controlling the zinc (Zn) precursor concentration plays a crucial role in determining the morphology, crystallinity, and density of ZnO nanostructures [12, 13]. Amin et al. [14] grew ZnO on silicon (100) substrates using

zinc nitrate hexahydrate and hexamethylenetetramine. They reported that Zn^{2+} concentration strongly influences morphology, yielding nanowires (<100 nm, ~1.2 μm long) at 10-25 mM, while >400 mM produces polycrystalline thin films instead of microrods. In another study, Lausecker et al. [15] varied the Zn^{2+} concentration from 1 to 100 mM, which led to pronounced morphological changes in ZnO nanowires on Au-coated silicon substrate, with the highest areal density (17.4 NW/μm^2) obtained at 50 mM.

Although the concentration effect has been widely investigated in solution-based growth techniques, fewer studies have focused on its role in the direct heating method. In this context, Zn precursor concentration may significantly influence the nucleation and growth of ZnO on resistive substrates during direct heating, thereby impacting the structural, and morphological characteristics of ZnO.

In this study, the effect of Zn^{2+} ion concentration on the growth of ZnO nanorods on Kanthal mesh using the direct heating was investigated. By tailoring precursor concentrations, the crystallinity, morphology, areal density, and surface coverage of ZnO NRs were systematically studied. Furthermore, the photocatalytic activity of the optimized ZnO/mesh system for Rhodamine B (RhB) dye degradation under UV light was evaluated, demonstrating the potential of this simple approach for environmental remediation.

2.0 MATERIALS

Zinc acetate dehydrate ($Zn(CH_3CO_2)_2 \cdot 2H_2O$) and sodium hydroxide (NaOH) were purcharsed from Merck. Rhodaminr B dye was purcharsed from Thermo Fisher. Ethanol 99.5% and Kanthan mesh was supplied by Chemsol and Vapour Tech, respectively.

3.0 EXPERIMENTAL

3.1 Synthesis of ZnO/mesh

Direct heating method was employed from our previous papers [10, 16] to synthesize ZnO nanorods. Generally, the Kanthal mesh was cut into 1x10 cm pieces and ultrasonically cleaned with ethanol for 5 min. The cleaned meshed was dried at 80 ℃ for 2 h before using.

ZnO nanorods were grown on Kantal mesh by fisrt immersing the mesh into the precursor solution of $Zn(CH_3CO_2)_2 \cdot 2H_2O$ and NaOH with different concentration of Zn^{2+} ion of 0.01, 0.02, 0.04 and 0.06 M. Then, the electrical power supply of 50 W was applied to both ends of the mesh. After heating for 8 min, ZnO NRs were grown on the mesh surface (ZnO/mesh), which were subsequently cleaned with distilled water and dried at 80 ℃ for 2 h.

3.2 Materials characterization

The morphology and structure of ZnO NRs were analyzed using Field Emission Scanning Electron Microscope (FESEM, SU8010, Hitachi) and X-ray diffraction (XRD, D8, Bruker), respectively. An average diameter, surface coverage, areal density of ZnO/mesh was analyzed using Image J software. The degradation of RhB dye was evaluated using Ultraviolet - Visible spectrometer (UV-VIS, Cary 100).

3.3 Photocatalytic study

Three ZnO/meshes were immersed in 50 ml of 2 ppm RhB aqueous solution. The solution was stirred in dark condition for 30 min to achieve absorption and/or desorption equilibrium. Subsequently, three UV lamps (8 W, 254 nm) were used to trigger the photocatalytic reaction. At 30 min interval, 2.5 ml of dye solution was withdrawn to determine the degradation of RhB dye. The degradation efficiency (DE) and degradation kinetic of RhB was calculated using equation (1) and (2), respectively as followed [17]:

$$DE\ (\%) = \frac{C - C_0}{C_0} \quad (1)$$

$$\ln\left(\frac{C_0}{C}\right) = -Kt \quad (2)$$

where, C_0 and C are the initial and time-dependent concentration of RhB, respectively. K is first-order rate constant, (min^{-1}), and t is irradiation time (min).

4.0 RESULTS AND DISCUSSION

Figure 1shows the XRD spectra of bare mesh and ZnO/meshes synthesized at different Zn^{2+} ions concentrations. The samples were designated as 0.01M, 0.02M, 0.04M and 0.06M corresponding to Zn^{2+} ions concentration. Three strong diffraction peaks at 44.7°, 64.8°, and 81.9° correspond to Aluminium Chromium Iron ($Al_{0.5}Cr_{0.5}Fe$) of Kanthal mesh [10]. Additional peaks matched well with ZnO wurtzite structure (ICDD no.: 00-074-1113), indicating that ZnO was successfully grown on kanthal mesh. The crystalinity of ZnO increased with the increase of Zn^{2+} ion concentration.

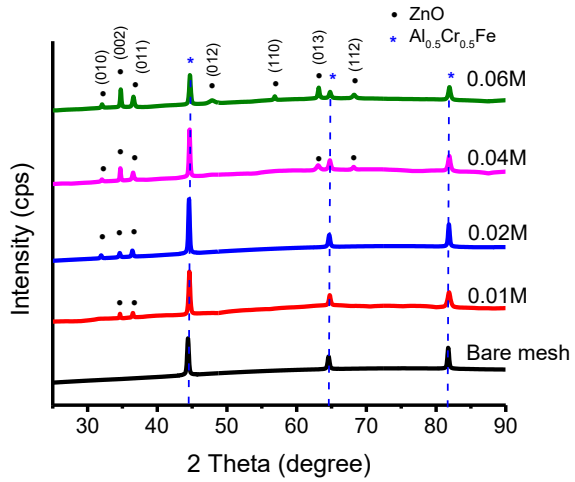

Fig. 1: XRD spectra of bare kanthal mesh and ZnO/meshes synthesized at different Zn^{2+} ion concentrations of 0.01M, 0.02M, 0.04m and 0.06M.

Fig. 2 shows the morphology of ZnO/meshes grown at different Zn^{2+} ions concentrations. Fig. 3 presents an average diameter, areal density, surface coverage and weight of ZnO particles grown on Kanthal mesh. The morphology and the growth of ZnO on kanthal meshes were strongly dependent on Zn^{2+} ion concentration. At 0.01 M, few rod-like crystallites were found on the mesh surface with low surface coverage of 72.3% and a large average diameter of 125.3 nm. Increasing the concentration to 0.02 M enhanced nucleation and growth, leading to denser coverage (78.4%) with thicker rods (166.4 nm).

At 0.04 M, ZnO NRs completely covered mesh surface (97.4%), with the highest areal density (17.7 μm^{-2}), and the smallest average diameter (87.6 nm). Furthermore, the secondary nucleation and grown in the bulk solution deposited flower-like particles on the primary grown layer (Fig. 2e). Further increasing the concentration to 0.06 M resulted in overgrowth and aggregation of ZnO NRs, which reduced areal density (8.4 μm^{-2}), increased rod diameter (155.7 nm) and caused the highest ZnO loading (10.7 mg). These results indicate that 0.04 M provides the most favorable conditions for uniform and dense ZnO NRs formation.

Based on the morphology analysis, sample 0.04 M was selected for photocatalytic study. Fig. 4 depicts the photocatalytic activity of ZnO/mesh (sample 0.04 M). Under illumination, the controlled samples show low degradation efficiency of 12.3% for RhB and 7.7% for mesh, which was attributed to photolysis [18]. In contrast, the presence of ZnO/mesh significantly in creased the degradation efficiency of RhB dye to 74.8% (Fig. 4a). This enhancement is ascribed to the nanostructures and high areal density of ZnO, which promote dye adsorption and efficient generation of electron-hole pairs that produce reactive oxygen species for decomposing RhB [19].

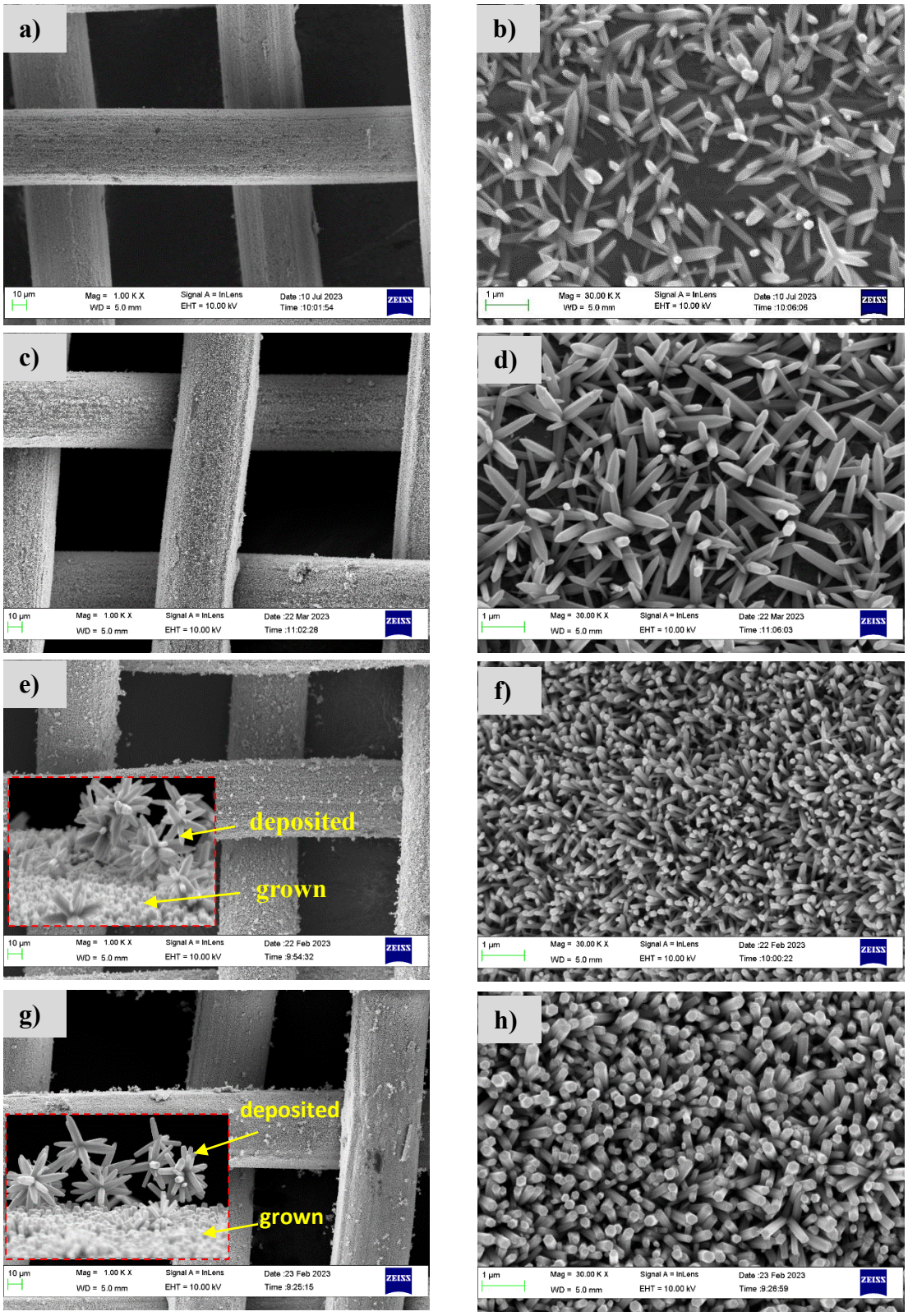

Fig. 2: FESEM images of ZnO/meshes synthesized at different Zn^{2+} ions concentrations: a, b) 0.01M; c, d) 0.02M; e, f) 0.04M; and g, h) 0.06M.

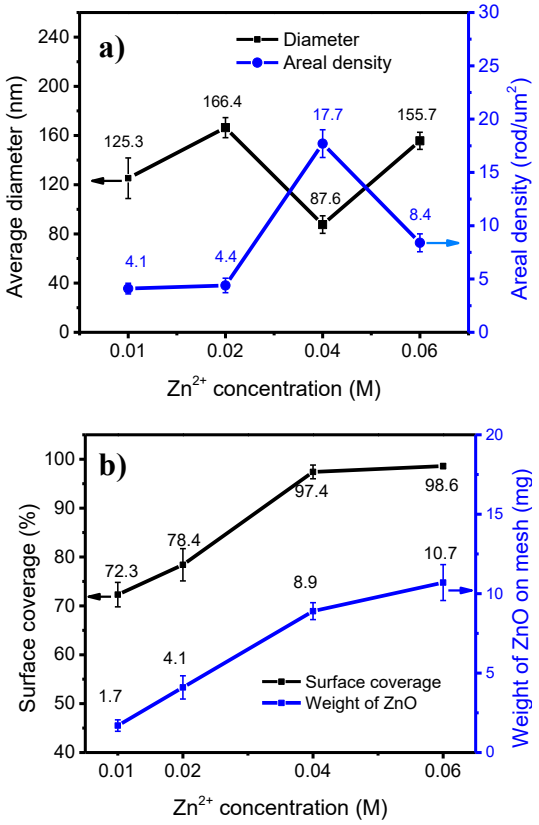

Fig. 3: a) Diameter and areal density; b) Average surface coverage and weight of ZnO NRs on Kanthal mesh. Data was measured from FESEM images of Fig. 2

As shown in Fig. 4b, the degradation of RhB in the presence of ZnO/mesh followed pseudo-first-order kinetic model, with a strong linear correlation ($R^2 = 0.98$). The corresponding degradation rate constant was calculated to be 0.0088 min^{-1} (Fig. 4c), which was nearly two orders of magnitude higher than that of the bare mesh, 5.2 × 10^{-4} min^{-1}) and the photolysis of RhB under illumination (8.6 × 10^{-5} min^{-1}). These findings confirm that ZnO nanorods grown on the mesh provide superior photocatalytic activity.

5.0 CONCLUSION

ZnO NRs were successful grown on flexible Kanthal mesh via a direct heating method. The crystallinity, diameter, areal density and surface coverage of ZnO NRs were effectively tailored by adjusting the Zn^{2+} concentration in the precursor solution. At an optimal concentration of 0.04 M, ZnO NRs with an average diameter of 87.6 nm completely covered the mesh surface. ZnO/mesh exhibited excellent photocatalytic activity in the degradation of RhB dye under UV light illumination. These findings highlight that precise control of Zn^{2+} ion concentration offers a simple yet effective strategy to tune the growth of ZnO nanostructures on flexible substrates, paving the way for their potential applications in environmental remediation.

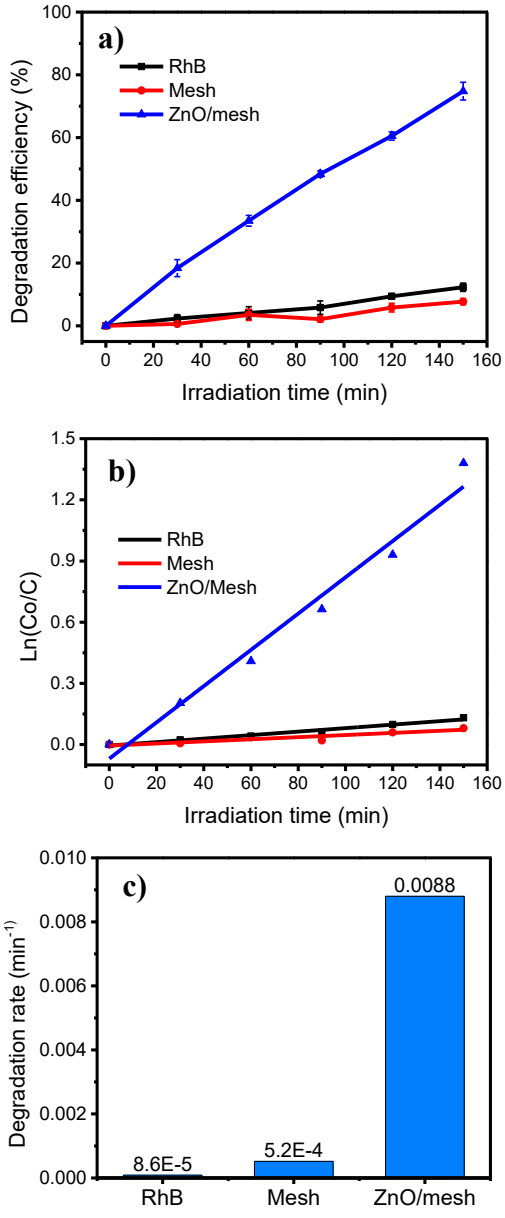

Fig. 4: Photocatalytic activity of ZnO/mesh (sample 0.04 M). a) Degradation efficiency, b)

Fist-order kinetic model and c) degradation rate of RhB dye under UV irradiation.

ACKNOWLEDGEMENTS

The authors gratefully acknowledge the support of Vietnam National University, Ho Chi Minh City (VNU-HCM), under grant number B2025-32-03, and Universiti Sains Malaysia for research funding through the Bridging Grant (Project No.: R501-LR-RND003-0000001343-0000).

REFERENCES

1. Joshi, B., et al., "Supersonically sprayed PVDF and ZnO flowers with built-in nanocuboids for wearable piezoelectric nanogenerators", Nano Energy, vol. 112, no., pp. 108447, 2023.
2. Kardeş, M., H.C. Yatmaz, and K. Öztürk, "ZnO Nanorods Grown on Flexible Polyurethane Foam Surfaces for Photocatalytic Azo Dye Treatment", ACS Applied Nano Materials, vol. 6, no. 8, pp. 6605-6613, 2023.
3. Huang, Y., et al., "Flexible piezoelectric sensor based on PAN/MXene/PDA@ZnO composite film for human health and motion detection with fast response and highly sensitive", Chem. Eng. J., vol. 488, no., pp. 150997, 2024.
4. Ragab, H.M., "Optical, thermal and electrical characterization of PEO/CMC incorporated with ZnO/TiO2 NPs for advanced flexible optoelectronic technologies", Ceram. Int., vol. 49, no. 8, pp. 12563-12569, 2023.
5. Lee, J.-H., K. Cho, and J.-K. Kim, "Age of Flexible Electronics: Emerging Trends in Soft Multifunctional Sensors", Adv. Mater., vol. 36, no. 16, pp. 2310505, 2024.
6. Hassan, M., et al., "Significance of Flexible Substrates for Wearable and Implantable Devices: Recent Advances and Perspectives", Adv. Mater. Technol., vol. 7, no. 3, pp. 2100773, 2022.
7. Nandanapalli, K.R., et al., "Predominantly enhanced catalytic activities of surface protected ZnO nanorods integrated stainless-steel mesh structures: A synergistic impact on oxygen evolution reaction process", Chem. Eng. J., vol. 429, no., pp. 132360, 2022.
8. Xing, X., et al., "Seedless hydrothermal growth of piezoelectric photocatalytic ZnO nanowires on laser-ablated copper mesh for oil/water separation", J. Environ. Chem. Eng., vol. 12, no. 2, pp. 112027, 2024.
9. Raturi, P., K. Yadav, and J.P. Singh, "ZnO-Nanowires-Coated Smart Surface Mesh with Reversible Wettability for Efficient On-Demand Oil/Water Separation", ACS Applied Materials & Interfaces, vol. 9, no. 7, pp. 6007-6013, 2017.
10. Le, A.T., et al., "Rapid immobilization of Ag/ZnO nanocomposite on Kanthal mesh for efficient removal of organic dye and heavy metal ions", Mater. Chem. Phy., vol. 339, no., pp. 130692, 2025.
11. Aziz, S.N.Q.A.A., et al., "Rapid growth of zinc oxide nanorods on kanthal wires by direct heating method and its photocatalytic performance in pollutants removal", J. Ind. Eng. Chem., no., 2022.
12. Mohamed, R. and M.S. Anuar, "Structural and Electrochemical Behaviors of ZnO Structure: Effect of Different Zinc Precursor Molarity", Cond. Mat., vol. 7, no. 4, 2022.
13. Konan, F.K., et al., "Influence of the precursor concentration on the morphological and structural properties of zinc oxide (ZnO)", Mater. Chem. Phys., vol. 229, no., pp. 330-333, 2019.
14. Amin, G., et al., "Influence of pH, Precursor Concentration, Growth Time, and Temperature on the Morphology of ZnO Nanostructures Grown by the Hydrothermal Method", J. Nanomater., vol. 2011, no. 1, pp. 269692, 2011.

15. Lausecker, C., et al., “Effects of Zinc Nitrate and HMTA on the Formation Mechanisms of ZnO Nanowires on Au Seed Layers”, Cryst. Growth Des., vol. 23, no. 4, pp. 2941-2950, 2023.
16. Le, A.T., et al., “Enhanced photocatalytic activity of Ag/ZnO nanocomposite immobilized on kanthal coils”, Physica Scripta, vol. 99, no. 8, pp. 085988, 2024.
17. Kohzadi, S., et al., “Doping zinc oxide (ZnO) nanoparticles with molybdenum boosts photocatalytic degradation of Rhodamine b (RhB): Particle characterization, degradation kinetics and aquatic toxicity testing”, J. Mol. Liq., vol. 385, no., pp. 122412, 2023.
18. de Souza, D.A., et al., “Easy and Fast Obtention of ZnO by Thermal Decomposition of Zinc Acetate and Its Photocatalytic Properties over Rhodamine B Dye”, Colorants, vol. 3, no. 3, pp. 229-252, 2024.
19. Ren, X., et al., “Controllable Synthesis of ZnO Nanoparticles with Improved Photocatalytic Performance for the Degradation of Rhodamine B under Ultraviolet Light Irradiation”, Molecules, vol. 28, no. 13, 2023.

Proceeding of the 9th International Symposium on Advanced Materials and Nanotechnology (iSAMN2025), October 29-30, 2025

Detection of Copper (II) with Oil Palm Petiole (OPP) Carbon Dots Pretreated with Lemon Juice

Tengku Nur **Adriana**[1], Mohamad Faiz **Zainuddin**[1], Nazatul Akmal **Nazibudin**[1]
Ernee Noryana **Muhamad**[2], Che Azurahanim **Che Abdullah**[3]

[1]Department of Environmental Science and Technology, Faculty of Forestry and Environment, Universiti Putra Malaysia, 43400 Serdang, Selangor, Malaysia

[2]Department of Chemistry, Faculty of Science, Universiti Putra Malaysia, 43400 Serdang, Selangor, Malaysia

[3]Department of Physics, Faculty of Science, Universiti Putra Malaysia, 43400 Serdang, Selangor, Malaysia

*Corresponding author's phone: +60397697460
E-mail: z_faiz@upm.edu.my

Received: 2 October 2025; Accepted: 28 October 2025

ABSTRACT

Past studies have demonstrated that plant derived carbon dots (CDs) can be utilized to detect a wide range of heavy metals in water such as iron(II), copper(II), mercury(II), and lead(II). Plant based CDs are considered more environmentally friendly, biocompatible and sustainable in the long run compared to CDs derived from non-renewable resources or semiconductor quantum dots (QDs). However, the use of acid treatment with strong acids such as sulphuric acid and nitric acid for pretreatment of plant-based carbon precursors are still reported. This study explores the use of citric acid (CA) from lemon juice as pretreatment of oil palm petiole (OPP) before being converted into CDs for copper(II) detection.

Keywords— Carbon dots; oil palm petiole; citric acid; hydrothermal; copper; photoluminescence

1.0 INTRODUCTION

Carbon dots (CDs) refer to the fluorescent carbon-based nanoparticles that are smaller than 10 nm. They possess excellent water solubility and tuneable light emission that make them as an excellent replacement of earlier fluorophores (Wang et al., 2020). While CDs can be synthesized from various sources, recent attention is shifted towards utilizing biomass waste as the carbon precursors.

Recently, CDs have attracted considerable attention to detect heavy metals owing to their photoluminescence properties, chemical inertness, biocompatibility, low toxicity, and affordability (Fang et al., 2024). Four heavy metals species commonly examined with CDs include mercury cation (Hg2+), ferric ion (Fe2+), cupric ion (Cu2+), and lead ion (Pb2+) (Ng et al., 2021).

This study evaluated the detection of Cu2+ with synthesized yellowish green emitting fluorescent CDs from OPP via hydrothermal route with citric acid (lemon juice) pretreatment. Citric acid was used as opposed to strong acid such as acid sulfuric and acid hydrochloric to minimize the impact of CDs production on the environment. TEM was used to assess the morphology of OPP-CDs. Zetasizer were used to determine the size of the OPP-CDs, polydispersity index (PDI), and surface charge. The OPP-CDs were tested to detect Cu2+ with concentrations ranging from 0.5 ppm to 2.0 ppm.

2.0 THEORY/LITERATURE REVIEW

CDs can be defined as zero-dimensional quasi-spherical carbon nanomaterials with a diameter of less than 10 nm and luminous characteristics. There are several classification CDs. One of them, carbonized polymer dots (PDs) are composed of carbon core centers and surface passivation layer (Fig. 1). The core centers of CDs exhibit nanocrystalline or amorphous characteristics while the surfaces of CDs are characterized by the presence of functional groups and exhibits a graphite-like structure (Guo et al., 2021; Sanni et al., 2023; Chen et al., 2025)

CDs are well known for their inherent fluorescence properties due to their wide range of tunable absorption and emission spectra. In the UV-NIR spectral range, CDs can display significant photoluminescence (PL) phenomena. Arguable the most outstanding features of CDs is the PL feature, and their outstanding performances has led to widespread applilcation of CDs in optical sensors, optical devices, catalysis, and plant photosynthesis (Chen et al., 2025).

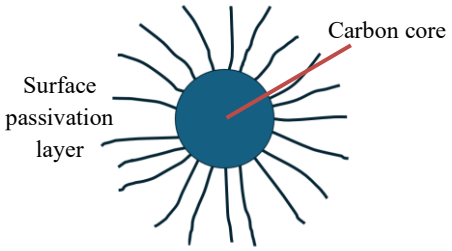

Fig. 1: Schematic diagram of PDs structure

3.0 MATERIALS

Fig. 2: Raw OPP (left) and OPP powder (right)

Raw OPF samples were cut and dried in an oven at 200°C for 24 hours (Fig. 2). After drying, they were ground and sieved through a 2 mm mesh to obtain OPP powder. Lemon juice was obtained by slicing and squeezing fresh lemon juice. Then, the juice was filtered with 0.2 µm filter paper to remove pulps and seeds. Then, 2.5 g of OPP powder was mixed with 10 ml of lemon juice. The mixture was stirred continuously and vigorously for two minutes to ensure homogeneity.

Next, 2.5 g of treated OPP powder was placed in a polypropylene (PPL)-lined stainless-steel autoclave reactor with 50 mL of deionized water. The reactor was heated in a furnace at 200°C for 2 hours. The resulting solution was centrifuged at 1000 rpm for 30 minutes. After centrifugation, the solution was filtered through 0.2 µm filter paper to remove macroparticles. TEM was used to image the CDs while a Zetasizer (Malvern) is used to measure particle size.

4.0 EXPERIMENTAL PROCEDURES

Different concentrations of Cu2+ samples (0.5 – 2.0 ppm) were prepared by diluting a stock solution of 1000 ppm copper (II) sulfate. The stock solution was prepared by dissolving 1 g of copper (II) sulfate salt in 1 L of distilled water. For the detection assessment, 2 mL of the CDs solution was mixed with 2 mL of the Cu2+ sulfate solution. The photoluminescence (PL) properties of the mixture were examined with Perkin Elmer spectrophotometer at an excitation wavelength of 370 nm to determine the quenching effects on the CDs.

5.0 RESULTS AND DISCUSSION

5.1 Physical characterization

The TEM images of the OPF-CDs suggested that the CDs are monodisperse nanoparticles of near spherical morphology with size ranging between 6 nm and 9 nm (Fig. 3). The changes in the apparent color

of the CD solutions under UV light were observed (Fig. 4). The green-yellowish fluorescence of the CD solutions appeared to be less visible to the naked eye with decreasing concentration of pure CDs

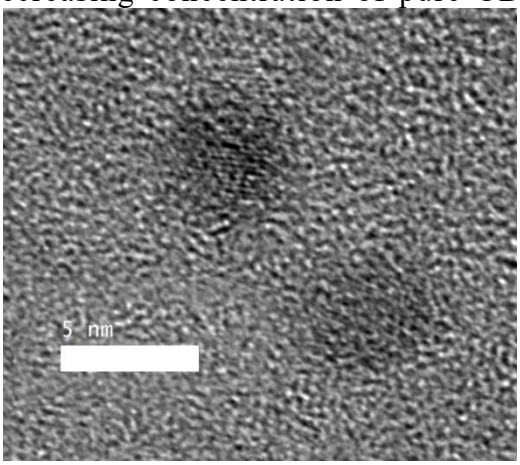

Fig. 3: TEM image of the OFP-CDs

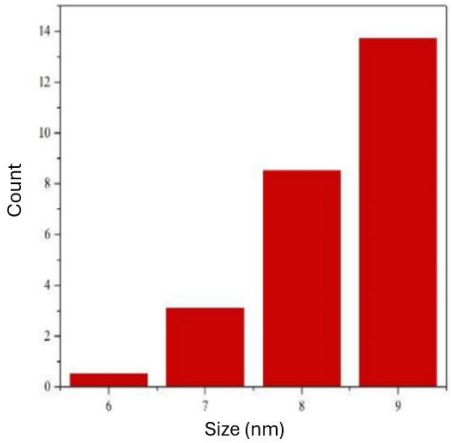

Fig. 4: Zetasizer count

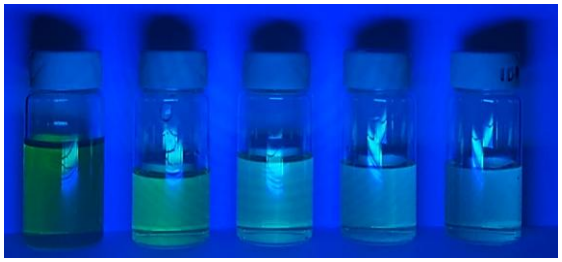

Fig. 5: Apparent color of the unadulterated CDs

solutions from 0.01 mg/mL to 0.001 mg/mL (Fig. 5).

5.2 Detection of Cu2+

Results from PL analysis show a substantial quenching impact of the OPP-CDs by the presence of Cu2+ (Fig. 6). In the absence of Cu2+, the OPP-CDs clearly exhibit a strong PL peak at 470 nm. With an increase in the concentration of Cu2+, PL intensity decreases successively in a linear trend. The explanation for PL quenching is thought to be caused by the formation of complexation between OPP-CDs and Cu2+ which results in the electron transfer between Cu2+ ions and OPP-CDs as proposed by Sanni et al. (2022) (Fig. 7).

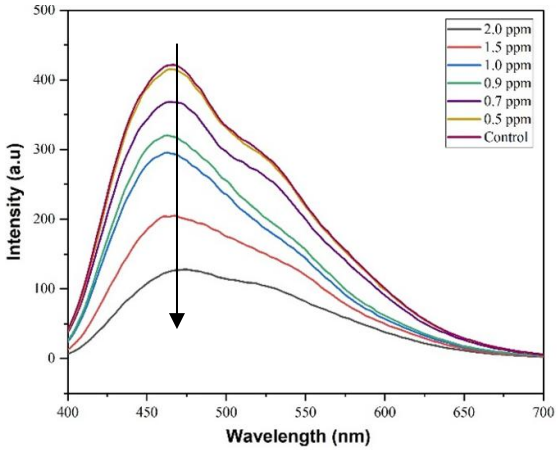

Fig. 6: PL emission of CDs in the presence of different concentrations of Cu2+

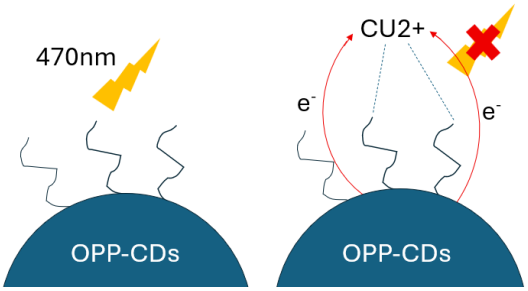

Fig. 7: Proposed fluorescence-quenching mechanism of OPP-CDs by Cu2+

6.0 CONCLUSION

Lemon juice was used to treat the OPP carbon precursors. Being a natural acid, lemon juice is non-toxic, safe for human consumption, and environmentally benign. The OPP-CDs were tested to detect CU2+ between 0.5 ppm and 2.0 ppm.The OPP-CDs were proven to detect CU2+ concentration as low as 0.5 ppm which is well below the 1.3 ppm limit set by the US EPA for water quality standards.

ACKNOWLEDGEMENTS

This research was funded by the Ministry of Higher Education Malaysia, under the Fundamental Research Grant Scheme (FRGS/1/2018/STG02/UPM/02/5) with additional support from the UPM Geran Putra (UPM.RMC.800-3/3/1/2023/GP/972000).

REFERENCES

1. M. Chen, J. Ma, Y. Feng, Y. Wu, G. Hu, and X. Liu, "Advanced characterization enables a new era of efficient carbon dots electrocatalytic reduction," Coordination Chemistry Reviews, Vol. 535, 216612, 2025.
2. M. Fang, B. Wang, X. Qu, S. Li, J. Huang, J. Li, S. Lu and N. Zhou, "State-of-the-art of biomass-derived carbon dots: Preparation, properties, and applications," Chinese Chemical Letters, vol. 35, no. 1, 108423, 2024.
3. R. Guo, L. Li, B. Wang, Y. Xiang, G. Zou, Y. Zhu, H. Hou, and X. Ji, "Functionalized carbon dots for advanced batteries. Energy Storage Materials," vol. 37, 8–39, 2021.
4. H. M. Ng, G. Lim and C. Leo, "Comparison between hydrothermal and microwave-assisted synthesis of carbon dots from biowaste and chemical for heavy metal detection: A review," Microchemical Journal, Vol. 165, 106116, 2021.
5. S. O. Sanni, H. G. Theo, Moundzounga, E. O. Oseghe, Nils Haneklaus, E. L. Viljoen and Hendrik Gideon Brink, "One-Step Green Synthesis of Water-Soluble Fluorescent Carbon Dots and Its Application in the Detection of Cu2+," vol. 12, no. 6, 958–958, 2022.
6. Y. Wang, J. Sun, B. He and M. Feng, "Synthesis and modification of biomass derived carbon dots in ionic liquids and their application: A mini review," Green Chemical Engineering, vol. 1, no. 2, 94–108, 2020.

Proceeding of the 9th International Symposium on Advanced Materials and Nanotechnology (iSAMN2025), October 29-30, 2025

Concentration Effects of Copper in ZnO Nanorods for Enhanced Antibacterial Photocatalysis

Muhammad Haziq Daniel **Rahim**[1], Aini Ayunni **Mohd Raub**[1], Khanom **Simarani**[2], and Jumril **Yunas**[1*]

[1]Institute of Microengineering and Nanoelectronics (IMEN), Universiti Kebangsaan Malaysia (UKM), Bangi, 43600, Selangor, Malaysia.
[2]Institute of Biological Sciences, Faculty of Science, Universiti Malaya, Kuala Lumpur, 50603, KualaLumpur, Malaysia.

*Corresponding author's phone: +603-89118541
E-mail: jumrilyunas@ukm.edu.my

Received: 30 September 2025; Accepted: 28 October 2025

ABSTRACT

Cu-doped zinc oxide (ZnO) nanorods were synthesized on glass substrates by a seed-assisted hydrothermal method with Cu concentrations of 4%, 8%, and 12% to enhance visible-light photocatalytic activity and antibacterial performance. Field-emission scanning electron microscopy with energy-dispersive X-ray spectroscopy confirmed improved nanorod alignment and successful Cu incorporation. The 8% Cu composition grown for 6 hours produced the maximum inhibition zone (2.5cm) against *Staphylococcus aureus*, while *Escherichia coli* showed no inhibition under the tested conditions. These results indicate that optimized Cu doping (8%) shifts ZnO activity into the visible range and enhances ROS-mediated bactericidal action against Gram-positive pathogens, supporting potential use as visible-light-activated antimicrobial surfaces.

Keywords—Cu-doped ZnO; nanorod; visible-light photocatalysis; antibacterial activity; reactive oxygen species

1.0 INTRODUCTION

Zinc oxide (ZnO) is a widely used semiconductor photocatalyst because of its strong oxidation potential, chemical or thermal stability, and large exciton binding energy, but its wide direct bandgap (~3.37 eV) restricts photoexcitation to the ultraviolet portion of sunlight [1]. Extending photocatalytic activity into the visible range and suppressing fast electron–hole recombination are therefore key challenges for practical water-treatment and antibacterial applications [2].

Cationic doping and heterojunction formation are established strategies to narrow the effective bandgap and improve charge separation in ZnO, enabling visible-light activation and enhanced photocatalytic performance [3]. Copper (Cu) is an attractive dopant for ZnO because Cu^{2+} readily incorporates into the ZnO lattice, can modify nucleation and growth kinetics during hydrothermal synthesis, and introduces defect states that alter optical absorption and carrier dynamics [4]. Nanorod morphology, particularly vertically aligned, one-dimensional arrays, strongly influences light harvesting, accessible surface area, and reactive oxygen species (ROS) production, so precise control of nanorod geometry is critical when designing antibacterial photocatalysts [5].

Despite these general strategies, systematic studies that link copper precursor concentration during the seed-assisted hydrothermal growth to controlled ZnO nanorod morphology and

the resulting antibacterial photocatalytic potential are limited, and optimization of Cu content remains an open synthesis–structure problem [6].

The present study addresses this gap by investigating copper concentration effects during hydrothermal growth to derive synthesis guidelines for morphology control of ZnO nanorods aimed at improved visible-light antibacterial photocatalysis.

2.0 THEORY/LITERATURE REVIEW

ZnO photocatalysis relies on photon absorption that excites electrons from the valence band to the conduction band, producing electron–hole pairs that react at the surface to form reactive oxygen species (ROS) such as superoxide ($\bullet O_2^-$), hydroxyl radicals (•OH) and H2O2; these ROS are the primary agents that damage bacterial cells and break down organic pollutants [7].

Pristine ZnO has a wide direct bandgap (~3.2–3.37 eV), so it absorbs predominantly UV light and cannot efficiently harvest visible solar photons, and rapid electron–hole recombination further limits ROS yield and overall antibacterial/photocatalytic effectiveness [8]. Incorporating copper modifies ZnO's electronic and interfacial chemistry in two complementary ways: substitutional Cu (or an interfacial CuO phase) introduces new electronic states that extend absorption toward the visible range, and formation of a ZnO/CuO p–n heterojunction promotes spatial separation of electrons and holes, increasing carrier lifetime and ROS generation [9,10].

These beneficial electronic effects are strongly composition dependent: low-to-moderate Cu levels commonly narrow the effective bandgap and improve charge separation, but excessive Cu can produce large CuO domains, too many lattice defects, or "shadowing" of active ZnO surfaces, which act as nonradiative recombination centers and reduce activity [11].

Nanorod architecture provides the structural platform that translates electronic improvements into usable photocatalyst performance [12]. The vertically aligned rods structure enhance light capture (via scattering and guided-mode effects), shorten the radial distance charges must travel to reach reactive surfaces, and expose high-area active facets for ROS formation, all of which help maximize the benefit of improved carrier separation [13].

Therefore, copper precursor concentration during hydrothermal growth controls a coupled set of variables, such as actual dopant incorporation, defect density, secondary-phase (CuO) formation, and nanorod morphology. All that variables together may determine visible-light absorption, carrier dynamics and ROS output; mapping this composition structure function space by a systematic concentration sweep is necessary to identify the synthesis window that yields optimal antibacterial photocatalysts [14].

3.0 MATERIALS

Sodium hydroxide (NaOH), zinc acetate dihydrate ($Zn(CH_3COO)_2 \cdot 2H_2O$), zinc nitrate hexahydrate ($Zn(NO_3)_2$), hexamethylenetetramine (HMTA), copper (II) nitrate ($Cu(NO_3)_2$) acetone, methanol, ethanol, Mueller-Hinton agar, nutrient agar.

4.0 EXPERIMENTAL

4.1 Preparation of ZnO Seed Layer

Glass slides (1.5 cm × 1.5 cm) were used as substrates for ZnO seed layer deposition. The slides were cleaned sequentially in acetone, ethanol, and deionized (DI) water, followed by ultrasonication for 7 mins in each solvent.

A 0.01M zinc acetate dihydrate (43.9mg) solution was prepared in 20mL methanol and stirred for 30 mins at 60°C.

Separately, a 0.09M sodium hydroxide (72 mg) solution was dissolved in 20mL methanol, stirred for 25 mins at room temperature, and then preheated to 60°C. The NaOH solution was added dropwise to the zinc acetate solution and stirred continuously for 2 hours at 60°C to form a stable ZnO seed suspension.

4.2 Synthesis of Cu-Doped ZnO NRs

The ZnO seed suspension was deposited on the glass substrates using a spin-coating method at 3000rpm for three cycles of 30 seconds each. The coated substrates were annealed at 250°C for 30 mins. Zinc oxide nanorods (ZnO NRs) were grown hydrothermally by immersing the seeded substrates (inverted) into an equimolar aqueous solution of 0.025M zinc nitrate hexahydrate (743.72mg) and hexamethylenetetramine (352.15mg) in 100mL DI water.

For Cu doping, varying concentrations of copper (II) nitrate were added into the growth solution by molarity ratios of 4%, 8% and 12% mol.

To investigate the effect of growth duration, the hydrothermal process was conducted at 95°C for 2, 4, and 6 hours, respectively. After growth, the substrates were rinsed with DI water, dried, and annealed again at 250°C for 2 hours. designations.

4.3 Characterization of ZnO NRs

The synthesized Cu-doped ZnO NRs were characterized using Field Emission Scanning Electron Microscopy (FESEM) to examine the surface morphology, alignment, and density of the nanorods. Energy Dispersive X-ray spectroscopy (EDX) coupled with FESEM to confirm elemental composition and verify successful Cu incorporation.

4.4 Bacterial Strains and Growth Condition

Antibacterial performance was tested against *Escherichia coli* (Gram-negative) and *Staphylococcus aureus* (Gram-positive) obtained from the Microbiology and Genetics Department, Universiti Malaya. Bacterial cultures were maintained on nutrient agar and sub-cultured regularly at room temperature.

4.5 Antibacterial Testing

The antibacterial efficacy of Cu-doped ZnO NRs was assessed via the disc diffusion method. The flow process for the antibacterial test is schematically shown in Figure 1. A loopful bacterial colony was suspended in 5mL sterile distilled water, vortexed for homogenization, and adjusted to match the 0.5 McFarland standard. The suspension was lawned onto Mueller-Hinton agar plates, and the ZnO NR-coated glass substrates were placed directly on the agar surface. Samples were incubated under visible light at room temperature for 24 hours.

Inhibition zones were measured to quantify antibacterial activity. An antibiotic disc served as positive control, while clean glass slides (without ZnO) acted as the negative control.

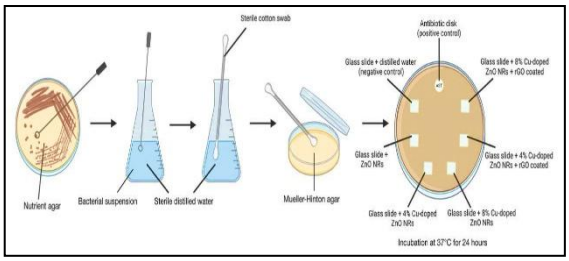

Fig. 1: Schematic diagram of antibacterial testing.

5.0 RESULTS AND DISCUSSION

5.1 FESEM Analysis

Field-emission scanning electron microscopy (FESEM) was employed to examine the surface morphology and cross-sectional views of the synthesized ZnO nanorods. Figure 2 presents FESEM images of both undoped (pristine) ZnO nanorods and Cu-doped ZnO NRs.

Figure 2(a) shows the top view of grown pristine ZnO NRs. The diameter and length distribution of ZnO NRs was measured with ImageJ software. It is observed that the undoped nanorods exhibit the typical hexagonal crystal structure of ZnO nanostructure with diameter of 64 nm and length of 6 µm.

Figure 2(b) shows the FESEM cross-sectional view of Cu doped ZnO NRs. It is seen that 8% Cu doping increases the mean rod diameter to about 83 nm while reducing the average length to roughly 5 µm. On the other hand, there is noticeable different of grown rods between pure ZnO NRs and Cu doped ZnO NRs. Based on Figure 3, the addition of Cu concentration may modified or distorted the hexagonal structure of the ZnO nanorods, which causes neighbouring rods to merge or agglomerate (clumping).

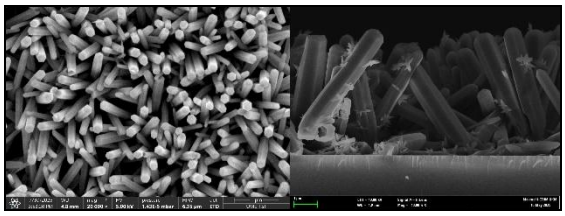

(a) (b)

Fig. 2: FESEM analysis of hydrothermally grown ZnO nanorods, (a) surface view of pure ZnO NRs (b) Cross-sectional of Cu doped ZnO NRs

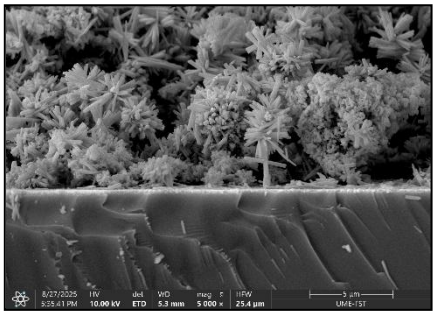

Fig. 3: FESEM analysis of grown Cu doped ZnO NRs

5.2 EDX Analysis

The atomic and weight percentages of different elements present in the synthesized ZnO NRs was evaluated using Energy Dispersive X-ray (EDX) spectroscopy analysis. Figure 4 shows the EDX spectrum for 8% Cu-doped ZnO NRs. The spectrum analysis of ZnO NRs revealed the presence of Zn, O, and Cu elements, respectively.

Significant Zn and O peaks were observed in the spectrum. The presence of Cu indicates that Cu ions were successfully incorporated into the ZnO NRs. The obtained EDX spectrum did not show the presence of any foreign elements, indicating that Cu-doped ZnO NRs were synthesized without contamination.

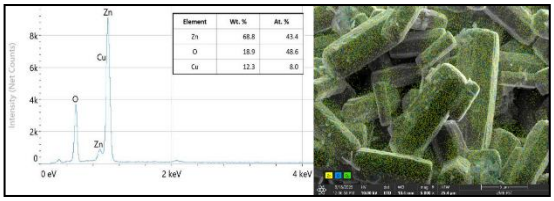

(a) (b)

Fig. 4: (a) EDX spectrum analysis of grown 8% Cu doped ZnO NRs (b) mapping analysis of grown Cu doped ZnO NRs

5.3 Antibacterial Testing

The antibacterial testing of synthesized ZnO NRs and Cu-doped ZnO NRs were assessed via the disc diffusion method. Figure 5 shows the antibacterial effect of the synthesized ZnO NRs against Gram-positive bacteria, *Staphylococcus aureus*.

Figure 5(a) shows the formation of inhibition zone for the negative control (clear and clean glass slide) and glass slide with undoped ZnO NRs. It can be observed the glass sample with undoped ZnO NRs exhibits halo or clear zone on the agar surface with diameter 3 cm. This happens primarily due to antibacterial activity of ZnO against *S. aureus*. In contrast, no zone of inhibition (ZOI) was observed in the control sample, confirming that the antibacterial effect is directly linked to the presence of ZnO [15].

Figure 5(b) shows the formation of inhibition zones for the two glass slides coated with 8% Cu-doped ZnO NRs. It can be observed that both samples exhibit a clear inhibition zone with an average diameter of 3.3 cm. This suggests that Cu doping enhances the antibacterial activity

of ZnO NRs. The improved inhibition may be attributed to the increased generation of reactive oxygen species (ROS) facilitated by Cu ions, which can disrupt bacterial cell membranes more effectively [16]. Additionally, Cu doping narrows the bandgap of ZnO, enabling better photocatalytic activity under visible light, whereas pure ZnO is primarily active only under UV light. This enhanced visible-light responsiveness further supports the improved antibacterial performance.

(a) (b)

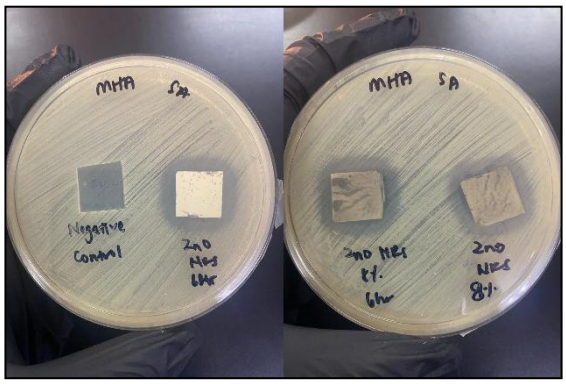

Fig. 5: Antibacterial testing against *S. aureus*
(a) ZOI of negative control and undoped ZnO NRs
(b) ZOI of 8% Cu doped ZnO NRs

Antibacterial testing was also carried out on Gram-negative bacteria, *Escherichia coli*. However, all the tested samples (both doped and undoped ZnO NRs) exhibited no inhibitory effect. As shown in Figure 6, the two glass slides coated with 8% Cu-doped ZnO display no visible inhibition zones.

Fig. 6: Antibacterial testing of 8% Cu doped ZnO NRs against *E. coli*

The glass substrates with either doped or undoped ZnO NRs proved to be more effective against *S. aureus* (Gram-positive) compared to *E. coli* (Gram-negative). This difference in antibacterial activity is likely due to the distinct structural makeup of their cell walls. The Gram-positive bacteria have a thick peptidoglycan layer that is more vulnerable to ZnO NRs, whereas the outer membrane of Gram-negative bacteria, rich in lipopolysaccharides, acts as a protective barrier that limits zinc ion entry [17].

Consequently, ZnO NRs show reduced antibacterial performance against Gram-negative bacteria. These results highlight how the composition and the structure of bacterial cell walls significantly influences the effectiveness of ZnO NRs. Therefore, further modification may be needed to enhance its performance against Gram-negative species.

Figure 7 presents the inhibition zone measurements for all samples tested against *S. aureus*. It can be seen that Cu doping enhances antibacterial activity. However, increasing the doping level beyond a certain point may reduce the effectiveness. Specifically, samples with 12% Cu doping exhibit smaller inhibition zones than those with 8%, indicating that the antibacterial activity is influenced by the Cu concentration.

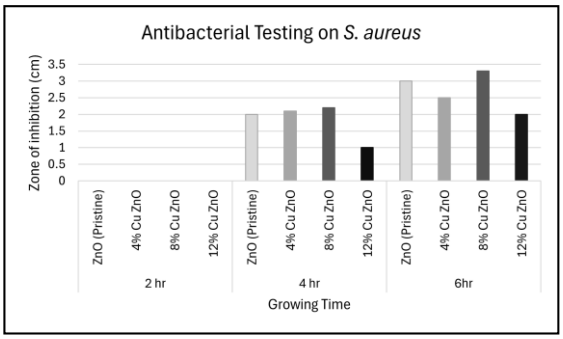

Fig. 7: Zone of inhibition measurement for tested samples against *S. aureus*

6.0 CONCLUSION

In conclusion, the results show that Cu doped ZnO NRs exhibit strong antibacterial activity against *S. aureus*

(Gram-positive), with the optimum doping concentration identified at 8% and grown for 6 hours. The enhanced performance at this level suggests that Cu incorporation improves the antibacterial properties of ZnO NRs. However, all tested samples, including the doped ones, showed no inhibition against *E. coli* (Gram-negative), likely due to the protective nature of its outer membrane, which limits zinc ion penetration. These findings highlight the importance of doping concentration in optimizing antibacterial performance and indicate that further modification may be needed to target Gram-negative bacteria effectively

ACKNOWLEDGEMENTS

This research was funded and supported by the Ministry of Higher Education Malaysia under Project Grant FRGS/1/2023/TK09/UKM/02/4, focusing on "Antibacterial Photocatalytic Mechanism on Doped ZnO/Graphene Oxide nanorods as a Reusable Antibacterial Agent." The authors also would like to express their gratitude to the staff and technicians from the Institute of Microengineering and Nanoelectronics at Universiti Kebangsaan Malaysia (UKM) for their valuable contributions to this work.

REFERENCES

1. Melese, A. et al., A comprehensive review on recent progress in synthesis methods of ZnO/CuO nanocomposites and their biological and photocatalytic applications., Results in Chemistry, vol. 14, pp. 102141, 2025.
2. Zhang, R., Zeng, K., and Zhang, T, Enhanced visible-light-driven photocatalytic activity of Bi_2WO_6-BiSI Z-scheme heterojunction photocatalysts for tetracycline degradation, International Journal of Environmental Analytical Chemistry, vol. 102, no. 18, pp. 7084-7099, 2020.
3. Li, Y. et al., Engineering the Band-Edge of Fe_2O_3/ZnO Nanoplates via Separate Dual Cation Incorporation for Efficient Photocatalytic Performance, Industrial & Engineering Chemistry Research, vol. 59, no. 42, pp. 18865-18872, 2020.
4. Baruah, S., and Dutta, J, Hydrothermal growth of ZnO nanostructures, Science and Technology of Advanced Materials, vol. 10, no. 1, pp. 013001, 2009.
5. Ojha, A. K. et al, Synthesis of well–dispersed silver nanorods of different aspect ratios and their antimicrobial properties against gram positive and negative bacterial strains, Journal of Nanobiotechnology, vol. 11, no. 1, pp. 42, 2013.
6. Bouras, D. et al, Cu:ZnO deposited on porous ceramic substrates by a simple thermal method for photocatalytic application., arXiv (Cornell University), 2018.
7. Chen, X. et al, Preparation of ZnO Photocatalyst for the Efficient and Rapid Photocatalytic Degradation of Azo Dyes, Nanoscale Research Letters, vol. 12, no. 1, 2017.
8. Abebe, B. et al, A Review on Enhancing the Antibacterial Activity of ZnO: Mechanisms and Microscopic Investigation, Nanoscale Research Letters, vol. 15, no. 1, 2020.
9. Mejia-Bernal, J. R. et al, Photocurrent generation using ZnO/CuO/Ag heterojunction films, Journal of Materials Science: Materials in Engineering, vol. 20, no. 1, 2025.
10. Yuan, S. J. et al, Zn/S-modified Cu_2O nanoparticles for applications in photocatalysis, IOP Conference Series: Earth and Environmental Science, vol. 787, no. 1, pp. 012028, 2021
11. Kim, T. G. et al, Effects of Zn amount on the properties of Zn-Cu2O composite films grown for PEC photoelectrodes by using electrochemical deposition, Journal of the Korean Physical Society, vol. 67, no. 7, pp. 1273-1277, 2015.

12. Three-Dimensional Core–Shell Nanorod Arrays for Efficient Visible-Light Photocatalytic H_2 Production, ACS Applied Materials & Interfaces, vol. 10, no. 41, pp. 35184-35193, 2018
13. Langer, J. et al, Present and Future of Surface-Enhanced Raman Scattering, ACS Nano, vol. 14, no. 1, pp. 28-117, 2019.
14. Biswal, H. J. et al, ZnO/CuO nanostructures anchored over Ni/Cu tubular films via pulse electrodeposition for photocatalytic and antibacterial applications, Materials Science for Energy Technologies, vol. 6, pp. 237-251. 2023
15. Rezaei, F. Y., et al., Antibacterial Activity, Cell Wall Damage, and Cytotoxicity of Zinc Oxide Nanospheres, Nanorods, and Nanoflowers, ACS Applied Nano Materials, vol. 7, no. 13, pp. 15242-15254, 2024.
16. Chatterjee, A. K., et al., Mechanism of antibacterial activity of copper nanoparticles, Nanotechnology, vol. 25, no. 13, pp. 135101, 2014.
17. Abebe, B. et al, A Review on Enhancing the Antibacterial Activity of ZnO: Mechanisms and Microscopic Investigation, Nanoscale Research Letters, vol. 15, no. 1, 2020.

A Comparative Study of Yeast Co-cultures in Enhancing Bacterial Cellulose Production and Its Properties

Nuratika **Hasanuddin**[1*], Nur Farhanul Iman **Ahmad Fozi**[1], Farzana **Muhammad Ramzan**[1], Nurul Syafikah Putri **Mohd Jeffree**[1], Aziz **Ahmad**[1], Azila **Adnan**[1*]

[1]Faculty of Science and Marine Environment, Universiti Malaysia Terengganu, 21030 Kuala Nerus, Terengganu, Malaysia

*Corresponding author's phone: +609-6683370
E-mail: azila.adnan@umt.edu.my

Received: 12 September 2025; Accepted: 13 October 2025

ABSTRACT

The production of bacterial cellulose (BC), a biopolymer with a variety of applications, is constrained by its low yield. This study examines the effects of co-culturing *Saccharomyces cerevisiae* and traditional "tapai" yeast with a symbiotic culture of yeast and bacteria (SCOBY) on the production and properties of BC. Three different configurations were used for the 14-day, static fermentation procedure at 30°C: SCOBY alone, SCOBY + *S. cerevisiae* (0.12 g), and SCOBY + "tapai" yeast (0.12 g). With 8.48 ± 0.46 g (5.5 ± 0.5 mm thickness), the results showed that "tapai" yeast significantly increased BC production in comparison to *S. cerevisiae* (4.49 ± 0.13 g) and control (3.10 ± 0.03 g). Following more optimisation with several quantities of "tapai" yeast, the optimal amount was determined to be 0.15 g, which produced 10.71 ± 0.19 g BC. The "tapai" group in BC had the highest crystallinity index (84.2%), followed by *S. cerevisiae* (68.5%) and control (61.3%), per an X-ray diffraction (XRD) investigation. The tensile strength and FTIR spectra confirmed the structural integrity and cellulose-specific functional groups. These findings suggest that "tapai" yeast enhances BC production and quality while offering a cost-effective and sustainable alternative.

Keywords—bacterial cellulose; production; yeast; fermentation

1.0 INTRODUCTION

Bacterial cellulose (BC) is a highly pure, reusable biopolymer produced by acetic acid bacteria, namely *Komagataeibacter* species. Its distinct nanofibrillar network, high crystallinity, mechanical strength, and biocompatibility set it apart from plant-derived cellulose, making it suitable for a wide range of applications in food, medicine, textiles, and innovative materials. Despite these benefits, large-scale adoption of BC is limited by low production yields in conventional monocultures, which creates a significant hurdle to commercial viability (Uțoiu et al., 2025).

Co-culture techniques have been a viable way to improve BC synthesis in recent years. It is well established that symbiotic cultures of bacteria and yeast (SCOBY), like those used in kombucha fermentation, enhance substrate utilisation, boost cellulose production, and enrich metabolic activity. The amylolytic and saccharolytic enzymes that yeasts provide hydrolyse complex sugars into fermentable substrates, increasing the amount of carbon available to bacterial strains that produce cellulose. The entire potential of this strategy is, however, constrained by the limited diversity of yeast species used in BC co-cultures (Brugnoli et al., 2023; Mauro et al., 2024).

Traditional fermentation starters from Southeast Asia, such "tapai" yeast, are an underappreciated source of microbial diversity with potent enzymatic properties.

"Tapai" yeast, which is made up of a variety of yeasts and filamentous fungi, has long been used in food fermentations that contain starch and is renowned for its capacity to convert complicated carbs into simple sugars. Therefore, by offering a more abundant metabolic environment for bacterial growth and cellulose generation, including "tapai" yeast into SCOBY-based systems may improve BC yield and quality (Feng et al., 2024).

The present study investigates the effects of co-culturing Saccharomyces cerevisiae and “tapai” yeast with SCOBY on BC production and material properties. Specifically, it evaluates yield, crystallinity, tensile strength, and structural integrity under static fermentation conditions. By comparing the performance of conventional yeast with traditional fermentation starters, this research highlights the potential of “tapai” yeast as a cost-effective, sustainable, and scalable alternative for improving BC synthesis.

2.0 THEORY/LITERATURE REVIEW

BC is a biopolymer with better physicochemical qualities than plant-derived cellulose. Its applications include biomedical, food, and textile industries. Monoculture yields remain modest, limiting commercial expansion (Jozala et al., 2021). Media optimisation, agro-waste substrates, and adaptive strain evolution have all been attempted to address this bottleneck, with limited success (Ul-Islam et al., 2022; Kim et al., 2024).

Co-culture systems have evolved as a viable solution for increasing BC output and tailoring its features. Yeasts in symbiotic bacteria and yeast (SCOBY) produce saccharolytic enzymes, which improve substrate availability, resulting in greater yields. While studies reveal strain-dependent effects, such as *Candida* species increasing BC yield and *Saccharomyces cerevisiae* producing varying results (Wahid et al., 2022), current research has also demonstrated functional composites such as BC-hyaluronic acid via co-culture (Zhong et al., 2023). A 2025 assessment highlighted co-culture as a scalable yield and property enhancement technique (Jung et al., 2025). Traditional Southeast Asian fermentation starters, like as "tapai" yeast, have received little attention, despite their high enzymatic activity and potential as a unique, cost-effective approach for industrial BC production.

3.0 MATERIALS

A handmade Kombucha bought from an online business, KombuCharm was employed as the inoculum. The starter culture was grown and maintained in black tea broth (Boh, Teh Harimau), which was supplemented with 20% w/v sucrose (Gula Prai, Malayan Sugar Co. Bhd, Malaysia) obtained from a local supermarket. *Saccharomyces cerevisiae* (MauriPan, obtained from a local grocery), and "Tapai" yeast, (Angel Rice Leaven), comprising *Rhizopus oryzae* and rice flour, were purchased from the online retailer HoHo Herb.

4.0 EXPERIMENTAL

A series of static fermentation experiments were carried out to determine the influence of various yeast co-cultures on bacterial cellulose (BC) synthesis. The researchers evaluated the performance of a symbiotic culture of bacteria and yeast (SCOBY) alone to SCOBY supplemented with *Saccharomyces cerevisiae* and traditional "tapai" yeast.

4.1 Fermentation Media

BC was produced using the method of Goh et al. (2012) with slight modifications. Briefly, 180 ml of distilled water was boiled in a 250 ml beaker, after which 3 g of Boh tea and 18 g of sugar were added and homogenized using a magnetic stirrer. The mixture was infused for 5 minutes, cooled to room temperature, and then autoclaved. Under sterile conditions, the tea medium was divided into three treatment groups: (i) control with 10 ml

starter tea only, (ii) 0.12 g *Saccharomyces cerevisiae* + 10 ml starter tea, and (iii) 0.12 g "tapai" yeast + 10 ml starter tea. Each treatment was prepared in triplicate. The pH of the media was adjusted using HCl or NaOH as needed (Laavanya et al., 2021).

4.2 Fermentation Conditions

Each 250 mL beaker (190 mL working volume) was covered with cheesecloth and tied with a rubber band to allow for oxygen exchange for aerobic development. Fermentation took place at 30°C under static circumstances for 14 days. The pH of the medium was measured on days 0, 7, and 14 to ensure optimal conditions for BC synthesis (Portela et al., 2019).

4.3 Purification of BC

The BC pellicles were rinsed with distilled water before being cleansed with 0.1 M NaOH for 30 minutes to eliminate any microbiological cells adhered to the BC surfaces. The purified BC was dried at 60°C in an oven until it attained a consistent bulk.

4.4 Optimization of "Tapai" yeast mass

To identify the best concentration of "Tapai" yeast for maximum BC production and characteristics, three different masses (0.05 g, 0.10 g, and 0.15 g) were chosen, representing concentrations of 0.028%, 0.056%, and 0.083% (w/v), respectively. These values were determined based on a previous work by Montenegro-Silva et al. (2024), which found that yeast concentration has a substantial effect on microbial metabolism, altering BC yield and structural features. Then, each beaker was wrapped in cheesecloth and sealed with elastic band. The beakers were incubated at 30°C for 14 days in static circumstances.

4.5 Fourier Transform Infrared Spectroscopy (FTIR)

The wavenumber range was set from 3500 to 500 cm^{-1} with an accumulation of 16 scans and a resolution of 4 cm^{-1}. FTIR works on the principle of measuring the quantity of infrared radiation absorbed at various wavelengths by the sample. The resulting spectrum indicated the information carrying chemical bonds and functional groups present in BC.

4.6 X-ray Diffraction (XRD)

The BC samples for XRD were dried with care to ensure that no moisture was trapped on the material, possibly affecting the diffraction results. Drying was done on the samples before they were mounted on the XRD sample holder. The analysis for the determination of diffraction pattern crystallinity index and changes in crystal structure was performed after scanning the samples from a range of angles. Data were collected at a rate of two degrees per minute between 5 to 60 degrees 2θ (Harrison and Curtin, 2021).

4.7 Statistical Analysis

The difference in BC production, including weight, was analyzed statistically by using Two-way analysis of variance (ANOVA).

5.0 RESULTS AND DISCUSSION

Results should be clear and concise. A combined Results and Discussion section is often appropriate. This section should discuss the significance of the results of the research. Avoid extensive citations and discussion of published literature.

5.1 The effect of co-culture SCOBY with *Saccharomyces cerevisiae*, "Tapai" yeast, optimised mass of "Tapai" yeast on BC fresh weight and dry weight in static culture.

Figure 1 reveals that co-culturing SCOBY with "Tapai" yeast significantly boosted bacterial cellulose (BC) production above the control and SCOBY with *S. cerevisiae*. The control yielded the lowest fresh weight (3.10 ± 0.03 g), whereas "Tapai" yeast increased it to 8.48 ± 0.46 g, with the highest yield at 0.15 g inoculum

(10.71 ± 0.19 g). In comparison, *S. cerevisiae* produced a moderate yield (4.49 ± 0.13 g). The superior effect of "Tapai" yeast originates from its varied microorganisms, which hydrolyse complex carbohydrates and give compounds that stimulate acetic acid bacteria activity, hence supporting cellulose biosynthesis (Montenegro-Silva et al., 2024).

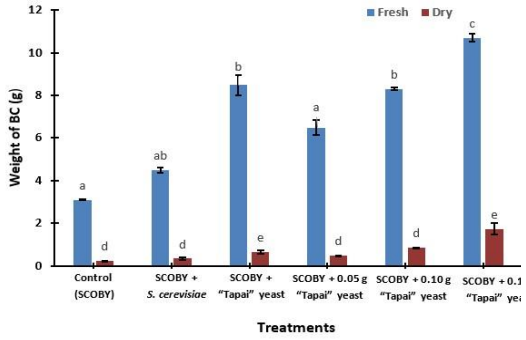

Fig. 1: The effect of co-culture SCOBY with Saccharomyces cerevisiae, "Tapai" yeast, optimised mass of "Tapai" yeast (0.05 g, 0.10 g and 0.15 g) on BC fresh and dry weight in static culture

S. cerevisiae had a moderate increase in BC yield (4.49 ± 0.13 g fresh weight) compared to the control, which is consistent with Venegas et al.'s (2023) findings that alcohol synthesis stimulates BC without the hydrolytic enzymes found in "Tapai" yeast. This illustrates the benefit of "Tapai" yeast, which converts complex polysaccharides into fermentable sugars. A similar pattern was seen in dry weight, with "Tapai" yeast at 0.15 g producing the maximum yield. Both yeasts increased BC production compared to the control, most likely due to metabolic intermediates used by AAB in the SCOBY. These metabolites stimulate the cellulose synthase, ATP, and acetyl-CoA pathways, indicating that BC production in co-culture is strongly dependent on the yeast strain employed (Wang et al., 2016).

5.2 The effects of different yeast co-cultures on BC thickness

Figure 2 depicts the influence of yeast co-culture on BC thickness. The control group produced the thinnest pellicle (3.4 ± 0.2 mm). However, co-culturing SCOBY with "Tapai" yeast considerably increased thickness, reaching 5.5 ± 0.5 mm at 0.15 g, which was statistically larger ($p < 0.05$) than both the control and *S. cerevisiae*. This enhancement is most likely owing to better interactions between yeast and acetic acid bacteria, which aid in polymerisation and fibril formation. Similar findings were reported by Chawla et al. (2009), who discovered that optimised yeast co-cultures improve thicker cellulose synthesis by increasing metabolic intermediate availability. *S. cerevisiae* co-culture produced thinner BC (4.2 ± 0.2 mm), indicating a lesser enzymatic contribution compared to the varied metabolic activity of "Tapai" yeast.

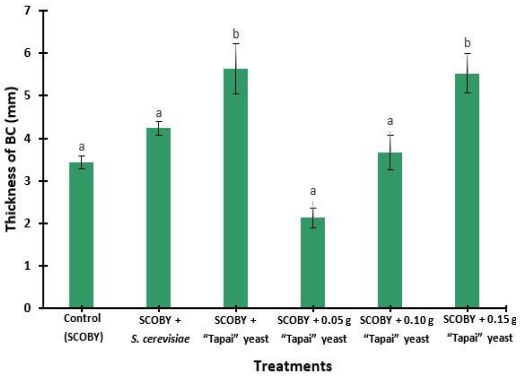

Fig. 2: The effect of co-culture SCOBY with *Saccharomyces cerevisiae*, "Tapai" yeast, optimised mass of "Tapai" yeast (0.05 g, 0.10 g and 0.15 g) on BC fresh and dry weight in static culture.

Yeast co-fermentation resulted in thicker BC pellicles, which is consistent with Brugnoli et al.'s (2023) finding that mixed consortia increase BC structure

when compared to monocultures. This boost is due to the clustering of BC nanofibres, which increases density and mechanical strength. In this study, yeast-AAB collaboration created a favourable biochemical environment for BC synthesis by: (i) enzymatic hydrolysis of complex carbohydrates, supplying steady sugars; (ii) ethanol and organic acid production, influencing pH and cellulose synthase activity; and (iii) the release of intermediates that enhance fibril polymerisation. These processes promote β-1,4-glycosidic bond formation and tighter fibril aggregation, resulting in denser and less porous pellicles. Such structural changes improve strength, water retention, and barrier qualities, emphasising co-culture fermentation as a scalable pathway for improved cellulose biomaterials.

5.3 The effects of different yeast co-cultures on BC fresh and dry weight

Table I reveals that the maximum BC yield was reached with 0.15 g "Tapai" yeast (0.56 ± 0.19 g/g fresh weight, 0.097 ± 0.25 g/g dry weight), which outperformed *S. cerevisiae* (0.25 ± 0.13 g/g; 0.018 ± 0.05 g/g) and the control (0.17 ± 0.03 g/g; 0.002 ± 0.03 g/g). The better efficiency of "Tapai" yeast is due to its microbial variety, as amylolytic and saccharolytic species offer continuous fermentable sugars to fuel AAB metabolism, as shown by Goh et al. (2012). In contrast, *S. cerevisiae exclusively* produces ethanol and lacks enzymes that hydrolyse complex carbohydrates, resulting in rapid substrate depletion. The inadequate control yield emphasises the importance of various yeast consortia for efficient BC synthesis.

TABLE I: The BC yield of fresh weight and dry weight of BC produced

Parameters	Fresh weight (g)	Dry weight (g)
Control	0.17 ± 0.03	0.002 ± 0.03
Saccharomyces cerevisiae	0.25 ± 0.13	0.018 ± 0.05
0.12 g/250 ml "Tapai" yeast	0.47 ± 0.46	0.035 ± 0.07
0.05 g/250 ml "Tapai" yeast	0.36 ± 0.35	0.027 ± 0.01
0.10 g/250 ml "Tapai" yeast	0.46 ± 0.06	0.047 ± 0.01
0.15 g/250 ml "Tapai" yeast	0.56 ± 0.19	0.097 ± 0.25

5.4 The effects of co-culture on the presence of BC functional groups

FTIR spectra of all materials showed a large peak at 3330 cm^{-1}, corresponding to -OH stretching and hydrogen bonding characteristic of cellulose (Ryngajłło et al., 2023). This peak was more prominent in BC from 0.15 g "Tapai" yeast, indicating more purity and less contaminants like proteins or polysaccharides. The C-H stretching band at 2900 cm^{-1} and β-glycosidic bond peak at 1160 cm^{-1} were sharper, indicating more polymerisation and crystallinity. Additional peaks at 1640 cm^{-1} (water absorption) and 1750 cm^{-1} (C-H deformation) were also detected. Compared to *S. cerevisiae* and the control, "Tapai" yeast treatments had clearer peaks and better structural integrity. These findings, which agree with Hamed et al. (2022), show that co-cultures improve BC purity, molecular order, and application potential.

5.5 The effects of co-culture on BC Crystallinity

XRD examination (Figures 3 and 4) showed significant changes in BC crystallinity between treatments. All samples showed cellulose I peaks, with sharp reflections at 2θ = 15° and 22°, which correspond to the (101) and (002) planes. BC from "Tapai" yeast produced sharper, more intense peaks, with 0.15 g yielding the greatest crystallinity index (CrI = 84.2%), indicating well-organised fibrils. In contrast, BC from *S. cerevisiae* displayed larger, weaker peaks, indicating poorer crystallinity (CrI = 68.5%) and increased structural disorder. The control showed significantly less-defined peaks, indicating the reduced order. These findings reveal the improved structural organisation induced by "Tapai" yeast, emphasising the importance of microbial diversity in increasing BC crystallinity.

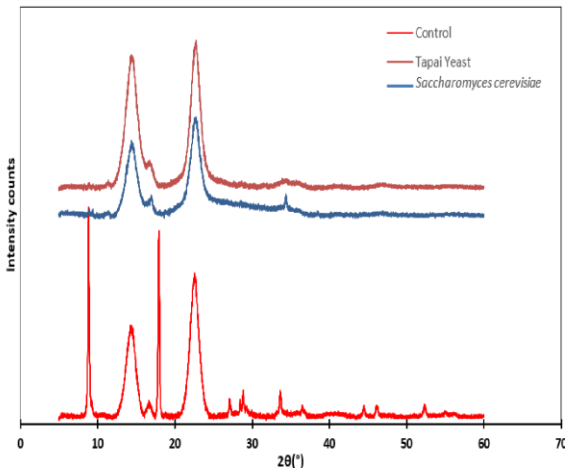

Fig. 3: Crystallite indices determination of Control, *Saccharomyces cerevisiae* and "Tapai" yeast.

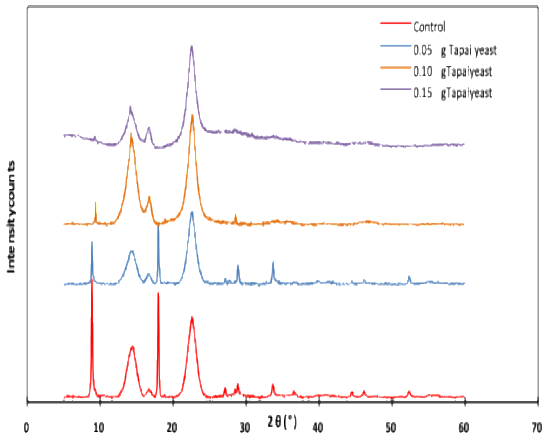

Fig. 4: Crystallite indices determination of Control, 0.05 g "Tapai" yeast, 0.10 g "Tapai" yeast and 0.15 g "Tapai" yeast.

The control group showed the weakest diffraction peaks (CrI = 61.3%), indicating inadequate fibril alignment and low crystallinity. The increased crystallinity found in the "Tapai" yeast treatments can be attributed to the yeast's metabolic activity, which offers an optimal environment for cellulose production and fibril structure. Laavanya et al. (2021) found similar results, stating that co-culturing yeast with *Koma-gataeibacter* increased BC crystallinity by promoting optimum microbial interactions. Increased crystallinity improves mechanical strength and thermal stability, making the BC better suited for industrial applications.

6.0 CONCLUSION

In comparison to *S. cerevisiae* and the control, "tapai" yeast was a successful co-cultivator for SCOBY, greatly increasing the BC output, thickness, functional group distribution and crystallinity. Its various enzymes provide steady flow of sugar and prolonged acetic acid bacterial activity, which produces BC that is stronger and purer. With potential uses in packaging, biomedical materials,

and sustainable fabrics, this low-cost, culturally accessible method provides a scalable route for generating high-quality BC.

ACKNOWLEDGEMENTS

The authors would like to convey their gratitude to the Faculty of Science and Marine Environment and Universiti Malaysia Terengganu (UMT), Malaysia for their ongoing assistance in facilitating this research.

REFERENCES

1. M. Brugnoli, I. Mazzini, S. La China, L. De Vero, and M. Gullo, "A microbial co-culturing system for producing cellulose–hyaluronic acid composites," *Microorganisms*, vol. 11, no. 6, p. 1504, 2023.

2. P. R. Chawla, I. B. Bajaj, S. A. Survase, and R. S. Singhal, "Microbial cellulose: Fermentative production and applications," *Food Technol. Biotechnol.*, vol. 47, no. 2, pp. 107–124, 2009.

3. X. Feng, Z. Ge, Y. Wang, Y. Zhang, J. Li, and X. Sun, "Production and characterization of bacterial cellulose from kombucha-fermented soy whey," *Food Prod. Process. Nutr.*, vol. 6, no. 20, 2024.

4. W. N. Goh, A. Rosma, B. Kaur, A. Fazilah, A. A. Karim, and R. Bhat, "Fermentation of black tea broth (Kombucha): I. Effects of sucrose concentration and fermentation time on the yield of microbial cellulose," *Int. Food Res. J.*, vol. 19, no. 1, pp. 109–117, 2012.

5. D. A. Hamed, H. Hamed, and H. Abdel-Kareem, "Biosynthesis of bacterial cellulose nanofibrils in black tea media by a symbiotic culture of bacteria and yeast," *World J. Microbiol. Biotechnol.*, vol. 39, no. 3, 2022.

6. K. Harrison and C. Curtin, "Microbial composition of SCOBY starter cultures used by commercial kombucha brewers in North America," *Microorganisms*, vol. 9, no. 5, p. 1060, 2021.

7. A. F. Jozala, V. A. Lencastre-Novaes, L. Lopes, J. M. de Carvalho Santos-Ebinuma, M. M. Seckler, A. Pessoa, … and M. Gama, "Bacterial nanocellulose: Long-term perspectives and novel applications," *Braz. J. Microbiol.*, vol. 52, no. 1, pp. 115–125, 2021.

8. J. Jung, Y. Park, H. Kim, and S. Lee, "Advances in microbial co-cultivation strategies for enhanced bacterial cellulose production," *Biotechnol. Adv.*, vol. 62, p. 108092, 2025.

9. D. Kim, J. Park, and C. Lee, "Adaptive evolution of *Komagataeibacter* species for improved bacterial cellulose production," *Carbohydr. Polym.*, vol. 315, p. 120987, 2024.

10. D. Laavanya, S. Shirkole, and P. Balasubramanian, "Current challenges, applications and future perspectives of SCOBY cellulose of kombucha fermentation," *J. Clean. Prod.*, vol. 295, p. 126454, 2021.

11. F. Mauro, B. Corrado, V. De Gregorio, E. Lagreca, C. Di Natale, R. Vecchione, and P. Netti, "Exploring the evolution of bacterial cellulose precursors and their potential use as cellulose-based building blocks," *Sci. Rep.*, vol. 14, p. 62462, 2024.

12. P. Montenegro-Silva, J. De Souza, A. Dias, and V. Santos, "Enhanced bacterial cellulose production in *Komagataeibacter sucrofermentans*: Impact of different PQQ-dependent dehydrogenase knockouts and ethanol supplementation," *Biotechnol. Biofuels Bioprod.*, vol. 17, no. 35, 2024.

13. R. Portela, C. R. Leal, P. L. Almeida, and R. G. Sobral, "Bacterial cellulose: A

versatile biopolymer for wound dressing applications," *Microb. Biotechnol.*, vol. 12, no. 4, pp. 586–610, 2019.

14. M. Ryngajłło, K. Kubiak, P. Jacek, S. Bielecki, and A. M. Kołodziejczyk, "Effect of ethanol supplementation on the transcriptional response of *Komagataeibacter xylinus*," *AMB Express*, vol. 9, p. 102, 2019.

15. E. Uțoiu, V. Manoiu, E. Oprița, and O. Crăciunescu, "Bacterial cellulose: A sustainable source for hydrogels and 3D-printed scaffolds for tissue engineering," *Gels*, vol. 10, no. 6, p. 387, 2024.

16. C. Venegas, J. Palacios, and P. Villalobos, "Effect of pH dynamics on bacterial cellulose production in co-culture systems," Biotechnol. Rep., vol. 40, p. e00772, 2023.

17. A. Wahid, J. J. Yin, D. Xue, H. Xue, Y. S. Lu, C. Zhong, and L. Q. Chu, "Co-culture strategies for bacterial cellulose production: A review," *Carbohydr. Polym.*, vol. 270, p. 118370, 2022.

18. S. S. Wang, Y. H. Han, J. L. Chen, D. C. Zhang, X. X. Shi, Y. X. Ye, and F. F. Li, "Insights into bacterial cellulose biosynthesis from different carbon sources," *Carbohydr. Polym.*, vol. 185, pp. 63–76, 2016.

19. C. Zhong, Z. Xu, Y. Xie, Q. Yang, and G. Chen, "Production of bacterial cellulose–hyaluronic acid composites using co-culture systems," *Int. J. Biol. Macromol.*, vol. 242, p. 124983, 2023.

Structural Characterization of Erbium-doped Zinc Tellurite Glass Modified with Antimony Oxide Towards the Development of Materials for Optical Amplifier

Muhammad Hazmi Che Ku Abu **Bakar**[1], Hafizah Noor **Isa**[1*]

[1]Department of Physics, Kulliyyah of Science, International Islamic University Malaysia, Jalan Sultan Ahmad Shah, 25200 Kuantan, Pahang, Malaysia.

*Corresponding author's phone: +60 18-988 4407
E-mail: hafizahnoorisa@iium.edu.my

Received: 10 September 2025; Accepted:13 October 2025

ABSTRACT

Tellurite (TeO_2) glass has attracted significant attention in nanomaterial research due to its high solubility of rare-earth doping, making them as promising host materials for rare earth ion doping like erbium (Er^{3+}). These properties are mainly due to its structural feature that contains lone pair electron (LPE) within TeO_2 structural units which contributes to the linear and non-linear optical properties. Notably, with these properties, Er^{3+}-doped TeO_2 glass has the potential application in optical amplifier. However, the presence of this LPE also prevent TeO_2 to form a stable glass on its own under conventional melt quenching method. In this study, we show that the addition of modifiers like zinc oxide (ZnO) and a small concentration of antimony oxide (Sb_2O_3) can enhance the network stability of TeO_2 glass as well as improving its properties. A series of 60 TeO_2 – 40 ZnO – xSb_2O_3 – yEr_2O_3 ($0 < x < 1$ mol%, $0 < y < 3$ mol%) glasses were synthesized using melt quenching technique under controlled parameter, and the structural properties of the glasses were investigated using x-ray diffraction (XRD) analysis and Fourier transform infrared (FTIR) spectroscopy. XRD analysis shows no crystalline peak, revealing the amorphous structure for all samples. The FTIR spectra show the strong absorption at 690 cm^{-1} for all samples, indicating the TeO_3-rich environment in the glass network due to the high concentration of ZnO. The addition of Sb_2O_3 and Er_2O_3 alters the short-range structural environment in TeO_2 glass mostly on the TeO_3 unit as observed in the shifting in the region 700 – 800 cm^{-1}. Our findings show that these structural modifications can heavily impact optical properties such as the absorption and luminescence which could mostly be desired for optical and photonics applications like optical amplifiers. Future study can be done to explore its optical performance, such as the absorption, emission spectra, and fluorescence lifetime measurements, to evaluate their effectiveness as rare-earth-doped materials for optics and photonics application.

Keywords— Tellurite glass; rare-earth; FTIR spectroscopy; XRD analysis; and optical amplifier

1.0 INTRODUCTION

Recently, the studies of rare-earth ions doping have attracted various attentions from the researchers because of its frequent utilisation to improve the physical and optical properties of the glass host [1]. Among these rare-earth ions, erbium ion (Er^{3+}) possesses efficient broadband emission and can amplify light at 1.53 μm, a key wavelength in fibre optics [2]. Notably, with these properties, Er^{3+}-doped glass has potential applications in optical amplifiers. To achieve the full potential of Er^{3+} doping, a suitable host material is needed to ensure efficient luminescence and minimal non-radiative losses. The host material should possess low phonon energy, high rare-earth

solubility, and good thermal and chemical stability to help maintain the emission efficiency of Er^{3+} ions. For the past years, researchers have used oxide glasses because of their high chemical durability, thermal stability, and excellent insulating and optical properties, which make them suitable to be utilised as host materials for rare-earth doping. Nonetheless, there are challenges remaining in identifying a suitable combination of oxides as host systems that can balance glass-forming ability with desirable optical performance. This study focuses on Er^{3+}-doped zinc tellurite glasses modified with antimony(III) oxide (Sb_2O_3), aiming to address these challenges and explore their structural suitability for optical amplifier applications.

2.0 THEORY/LITERATURE REVIEW

Tellurite (TeO_2) glass has been widely investigated for its unique optical properties, such as broad transmission range around 0.4 to 6 μm, high nonlinear refractive index, and low phonon energies between 700 and 900 cm^{-1} [3]. In addition, TeO_2-based glass also possesses a high solubility for rare-earth ions, which makes it a promising candidate for a host material for rare-earth doping [4]. However, it is difficult to prepare TeO_2 glass under the conventional melt quenching technique [5]. The configuration of TeO_2 glass is similar to TeO_2 crystal, which makes the network structure of TeO_2 highly compact and rigid. This makes TeO_2 favour crystallisation during the quenching process. To bypass crystallisation, TeO_2 needs to be quenched at an exceedingly high rate [6]. An easier way to fabricate TeO_2 glass through melt quenching is by adding the other oxides like zinc oxide (ZnO) and antimony(III) oxide (Sb_2O_3) into TeO_2 glass to promote its glass-forming ability [7]. ZnO can reduce the rigidity of the TeO_2 glass network by transforming the high coordination of the TeO_4 trigonal bipyramidal (tbp) unit into a lower coordination unit like TeO_3 trigonal pyramid (tp) unit, which is less rigid [8]. Zinc tellurite glass shows great potential for optical properties due to its high refractive index, wide transmission window, and non-linear optical behaviour [9], [10]. In addition, Sb_2O_3 is known as a glass stabiliser and a source of non-linear optical properties, such as high non-linear refractive index [11]. Sb_2O_3 can also act as both network formers and network modifiers, depending on their coordination environment [12]. Therefore, the inclusion of ZnO and Sb_2O_3 plays a significant role in altering the fundamental structural units of TeO_2 glass.

In terms of oxygen bonding, TeO_4 units are generally associated with bridging oxygen (BO), while TeO_3 units are linked to non-bridging oxygen (NBO) [13]. The conversion of TeO_4 to TeO_3 upon the addition of modifiers is crucial as the presence of BO and NBO in the glass is a key structural change that directly influences the optical properties of TeO_2-based glasses. Hence, to observe the ratio of BO and NBO within the glass structure, Fourier Transform Infrared (FTIR) spectroscopy is employed as it is a suitable method to detect the vibration modes associated with BO and NBO in TeO_2 glass. FTIR is chosen for its effectiveness in detecting the vibrational modes in the bonds, such as the stretching and bending vibration in distinctive structural groups that represent the glass matrix [14]. In this study, the FTIR spectroscopy was used to analyse the structural characteristics of Er^{3+}-doped zinc tellurite glass by identifying the vibrational modes of the chemical bonds within the glass network. The identification helps to determine the structural evolution of TeO_2 glass with the addition of the modifiers, such as ZnO, Er_2O_3 and Sb_2O_3.

3.0 MATERIALS

Tellurium dioxide (>99.5%), zinc oxide (99.9%), antimony(III) oxide (99.999%), and erbium(III) oxide (99.9%) were purchased from Sigma Aldrich.

4.0 EXPERIMENTAL

A series of TeO_2 – ZnO – Sb_2O_3 – Er_2O_3 glasses were synthesized via melt quenching technique by varying the composition of the materials using the stoichiometric formula (60.0 − x − y) TeO_2 – 40.0 ZnO – x Sb_2O_3 – y Er_2O_3, where x = 0, 0.5, and 1.0 mol %, and y = 0, 1.5, 3.0, and 5.0 mol %. A total of 6 glass samples were prepared, and the composition of each sample was tabulated in Table 1. The required amount of tellurium dioxide (TeO_2), zinc oxide (ZnO), antimony(III) oxide (Sb_2O_3), and erbium(III) oxide (Er_2O_3) were calculated and weighed accordingly using a digital weight machine at a total of ~6 g. The powders were weighed and mixed homogeneously, transferred into an alumina crucible, and placed inside the furnace for the preheating process at 400 °C for 2 hours. After 2 hours, the crucible was transferred into another furnace for the melting process at 1100 °C for 1 hour. Then, the melted sample was cast on the preheated brass plate and annealed in the first furnace at 370 °C for 2 hours to remove the thermal stress that can cause the glass to develop cracks. Finally, the furnace is turned off to let the sample slowly cool to room temperature.

TABLE 1: Molar compositions of the glass material

Sample annotation	Molar percentage of the glass material (mol %)			
	TeO_2	ZnO	Sb_2O_3	Er_2O_3
S1	57.0	40.0	0.0	3.0
S2	55.0	40.0	0.0	5.0
S3	56.5	40.0	0.5	3.0
S4	56.0	40.0	1.0	3.0
S5	59.5	40.0	0.5	0.0
S6	58.0	40.0	0.5	1.5

The structural properties of the glasses were assessed using x-ray diffractometer to determine their amorphous nature and Fourier Transform Infrared (FTIR) spectroscopy for the detection of functional groups in the glass network. The glasses were ground into a powder form and examined using Bruker D8 Advance x-ray diffractometer. The x-ray diffraction (XRD) analysis was carried out with CuK_α radiation source of wavelength λ = 1.5406 Å at the range 2θ between 10° to 80°. For FTIR analysis, the spectra were recorded using PerkinElmer Frontier FT-IR. The KBr pellet technique was employed, and the analysis was carried out in the range of 400 – 4000 cm^{-1}. All the measurements were done at the resolution of 4.0 cm^{-1}.

5.0 RESULTS AND DISCUSSION

5.1 X-Ray Diffraction (XRD)

Fig. 1 shows the x-ray diffraction (XRD) spectra of the glasses that were scanned from 10° to 80° of 2θ. It is observed that there are no visible sharp peaks, which indicates the properties of the amorphous structure. There were observable broad humps at 20° to 35° for all samples, which indicate the short-range order in the glass network [15]. From the XRD spectra, it can be concluded that amorphous Er^{3+}-doped zinc tellurite glasses modified with Sb_2O_3 have been successfully prepared via the melt quenching technique.

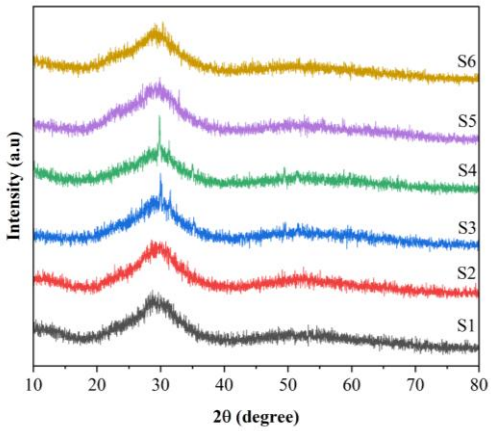

Fig. 1: XRD spectra of Er^{3+}-doped zinc tellurite glasses series at various compositions.

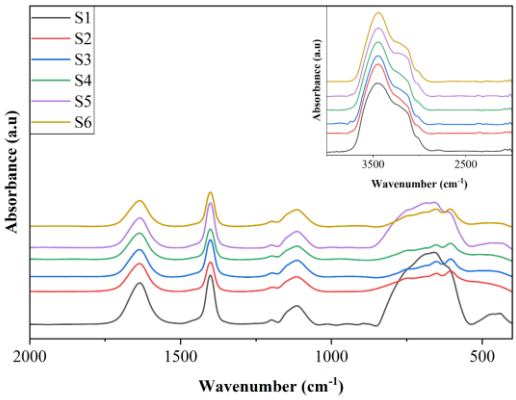

Fig. 2: FTIR absorption spectra of (60-x-y) TeO_2 – 40 ZnO – x Sb_2O_3 – y Er_2O_3 glass series at various compositions from 2000 – 400 cm^{-1}, and the inset is the same FTIR spectra from 4000 – 2000 cm^{-1}.

5.2 Fourier Transform Infrared (FTIR)

Fig. 2 shows the FTIR spectra of (60-x-y) TeO_2 – 40 ZnO – x Sb_2O_3 – y Er_2O_3 glass series, where x and y were varied in the range of $0 < x < 1.0$ mol% and $0 < y < 5.0$ mol%, given in Table 1. All spectra exhibit several characteristic absorption features within the 400 – 4000 cm^{-1} range, as shown in the inset graph in Fig. 2, indicating the presence of various vibrational modes in the glass structure. A broad absorption band appears in the region of 3100 – 3700 cm^{-1} for all spectra, typically attributed to the stretching vibration of the OH group [16], [17]. The presence of this group suggests that there might be water content or moisture trapped during the grounding process of the glass powder and KBr. There is a broad absorption peak around ~1650 cm^{-1} that appears for all samples, which is related to the bending vibration of OH bonds [17], [18], [19]. There is a sharp absorption band centred at ~1400 cm^{-1} detected for all samples, which is unusual for ZnO-TeO_2-based glass. Usually, this band is assigned to the carbonate (CO_3^{2-}) or nitrate (NO_3^{2-}) impurities [20]. This band might arise due to the atmospheric CO_2 during the preparation of KBr pellet. Nevertheless, the persistence of this band across all compositions also raises the possibility of a new bonding environment related to zinc tellurite glass, which would require complementary techniques such as Raman spectroscopy or nuclear magnetic resonance (NMR) to confirm it. There is also an absorption peak detected at ~1120 cm^{-1} with a shoulder at ~1193 cm^{-1} attributed to the Te-O-Zn linkages [17], [21]. These peaks seem not to be affected by the change in the compositions. On top of that, several prominent bands appear in the region 1000 – 400 cm^{-1}. All samples exhibit a broad absorption band that spans between 400 – 800 cm^{-1}. The observed broadening of the bands can be either from the overlapping of some individual bands or the distribution of the bond angles, the bond lengths, and the fluctuations of the local electronic and atomic environments in the amorphous state [22]. Therefore, it is necessary to carry out the deconvolution to separate those peaks. The deconvolution was carried out using Gaussian function, and the parameters such as the peak centre (C) and the relative area of the band (A) were recorded in Table 2, and the deconvolution of the spectra is shown in Fig. 3.

As seen in the deconvolution data and spectra in Table 2 and Fig. 3, all six samples exhibit a common absorption feature that spans the region from approximately 400 cm^{-1} to 900 cm^{-1}. This broad absorption is an envelope of seven absorption bands, representing the vibration modes of Te-O and Zn-O. Table 3 shows the band assignments of the functional group for TeO_2 glass. At low concentration of modifiers (x + y < 3.0 mol%), as observed in S1, S5, and S6, a strong absorption band dominates in the region 690 – 700 cm^{-1}, indicating that the glass network in these samples is primarily composed of TeO_3 structural units. This is mainly due to the high concentration of ZnO, which breaks down the bridging oxygens of TeO_2 glass network (Te-O-Te) to form the NBOs, which reduces the formation of TeO_4 units and creates more TeO_3 units [23], [24]. Upon the inclusion of modifiers, several peak centres show variations, indicating the structural modification of the zinc tellurite glass network. When the total modifier contents exceed 3.0 mol% (x + y > 3.0 mol%), the band centred at ~430 cm^{-1}, related to the stretching vibration of Zn-O or bending vibration of Te-O-Te linkages [14], [25], [26], gradually diminishes and shifts toward higher wavenumber, around ~460 cm^{-1}. This behaviour may relate to the decrease of Zn-O bonds in the glass, which agrees with the literature [26]. Similarly, the band at ~470 cm^{-1}, also assigned to Te-O-Te linkages, shifts to a higher wavenumber, around ~550 cm^{-1}, suggesting the transformation of weaker bending vibrations of Te-O-Te linkages into

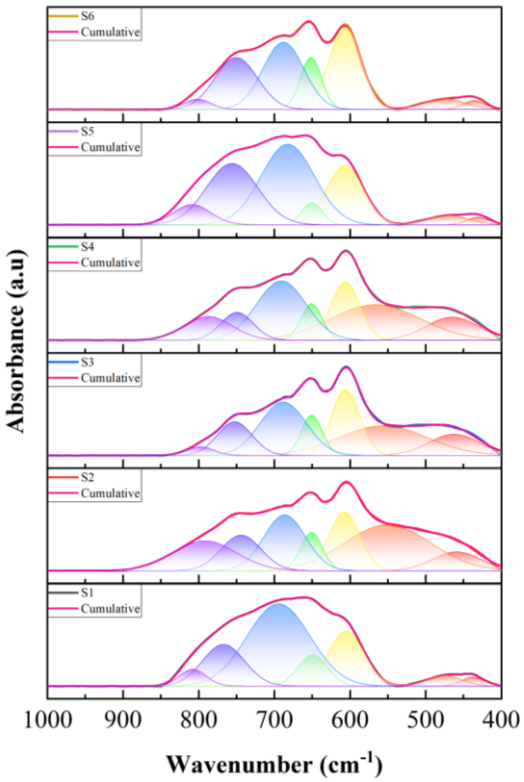

Fig. 3: The deconvolution of FTIR spectra in the region 400 – 1000 cm^{-1} for all samples.

TABLE 2: The deconvolution parameters of FTIR spectra of (60.0 − x − y) TeO_2 – 40.0 ZnO – x Sb_2O_3 – y Er_2O_3 glass in the region 400 – 1000 cm^{-1}, where C is the centre of deconvoluted band (cm^{-1}) and A is the relative area fraction of deconvoluted band (%).

Sample	Molar percentage (mol%)		The centre of deconvoluted band, C (cm^{-1}) and the relative area fraction of deconvoluted band, A (%).							
S1	x = 0	C	437	475	-	605	649	694	767	808
	y = 3.0	A	1.90	3.43	-	18.09	8.52	47.72	16.18	4.16
S2	x = 0	C	-	459	550	607	651	686	744	792
	y = 5.0	A	-	6.70	30.04	13.74	6.31	17.88	10.89	14.43
S3	x = 0.5	C	-	462	556	606	651	688	752	798
	y = 3.0	A	-	10.25	25.37	18.24	8.18	24.21	11.48	2.27
S4	x = 1.0	C	-	465	566	606	651	691	749	787
	y = 3.0	A	-	9.90	26.88	14.35	6.53	25.11	7.64	9.60
S5	x = 0.5	C	431	471	-	607	650	682	756	809
	y = 0	A	1.46	3.32	-	19.18	3.97	37.75	27.73	6.58
S6	x = 0.5	C	436	474	-	606	652	688	750	802
	y = 1.5	A	1.99	4.66	-	27.38	11.47	28.65	23.04	2.80

Table 1: FTIR band assignment in the spectra of TeO_2 glass.

Wavenumber (cm^{-1})	Assignment	Reference
430 – 470	The bending vibration from Te-O-Te or O-Te-O linkages or the stretching vibration of Zn-O in ZnO_4 tetrahedra.	[14], [25], [26]
545 – 590	The stretching vibrations of Te-O-Te bond between TeO_4 and bridging oxygen.	[26], [27]
600 – 650	The stretching vibration of Te-O in TeO_4 tbp.	[15], [28]
650 – 700	The stretching vibration of Te-O in TeO_3 tp.	[15], [24]
740 – 770	The vibration modes of TeO_3 tp or distorted TeO_{3+1}.	[4], [34], [35]
780 – 810	The stretching mode of Te-O with non-bridging oxygen.	[27], [36]

stronger stretching vibrations associated with Te-O-Te bonds involving BO in TeO_4 units [26], [27]. Meanwhile, the bands at ~600 – 650 cm^{-1} that relate to TeO_4 tbp structure remain nearly unchanged for all samples [15], [28]. It is implied that this specific vibrational mode is less affected by the modifiers. However, it is worth noting that these bands appear as a partially overlapped doublet at low concentration of modifiers. Upon the addition of Er_2O_3 and/or Sb_2O_3, the two centres at ~600 cm^{-1} and ~650 cm^{-1} become more widely separated, implying the changed in local environment of Te atoms. The modifiers like Sb_2O_3 and Er_2O_3 can distort the TeO_4 unit, which could alter its bond lengths and angles, thus leading to the splitting of the vibrational modes and the appearance of two distinct peaks in the FTIR [29]. On the other hand, in the region 650 – 800 cm^{-1} corresponding to TeO_3 tp units, the peak centres exhibit significant shifts compared to the nearly unchanged bands at 600 – 650 cm^{-1}, indicating that TeO_3 units are more sensitive to structural modification from the inclusion of Sb_2O_3 and Er_2O_3. This behaviour might suggest that Sb_2O_3 and Er_2O_3 may have alter the bond lengths and angles from TeO_3 unit more than from TeO_4 unit, which explained the shift of peak centres.

To evaluate the effect of Sb_2O_3 and Er_2O_3 on the formation of BO and NBO in $ZnO\text{-}TeO_2$ glass, the relative fraction area of the deconvoluted band (A) can be used, as it reflects the concentration of the structural unit associated with each peak centre. The relations in (1) and (2) can be used to evaluate the concentration of TeO_4 and TeO_3 units [30]:

$$P_{TeO4} = \frac{A_{TeO4}}{A_{TeO4} + A_{TeO3}} \times 100\% \quad (1)$$

$$P_{TeO3} = \frac{A_{TeO3}}{A_{TeO4} + A_{TeO3}} \times 100\% \quad (2)$$

where P_{TeO4} and P_{TeO3} refers to the percentage fraction area of TeO_4 and TeO_3 unit, while A_{TeO4} and A_{TeO3} is the collective area of TeO_4 and TeO_3 unit, respectively. These relations can be used to evaluate the presence of BO and NBO in $ZnO\text{-}TeO_2$,

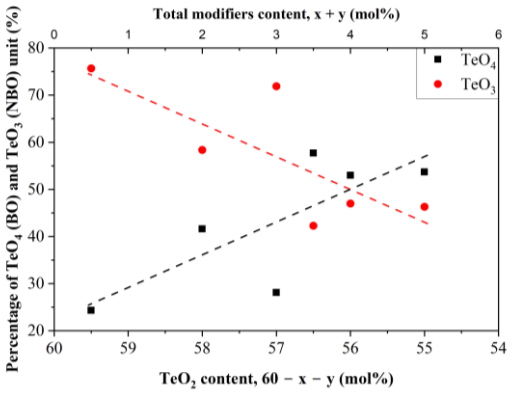

Fig. 4: Variation of TeO_4 and TeO_3 with the concentration of modifiers at the expense of TeO_2. The dashed line represents the trendline of the plot.

since TeO_4 units are typically associated with BOs, while TeO_3 are linked with NBOs. Fig. 4 shows the plot of percentage area for TeO_4 and TeO_3 vs the concentration of TeO_2. Based on Fig. 4, it shows the variation of TeO_4 and TeO_3 units with the decrease of TeO_2 induced by the addition of Sb_2O_3 and Er_2O_3. For S5, S6, and S1, TeO_3 unit is higher than TeO_4, which implied that the content of NBO is high in these samples. The high NBO content is due to the high concentration of ZnO, as discussed above. As the modifiers increase at the expense of TeO_2, the fraction of TeO_3 units decrease while TeO_4 units increase, indicating the creation of BO in the glass network. For S3, S4, and S2, the inclusion of modifiers at the expense of TeO_2 leads to a more balanced ratio of BO and NBO units within the glass network, as reflected in the graph. This is crucial as it will impact the functionality of the glass. Excessive NBOs are known to weaken the network connectivity, which could reduce the overall stability of the glass network [31]. On the contrary, too little NBO could potentially reduce the refractive index of the glass, as the presence of NBO has been correlated with an increase in the refractive index of various glass systems [32], [33]. A glass network that maintains both BO and NBO units in proportion is more likely to combine mechanical durability with favourable optical characteristics, an important quality for glasses intended for photonic applications, where stability and high refractive index must coexist.

6.0 CONCLUSION

In conclusion, a series of ZnO-TeO_2 glasses with a stable glass network have been successfully fabricated by adding Er_2O_3 and Sb_2O_3. The structural properties of the fabricated glasses were characterized using XRD and FTIR spectroscopy. XRD patterns confirmed the amorphous nature of all samples while the FTIR results revealed the absorption bands at 400 – 1000 cm^{-1}, 1120 – 1190 cm^{-1}, 1400 cm^{-1}, 1650 cm^{-1}, and 3100 – 3700 cm^{-1}. To resolve the overlapping bands in the 400 – 1000 cm^{-1}, a deconvolution analysis was performed, which revealed seven distinct absorption bands corresponding to the vibration modes of Te-O and Zn-O. At low concentration of modifiers, the band at ~690 – 700 cm^{-1} appeared as the most intense, indicating the NBO-rich environment in the glass. As the modifiers increased, the intensity of the band decreased, suggesting the reduction in NBO and a transition towards a more balanced distribution of BOs and NBOs.

ACKNOWLEDGEMENTS

The authors would like to express sincere gratitude towards i-CRIM Lab, UKM, and Kulliyyah of Science, IIUM for providing the service analysis of XRD and FTIR used in this study.

REFERENCES

1. S. O. Adeleye, A. A. Adeleke, P. Nzerem, A. I. Olosho, E. N. Anosike-Francis, T. S. Ogedengbe, P. P. Ikubanni, R. A. Saleh, J. A. Okolie. “A Review of the Physical, Optical and Photoluminescence Properties of Rare Earth Ions Doped Glasses,” Trends in Sciences, vol. 21, no. 12, pp. 8759, 2024.
2. P. Vani, G. Vinitha, and N. Manikandan, “Structural, luminescence and nonlinear optical properties of erbium doped barium tellurite glasses for photonic applications,” Journal of Materials Science: Materials in Electronics, vol. 34, no. 1, pp. 1–22, 2023.
3. E. A. Anashkina, “Laser Sources Based on Rare-Earth Ion Doped Tellurite Glass Fibers and Microspheres,” Fibers, vol. 8, no. 5, 2020.
4. Y. Sun, A. Chen, J. Yang, K. Zhang, S. Wang, X. Xu, L. Niu, Y. Jing, C. Wang, L. Ren, J. Zhang, “Net gain in C+L band from LED pumped broadband emission in Er3+-doped oxyhalide tellurite glass,” Ceram Int, vol. 50, no. 11, pp. 18968–18976, 2024.

5. G. Torun, T. Kishi, D. Pugliese, D. Milanese, and Y. Bellouard, "Formation Mechanism of Elemental Te Produced in Tellurite Glass Systems by Femtosecond Laser Irradiation," Advanced Materials, vol. 35, no. 20, p. 2210446, 2023.
6. V. Tomar, R. Pandey, and P. Singh, "Influence of quenching rate and quenching media on formation of TeO2 glasses," Journal of Materials Science: Materials in Electronics, vol. 32, no. 13, pp. 17726–17740, 2021.
7. J. Hrabovsky, L. Strizik, F. Desevedavy, S. Tazlaru, M. Kucera, L. Nowak, R. Krystufek, J. Mistrik, V. Dedic, V. Kopecky Jr, G. Gadret, "Optical, magneto-optical properties and fiber-drawing ability of tellurite glasses in the TeO2–ZnO–BaO ternary system," J Non Cryst Solids, vol. 624, p. 122712, 2024.
8. V. Kozhukharov, H. Bürger, S. Neov, and B. Sidzhimov, "Atomic arrangement of a zinc-tellurite glass," Polyhedron, vol. 5, no. 3, pp. 771–777, 1986.
9. M. Elisa, R. C. Stefan, I. C. Vasiliu, S. M. Iordache, A. M. Iordache, B. A. Sava, L. Boroica, M. C. Dinca, A. V. Filip, A. C. Galca, C. Bartha, "A New Zinc Phosphate-Tellurite Glass for Magneto-Optical Applications," Nanomaterials, vol. 10, no. 9, pp. 1875, 2020.
10. M. K. Halimah, A. A. Awshah, A. M. Hamza, K. T. Chan, S. A. Umar, and S. H. Alazoumi, "Effect of neodymium nanoparticles on optical properties of zinc tellurite glass system," Journal of Materials Science: Materials in Electronics, vol. 31, no. 5, pp. 3785–3794, 2020.
11. G. Jagannath, B. Eraiah, A. Gaddam, H. Fernandes, D. Brazete, K. Jayanthi, K. N. Krishnakanth, S. Venugopal Rao, J. M. Ferreira, K. Annapurna, A. R. Allu, "Structural and Femtosecond Third-Order Nonlinear Optical Properties of Sodium Borate Oxide Glasses: Effect of Antimony," Journal of Physical Chemistry C, vol. 123, no. 9, pp. 5591–5602, 2019.
12. Y. Hordieiev and A. Zaichuk, "Structural, thermal, and radiation shielding properties of antimony-doped zinc borate glasses," Sci Rep, vol. 15, no. 1, pp. 1–12, 2025.
13. M. Hongisto, A. Veber, Y. Petit, T. Cardinal, S. Danto, V. Jubera, L. Petit, "Radiation-Induced Defects and Effects in Germanate and Tellurite Glasses," Materials, vol. 13, pp. 3846, 2020.
14. N. R. Mohamad Azaludin and N. S. Sabri, "Infrared spectroscopy of mixed glass former effect in borotellurite glasses: A review," Gading Journal of Science and Technology, vol. 4, no. 1, pp. 94–102, 2021.
15. S. N. Nazrin, M. S. Sutrisno, H. B. Zaman, N. Jothi, A. Assaiqeli, and S. Ezzine, "Enhanced photoluminescence and optical properties of erbium-doped zinc tellurite glasses for visible and near-infrared photonic applications," J Lumin, vol. 281, pp. 121184, 2025.
16. P. Naresh, B. Kavitha, H. K. Inamdar, D. Sreenivasu, N. Narsimlu, C. Srinivas, V. Sathe, K. S. Kumar, "Modifier role of ZnO on the structural and transport properties of lithium boro tellurite glasses," J Non Cryst Solids, vol. 514, pp. 35–45, 2019.
17. S. K. Ghoshal, A. Awang, M. R. Sahar, and R. J. Amjad, "Spectroscopic and structural properties of TeO2-ZnO-Na2OEr2O3-Au glasses," Chalcogenide Letters, vol. 10, no. 10, pp. 411–420, 2013.
18. Y. B. Saddeek, "Network structure of molybdenum lead phosphate glasses: Infrared spectra and constants of elasticity," Physica B Condens Matter, vol. 406, no. 3, pp. 562–566, 2011.
19. M. Reza Dousti, M. R. Sahar, S. K. Ghoshal, R. J. Amjad, and A. R. Samavati, "Effect of AgCl on spectroscopic properties of erbium doped zinc tellurite glass," J Mol Struct, vol. 1035, pp. 6–12, 2013.

20. D. S. Volkov, O. B. Rogova, and M. A. Proskurnin, "Organic matter and mineral composition of silicate soils: FTIR comparison study by photoacoustic, diffuse reflectance, and attenuated total reflection modalities," Agronomy, vol. 11, no. 9, p. 1879, 2021.
21. M. R. Sahar, K. Sulhadi, and M. S. Rohani, "Spectroscopic studies of TeO2-ZnO-Er2O3 glass system," J Mater Sci, vol. 42, no. 3, pp. 824–827, 2007.
22. Y. B. Saddeek and N. Z. Elsayed, "Structural and mechanical features of some lanthanum tellurite glasses," Can J Phys, vol. 93, no. 4, pp. 460–465, 2015.
23. S. N. Nazrin, M. K. Halimah, and F. D. Muhammad, "Comparison study of optical properties on erbium-doped and silver-doped zinc tellurite glass system for non-linear application," Journal of Materials Science: Materials in Electronics, vol. 30, no. 7, pp. 6378–6389, 2019.
24. H. A. A. Sidek, S. Rosmawati, Z. A. Talib, M. K. Halimah, and W. M. Daud, "Synthesis and optical properties of ZnO-TeO 2 glass system," Am J Appl Sci, vol. 6, no. 8, pp. 1489, 2009.
25. S. K. Ahmmad, M. A. Samee, S. M. Taqiullah, and S. Rahman, "FT-IR and Raman spectroscopic studies of ZnF2–ZnO–As2O3–TeO2 glasses," Journal of Taibah University for Science, vol. 10, no. 3, pp. 329–339, 2016.
26. D. E. Fausta, A. Marzuki, and Cari, "Infrared absorption spectra analysis of TeO2-ZnO-Bi2O3-TiO2 doped B2O3 glasses," J Phys Conf Ser, vol. 1511, no. 1, p. 012076, 2020.
27. A. Azuraida, M. K. Halimah, M. Ishak, L. Hasnimulyati, and S. I. Ahmad, "GAMMA RAY SHIELDING PARAMETER OF BARIUM-BORO-TELLURITE GLASS," Chalcogenide Letters, vol. 17, no. 4, pp. 187–196, 2020.
28. R. Stefan, M. Karabulut, A. Popa, E. Culea, L. Bolundut, L. Olar, P. Pascuta, "A spectroscopic study of the influence of CuO addition on the ZnO-TeO2 glass and glass ceramics," J Non Cryst Solids, vol. 498, pp. 430–436, 2018.
29. L. Brand, V. Anjos, and M. J. V. Bell, "Optical and structural analysis of tellurite matrices with different modifiers," Opt Mater (Amst), vol. 138, pp. 113470, 2023.
30. Y. S. Rammah, N. A. M. Alsaif, Z. Y. Khattari, M. S. Shams, R. A. Elsad, and M. S. Sadeq, "Synthesis, physical, FTIR, and optical characteristics of B2O3·CaO·ZnO glasses doped with Nb2O5 oxide: Experimental investigation," Journal of Materials Science: Materials in Electronics, vol. 33, no. 30, pp. 23749–23760, 2022.
31. J. E. Shelby, "Introduction to Glass Science and Technology," Introduction to Glass Science and Technology, 2020.
32. A. S. Asyikin, M. K. Halimah, A. A. Latif, M. F. Faznny, and S. N. Nazrin, "Physical, structural and optical properties of bio-silica borotellurite glass system doped with samarium oxide nanoparticles," J Non Cryst Solids, vol. 529, p. 119777, 2020.
33. Y. Zhu et al., "Concentration dependent structural, thermal and luminescence properties in Er3+/Tm3+ doped tellurite glasses," J Non Cryst Solids, vol. 507, pp. 19–29, 2019.
34. H. Elkholy, H. Othman, I. Hager, M. Ibrahim, and D. de Ligny, "Europium-Doped Tellurite Glasses: The Eu2+ Emission in Tellurite, Adjusting Eu2+ and Eu3+ Emissions toward White Light Emission," Materials, vol. 12, no. 24, p. 4140, 2019.
35. N. Elkhoshkhany, S. Y. Marzouk, and S. Shahin, "Synthesis and optical properties of new fluoro-tellurite glass within (TeO2-ZnO-LiF-Nb2O5-NaF) system," J Non Cryst Solids, vol. 472, pp. 39–45, 2017.
36. Y. B. Saddeek, K. A. Aly, K. S. Shaaban, A. M. Ali, M. M. Alqhtani, A.

M. Alshehri, M. A. Sayed, E. A. Wahab EA, “Physical properties of B2O3–TeO2–Bi2O3 glass system,” J Non Cryst Solids, vol. 498, pp. 82–88, 2018.

Optimizing Titanium Dioxide (TiO_2) Nanostructured via Precursor Conditions for Enhanced Photocatalytic Degradation of β_2-Microglobulin

Nahrusyifa' Abdul **Karim**, Jumril **Yunas***, Azrul Azlan **Hamzah**
Institute of Microengineering and Nanoelectronics, Universiti Kebangsaan Malaysia, Bangi 43600, Selangor, Malaysia
Correspondence: jumrilyunas@ukm.edu.my

Received: 11 September 2025; 8 October 2025

ABSTRACT

Titanium dioxide (TiO_2) nanostructures have been synthesized via hydrothermal method under varying precursor conditions. The objective of this study was to investigate the effect of pH and ethanol on their structure and photocatalytic activity that capable to reduce the concentration of organic materials such β_2-Microglobulin (β_2M). The EDX analysis confirmed anatase phase, where acidic conditions produced smaller, defect-rich crystallites, while alkaline conditions favored higher crystallinity. FESEM analysis showed that ethanol reduced aggregation and improved surface uniformity compared to samples prepared without ethanol. Photocatalytic tests using methylene blue revealed higher degradation efficiency for TiO_2 synthesized under acidic conditions, attributed to enhanced defects and surface area that promote reactive oxygen species (ROS) generation. These results demonstrate that precursor condition directly influenced the photocatalytic efficiency of TiO_2 nanostructured and highlight the potential for degrading others complex organic biomolecules such as β_2-Microglobulin in biomedical field.

Keywords: Titanium dioxide (TiO_2), hydrothermal synthesis, photocatalysis, artificial kidney, β2-microglobulin (β_2M)

1.0 INTRODUCTION

Photocatalysis is a advance oxidation process that utilized light energy absorption to drive redox reactions capable of degrading a wide range of biological and organic pollutants (1). Semiconductor materials such as TiO_2, ZnO, and WO_3 are frequently explored as photocatalysts due to their suitable band gaps and ability to harness ultraviolet or visible radiation (2–4). Among these, TiO_2 stands out because of its strong photoactivity, low cost, non-toxicity, and excellent chemical stability (5). Upon exposed irradiation, TiO_2 generates electron-hole pairs with strong oxidative and reductive potentials which trigger the formation of reactive oxygen species (ROS) that responsible for breaking down organic molecules (6). These features have enhanced the usage of TiO_2 as photocatalysts in environmentals purification systems.

Beyond environmenal applications, TiO_2 is also gaining recognition for biomedical fields particularly in hemodialysis, where the accumulation of β_2-microglobulin (β_2M) protein remains a critical challenge (7). The photocatalytic properties of TiO_2 offer a promising pathway for protein decomposition due to its ability to generate highly reactive surface radicals under light exposure. Among the polymorphys of TiO_2, anatase phase is generally considered with a higher photocatalytic activity, owing to its larger surface area, lower charge recombination, and higher reactivity compared with rutile or brookite (8). Thus careful control of synthesis parameters is essential to tailor the crystal phase, morphology and defect density for specific applications.

Since the physiochemical properties of TiO_2 particles are strongly influenced by precursor composition and synthesis

conditions. In this study, TiO_2 nanostructured were synthesized via a hydrothermal method under varied precursor conditions, including adjustment in pH and ethanol as co-solvent to investigated their structural and optical features. Their photocatalytic activity was then systematically evaluated using methylene blue as model pollutants under simulated UV-visible light. This comparative analysis provides valuable insight into how synthesis conditions modulated surface charge and selectivity in photocatalytic degradation, forming the basis for optimizing TiO_2 nanostructured towards future biomedical applications, particularly the photocatalytic degradation of B2M.

2.0 MATERIALS

Titanium (IV) isopropoxide (TTIP, 97% Sigma Aldrich) was used as the titanium precursor. Ethanol (C_2H_5OH, 96%), hydrochloric acid (HCl), sodium hydroxide (NaOH), methylene blue ($C_{16}H_{18}ClN_3S$), were purchased from Chemiz (Malaysia). All reagents were analytical grade.

3.0 EXPERIMENTAL

3.1 Preparation of Precursor Solution

TiO_2 nanostructured were synthesized by a hydrothermal method with controlled precursor conditions (9). 2 mL of TTIP was added dropwise into 50 mL of dionized water (DI) under vigorous stirrring. For selected samples, ethanol was introduced as a co-solvent (DI:ethanol = 5:1). The pH of the precursor solution was adjusted to either acidic using HCl (pH ≈ 2) or alkaline using NaOH (pH ≈ 10), while the neutral precursor without ethanol served as a baseline. The prepared precusor were then heated at 180°C for 24 h. The synthesis TiO_2 nanostructured were then washed seveal times with DI water and ethanol. Lastly samples were annealed at 400°C for 5 h to improve crsytallinity.

3.2 Characterization process

The synthesized TiO_2 will be characterized using multiple analytical techniques to evaluate their structural, morphological, optical, and surface properties. Field Emission Scanning Electron Microscopy (FESEM-EDX) will be used to examine surface morphology, and elemental composition. X-Ray Diffraction (XRD) analysis will confirm the crystallographic phase, crystallite size was estimated using the Scherrer equation, while dislocation density and specific surface area (SSA) were calculated from peak broadening parameters.

3.3 Photocatalytic Activity Test With Methylne Blue

Photocatalytic performance was first evaluated using methylene blue (MB) as a reference sample. For each test, 100 mg of TiO_2 particles were dispersed in 100 mL MB solution and sonicated for 20 mins (10). Photocatalytic degradation was carried out under UV light irradiation, and 3 mL of solutions were withdrawn at 30 mins interval up to 120 mins. The catalyst was separated by centrifugation, and the absorbance of the supernatant was measured at 664 nm using a UV–Vis spectrophotometer. The photodegradation efficiency of TiO_2 particles was calculated using the following equation (11);

$$Dye\ removal\ (\%) = \frac{C_0 - C_t}{C_0} \times 100\%$$

Where C_t is the concentration of MB at time (t) and C_0 is the initial concentration of MB.

4.0 RESULTS AND DISCUSSION

4.1 XRD Analysis

The XRD analysis revealed that all TiO_2 nanostructured samples crystallized into the anatase phase (PDF 01-076-8999). The diffraction angle (2Θ) at 25.95°, 36.75°, 37.05°, 37.91°, 48.07°, 52.27°, 54.54°, 62.78°, 63.05° which corresponds

to the Braggs reflection plane of (110), (101), (111), (210), (211), (220), (002), and (301) respectively. The observed angle at 25.95° (101) represents the high crystalline nature of TiO_2 (Fig. 1). The absence of rutile or brookite peaks confirmed that the hydrothemal method succefully produced phase pure anatase nanostructures under different synthesis paramaters. The average crystalline size of TiO2 particles was calculated from the XRD pattern using the Debye Scherrer formula (12);

$$D = \frac{K\lambda}{\beta \cos\theta}$$

Where D is an average crystalline size, K is a dimension less shape factor with a value close to unity, λ is the wavelength of the X-ray, β is the full width half the maximum intensity (FWMH) and θ is the Bragg angle.

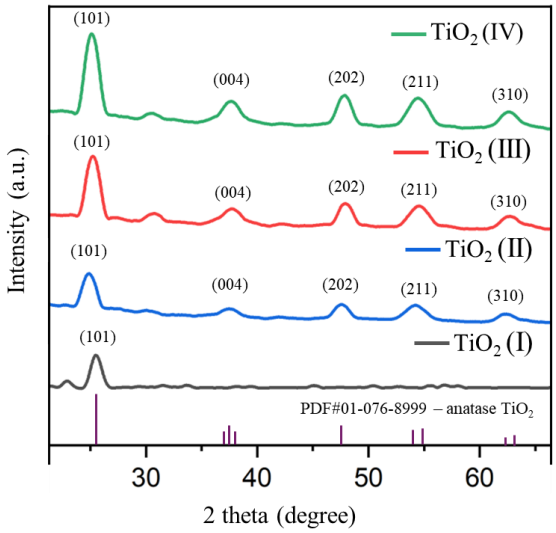

Fig. 1: XRD patterns for different TiO_2 preparation process, (I) alkaline, (II) acidic, (III) without ethanol and (IV) ethanol. The PDF #01-076-8999 for TiO_2 is shown as a reference. The insets are Miller indices of anatase phases

Clear distinctions were observed when comparing the effect of pH and the presence of ethanol on the structural properties. TiO_2 (I) with addition of NaOH exhibits a sharper and more intense (101) diffraction peak, indicating higher crystallinity and larger crystallite domains. In contrast, TiO_2 (II) with the addition of HCl showed broader peaks shifted slightly towards lower angles, reflecting smaller crystallite sizes and lattice strain, possible associated with oxygen vacancy formation (13–15). The scherrer equation confirmed this trend with crystallite sizes of 7.9 nm for TiO_2 (I) with alteration of alkaline and 6.4 nm for TiO_2 (II) that alter with HCl. These results highlight that precursor pH strongly influences crystallinity where alkaline conditions favor crystal growth, whereas acidic conditions suppress growth and introduce structural defects (16). For a second contrast emerged between sample prepared with and without the presence of ethanol. TiO_2 (IV) with ethanol shows a broader diffraction peaks compared without the presence of ethanol, TiO_2 (III). This suggesting that ethanol slowed the hydrolysis rate of TTIP leading to finer crystallite with high defect density (15,17). Thus, ethanol appears to acts as a growth modifiying agent, controlling nucleation dynamics and defect formation. Overall, the XRD analysis demonstrates that both pH and ethanol addition critically tune the crystallinity, crystallite size, and defect density of TiO_2 particles.

4.2 FESEM analysis

Figure 2 shows the FESEM images of TiO_2 nanostructured prepared under different precursor conditions. The images clearly demonstrate the influence of ethanol on the surface morphology and particle dispersion of the resulting TiO_2 particles. This revealed that the preparation of TiO_2 nanostructured with the presence of ethanol was distributed with lower aggregation between particles (10). Most particles appeared in a nanosized spherical form with a relatively smooth surface arrangement. The reduced clustering is attributed to the role of ethanol as a co-solvent, which slows down the hydrolysis process and thereby promotes more controlled nucleation. This effect results in better dispersion and stabilization of the nanoparticles.

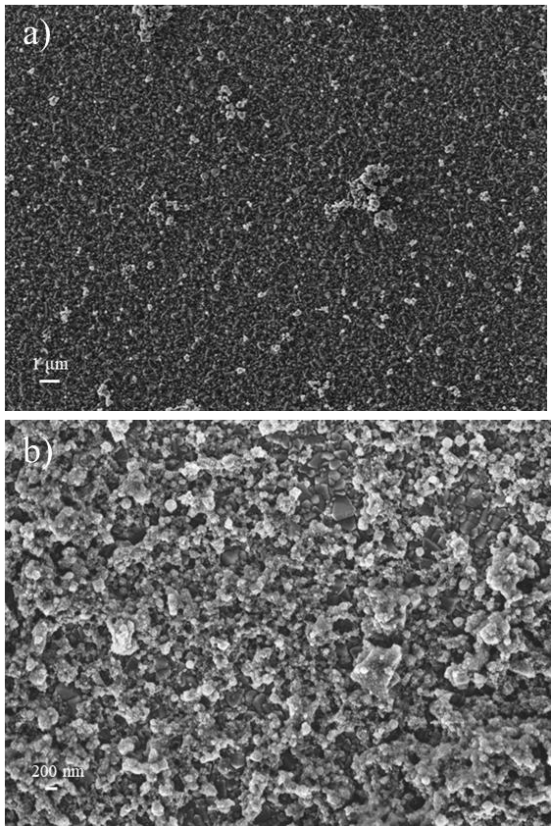

Fig. 2: Shows FESEM images of TiO_2 particles at different preparation process a) TiO_2 with the presence of ethanol b) TiO_2 without ethanol.

On the other hand, figure 2 shows a highly agglomerated particles structure from TiO_2 without the presence of ethanol where individual particles coalesced into irregular crumble clusters. The absence of ethanol allowed rapid hydrolysis during synthesis process producing uncontrolled nucleation followed by significant particles growth and aggregation. This has led to a reduction in the effective area and may limit the accessibility of reactive sites for photocatalytic reactions (18,19). Hence, FESEM analysis confirms that ethanol plays critical role in regulating particles growth and agglomeration.

4.3 Elemental Composition

The elemental analysis of the chemical compounds was investigated through EDX analysis. Figure 3 shows the elemental composition of TiO_2 nanoparticles. The elements present in the synthesized TiO_2 are Titanium (Ti) and Oxygen (O). The result shows the composition of the O element is higher compared to Ti content. The atomic and weight percentage of the TiO_2 are tabulated in Table 1.

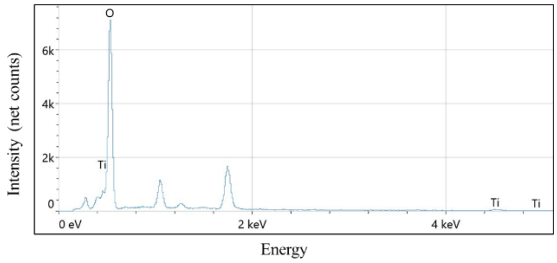

Fig. 3: EDX analysis of TiO_2 preparation with ethanol

TABLE I: Elemental composition of TiO_2 with ethanol

No.	Element	Wt (%)
1	Oxygen (O)	92.7
2	Titanium (Ti)	7.3

4.4 Photocatalytic activity

The photocatalytic degradation of MB dye was investigated under UV-Vis to assess the efficiency of TiO_2 prepared under different precursor conditions. MB was selected as a reference sample to study the photocatalytic activity due to its strong absorption peak at 665 nm, which corresponds to π-π* electronic transition of its chromophoric group, making its degradation pathway straightforward to monitor (10). A decrease in the absorbance intensity over irradiation time indicated a progressive breakdown of MB molecules.

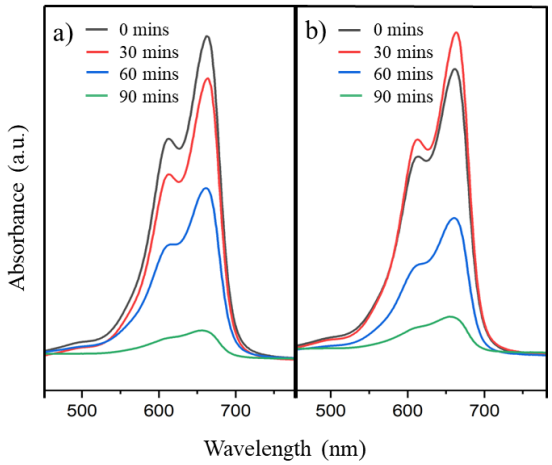

Fig. 4: Photocatalytic activity of TiO2 a) acidic b) alkaline

Figure 4 shows that TiO_2 synthesized under acidic conditions demonstrated a higher degradation rate of MB with 90% removal compared to the sample prepared under alkaline conditions. This enhancement can be attributed to several structural and surface property differences. Since acidic prepared TiO_2 exhibits a smaller crystallite size and broader peak from XRD analysis, indicating a higher density of lattice defects and oxygen vacancies. This has contributed to a larger specific surface area with higher absorption capacity which in turn facilitates more efficient generation of ROS groups. As a result, acidic prepared TiO_2 demonstrates superior degradation of MB compared with alkaline prepared TiO_2 (9,20), despite the latter showing higher crystallinity. This suggests that adsorption on the catalyst surface and production of ROS is better over bulk crystallinity in determining photocatalytic efficiency. Given β_2M degradation similarly depends on adsorption and oxidative fragmentation at the catalyst surface and defect-rich, TiO_2 prepared in acidic conditions is expected to provide a more favorable pathway for protein decomposition compared to alkaline condition of precursor solution.

4.5 Optimizing TiO_2 for β_2M Decomposition

Result obtained from this study shows that precursor pH and the presence of ethanol strongly influence the structural features and photocatalytic behavior of TiO_2 photocatalytic activity. Under alkaline conditions, higher crystallinity that favors charge separation and sustained ROS generation, yet the lower density of surface defects may reduce adsorption affinity towards large biomolecules such as β_2M (21,22). In contrast, acidic synthesis produced smaller crystallites with high defect density and surface area has higher adsorption capacity and reactivity despite some agglomeration.

Similarly, the presence of ethanol during preparation process displayed lower aggregation and greater exposure of active sites compared to those prepared without ethanol, offering more effective interaction with β_2M molecules. These findings suggest that while crystallinity promotes charge transport, surface defect and dispersion are equally critical for enabling oxidative protein decomposition. Thus, controlled tuning of pH and solvent environment provides a pathway to optimize TiO_2 nanostructures for efficient β_2M decomposition.

5.0 CONCLUSION

TiO_2 nanostructures were synthesized via a hydrothermal method with varying pH and ethanol conditions, yielding anatase phase with distinct crystallinity, crystallite size, and defect densities. Acidic synthesis produced smaller, defect-rich crystallites with higher photocatalytic activity, while ethanol addition reduced agglomeration and improved surface exposure. These structural features directly enhanced methylene blue degradation, suggesting their suitability for the decomposition of complex biomolecules such as β_2M. The results highlight precursor condition as a key factor in tailoring TiO_2 for biomedical photocatalysis.

ACKNOWLEDGEMENTS

The authors gratefully acknowledge financial support from Ministry of Higher Education under the Project TRANSLATIONAL-2023-002 and HiCoE IMEN AKU 254.

REFERENCES

1. Shuang S, Zhang Z. The effect of annealing treatment and atom layer deposition to Au/Pt nanoparticles-decorated TiO2 nanorods as photocatalysts. Molecules. 2018;23(3).
2. Khan H, Pawar RC, Charles H, Sunyong Lee C. Cu-doped TiO2

nanofibers coated with 1T MoSe2 nanosheets providing a conductive pathway for the electron separation in CO2 photoreduction. Appl Surf Sci. 2023;636:157832.
3. Aspoukeh PK, Barzinjy AA, Hamad SM. Synthesis, properties and uses of ZnO nanorods: a mini review. Int Nano Lett. 2022;12(2):153–68.
4. Mohd Raub AA, Rahim MHD, Bahru R, Latif R, Hamzah AA, Simarani K, and Yunas J, A review on zinc oxide nanostructures as antimicrobial agent: mechanism and applications, Nanotechnology 2025, 36: 292001.
5. Suhaimi NHS, Azhar R, Adzis NS, Mohd Ishak MA, Ramli MZ, Hamzah MY, et al. Recent updates on TiO2-based materials for various photocatalytic applications in environmental remediation and energy production. Desalin Water Treat. 2025;321:100976.
6. Ge J, Zhang Z, Ouyang Z, Shang M, Liu P, Li H, et al. Photocatalytic degradation of (micro)plastics using TiO2-based and other catalysts: Properties, influencing factor, and mechanism. Environ Res. 2022;209:112729.
7. Tang H. Nanostructured Photocatalytic Systems to Enable Portable Kidney Dialysis and Precision Synthesis. University of Washington; 2023.
8. Yalcin M. The effect of pH on the physical and structural properties of TiO2 nanoparticles. J Cryst Growth. 2022;585:126603.
9. Santhi K, Navaneethan M, Harish S, Ponnusamy S, Muthamizhchelvan C. Synthesis and characterization of TiO2 nanorods by hydrothermal method with different pH conditions and their photocatalytic activity. Appl Surf Sci. 2020;500:144058.
10. Aravind M, Amalanathan M, Mary MSM. Synthesis of TiO2 nanoparticles by chemical and green synthesis methods and their multifaceted properties. SN Appl Sci. 2021;3(4):1–10.
11. Singh S, Sidhu GK, Singh H. Removal of methylene blue dye using activated carbon prepared from biowaste precursor. Indian Chem Eng. 2019;61(1):28–39.
12. Moradnia F, Taghavi Fardood S, Ramazani A, Gupta VK. Green synthesis of recyclable MgFeCrO4 spinel nanoparticles for rapid photodegradation of direct black 122 dye. J Photochem Photobiol A Chem. 2020;392:112433.
13. Sahadat Hossain M, Ahmed S. Easy and green synthesis of TiO2 (Anatase and Rutile): Estimation of crystallite size using Scherrer equation, Williamson-Hall plot, Monshi-Scherrer Model, size-strain plot, Halder- Wagner Model. Results Mater. 2023;20:100492.
14. Kamisaka H, Hitosugi T, Suenaga T, Hasegawa T, Yamashita K. Density functional theory based first-principle calculation of Nb-doped anatase TiO2 and its interactions with oxygen vacancies and interstitial oxygen. J Chem Phys. 2009;131(3).
15. Ahmed S, Shishir MKH, Islam MT, Rahaman MA, Aman S, Aidid AR, et al. Crystallinity integration of anatase (TiO2) nanocrystal by whole powder pattern fitting (WPPF) method: A Rietveld refinement study. Results Mater. 2025;26:100673.
16. Mohammadi MR, Fray DJ, Mohammadi A. Sol-gel nanostructured titanium dioxide: Controlling the crystal structure, crystallite size, phase transformation, packing and ordering. Microporous Mesoporous Mater. 2008;112(1–3):392–402.
17. Qaid SMH, Ghaithan HM, Bawazir HS, Bin Ajaj AF, AlHarbi KK, Aldwayyan AS. Successful Growth of TiO2 Nanocrystals with {001} Facets for Solar Cells. Nanomaterials. 2023;13(5):1–17.
18. Ananthakumar S, Kumar JR, Babu SM. Colloidal synthesis and

characterisation of oleic acid capped TiO2 nanorods. Int J Nanotechnol. 2017;14(9–11):710–8.
19. Gupta T, Samriti, Cho J, Prakash J. Hydrothermal synthesis of TiO2 nanorods: formation chemistry, growth mechanism, and tailoring of surface properties for photocatalytic activities. Mater Today Chem. 2021;20.
20. Jiang Y, Yang F, Hassan Kazmi SSU, Zhao Y, Chen M, Wang J. A review of microplastic pollution in seawater, sediments and organisms of the Chinese coastal and marginal seas. Chemosphere. 2022;286(P1):131677.
21. Yoo H, Bae C, Yang Y, Lee S, Kim M, Kim H, et al. Spatial charge separation in asymmetric structure of Au nanoparticle on TiO2 nanotube by light-induced surface potential imaging. Nano Lett. 2014;14(8):4413–7.
22. Noh J, Kwon SH, Park S, Kim KK, Yoon YJ. TiO2 nanorods and pt nanoparticles under a uv-led for an no2 gas sensor at room temperature. Sensors. 2021;21(5):1–11.

Structural, Magnetic, and Dielectric Properties of Y^3-substituted $BiFeO_3$ Multiferroic Ceramics

Ammar Abd Ali **Najm**[1], Raba'ah Syahidah **Azis**[1,2], Abdul Halim **Shaari**[1], Chan Kar Tim[1], Nurul Huda **Osman**[1], Ehssan **Al-Bermany**[3]

[1]*Department of Physics, Faculty of Science, Universiti Putra Malaysia, 43400 UPM Serdang, Selangor, Malaysia.*

[2]*Nanomaterials Synthesis and Characterization Laboratory (NSCL), Institute of Nanoscience and Nanotechnology (ION2), Universiti Putra Malaysia, 43400 Serdang, Selangor, Malaysia*

[3]*Department of Physics, College of Education for Pure Science, University of Babylon, Hillah, Iraq*

Corresponding author: rabaah@upm.edu.my*, ammaralin79@gmail.com

Received: 21 September 2025; Accepted: 4 December 2025

ABSTRACT

In this study, the Y3+-substituted Bismuth ferrite ($BiFeO_3$, BFO) multiferroic ceramics, BiFe1-xYxO_3 ceramics (x = 0.0-0.4), were synthesized using the solid-state reaction method to evaluate the effect of Y substitution on the structural, magnetic, and dielectric behavior. X-ray diffraction confirmed a reduction in unit cell volume from 373.7 Å³ (x = 0.0) to 370.7 Å³ (x = 0.2) due to the smaller ionic radius of Y, followed by a rhombohedral (R3c) to orthorhombic (Pnma) phase transition at x ≥ 0.3, with unit cell volume decreasing to 229.2 Å³ (x = 0.4). SEM revealed progressive grain refinement, consistent with suppressed leakage current. Magnetic measurements showed the highest saturation magnetization (2.90 emu/g) at x = 0.2, while further substitution reduced the coercivity, indicating a soft magnetic behavior advantageous for permeability. Dielectric studies revealed a strong frequency dependence of permittivity, attributed to Maxwell-Wagner polarization and polaron hopping. The AC conductivity (σac) decreased from 5.19 × 10-8 S/cm (x = 0.0) to 7.75 × 10-12 S/cm (x = 0.4), while the quality factor (Q) improved significantly from 0.284 to 7462.7. Notably, the x = 0.2-0.3 compositions exhibited the best balance of permittivity and permeability, providing favorable impedance matching with free space. These findings highlight Y-substituted BFO as a promising candidate for advanced microwave device absorbers and EMI shielding applications.

Keywords: $BiFeO_3$; multiferroic; yttrium substitution; dielectric properties;

1. INTRODUCTION

Multiferroic materials, which possess a simultaneous consideration of ferroelectric and antiferromagnetic characteristics at room temperature, have attracted significant attention for next-generation multifunctional technologies [1]. Even though various multiferroic materials, while bismuth ferrite ($BiFeO_3$, BFO) is one of the most investigated room temperature multiferroics, due to its high Curie temperature (T_C) 1083 K, and Néel temperature (T_N) 643 K [2]. The characteristics of BFO render it highly desirable for microwave absorption applications, electromagnetic interference (EMI) shielding, spintronic devices, and energy storage systems [3].

The practical application of pure BFO is restricted by inherent limitations, such as weak magnetization resulting from spin cycloidal modulation, high leakage current

due to significant dielectric loss, and oxygen vacancies [4]. These defects limit its effectiveness as an electromagnetic (EM) absorber and restrict its integration into modern shielding architectures [5]. Several modification strategies have been investigated to mitigate these issues, including reduction of particle size, optimization of the synthesis method, and elemental substitution at the A- or B-site of the perovskite structure [6].

Specifically, substitution of rare earth (RE) ions at the Bi^{3+} site has revealed the efficient reduction of leakage current, stabilization of crystal structure, and enhancement of magnetic and dielectric performance [7-12]. Such doping interrupts the long-range cycloidal spin structure, thereby increasing magnetization, while inducing lattice distortion that tunes the dielectric properties [13]. Previous studies on RE-doped BFO, including Sm^{3+}, Gd^{3+}, Nd^{3+}, and Dy^{3+} substitutions, have confirmed enhancements in the multiferroic properties and behavior of microwave absorption [14-17]. Though, most of these findings have focused on A-site substitution, whereas B-site doping with Y^{3+} remains largely untapped. Yttrium has a comparable ionic radius to Fe^{3+} in octahedral coordination [18]. It displays strong chemical stability, making it an effective dopant for stabilizing the perovskite lattice and decreasing oxygen-vacancy-related leakage [16]. On the contrary, A-site RE substitution, which primarily affects ferroelectric distortion, B-site Y^{3+} combination straight modifies the Fe-O-Fe super exchange network, potentially improving spin canting and dielectric polarization through controlled lattice distortion[19]. This unique substitution strategy thus allows for simultaneous tuning of magnetic and dielectric properties, providing a more efficient method for enhancing microwave absorption performance.

This study concentrates on the synthesis of $BiFe_{1-x}Y_xO_3$ (x = 0.0-0.4) ceramics through a conventional solid-state reaction to observe the impact of Y^{3+} substitution on the structural, dielectric, and magnetic properties of BFO. The relationship between phase evolution, microstructural modifications, and magnetic response was carefully analyzed to determine the optimal composition for microwave absorption and EMI shielding applications.

2. MATERIALS

The high purity oxide powders were utilized as precursors: bismuth oxide, Bi_2O_3 (99.9%), iron(III) oxide, Fe_2O_3 (99.98%), and yttrium oxide, Y_2O_3 (99.99%). Polyvinyl alcohol (PVA; 0.05 mL g^{-1}) was used as a temporary binder during the pelletization process. To study the electrical properties, the polished surface of the pellets was coated with silver.

2.1 EXPERIMENTAL METHODS

2.1.1 Synthesis

$BiFe_{1-x}Y_xO_3$ (x = 0.0, 0.1, 0.2, 0.3, 0.4) ceramics were synthesized via a conventional solid-state reaction method. The stoichiometric amounts of Bi_2O_3, Fe_2O_3, and Y_2O_3 (analytical grade, ≥99.9% purity) were accurately weighed, carefully mixed, and ground in an agate mortar to ensure chemical homogeneity. The resulting powder mixture was calcined at 780 ºC for 2 hours to initiate solid state diffusion and enhance the formation of the perovskite phase. After calcination, the powder was further ground for 1 hour to achieve a uniform fine particle size.

The cylindrical pellets of 13 mm diameter, 2 mm thickness were produced via polyvinyl alcohol (PVA; 0.05 mL g^{-1}) as a temporary binder and compressed under a uniaxial pressure of 5 tons. The pellets were consecutively sintered in air at 800 ºC for 3 hours, temperature selected based on previous studies indicating ideal densification and phase purity of BFO ceramics achieved in the 780 to 820 ºC range [20, 21]. Reducing this range, incomplete crystallization, and residual

Bi_2O_3 phases were determined in preliminary trials. Higher temperatures (>830 ºC) resulted in partial Bi volatilization and the appearance of secondary phases, such as $Bi_{25}FeO_{40}$. Hence, 800 ºC was determined as the optimum sintering temperature, confirming a balance between phase purity, grain growth control, and mechanical integrity [22].

2.1.2 Structural and microstructural analysis.

Phase composition was examined by X-ray diffraction (XRD; Philips X'Pert, model 7602 EA Almelo) using Cu Kα radiation (λ = 1.5418 Å) over 2θ = 20º-80º. Surface morphology and grain features were observed by scanning electron microscopy (SEM; JEOL JSM-6400).

2.2 Electrical measurements

Both pellet faces were polished and coated with silver paste to form electrodes. Room-temperature dielectric spectra were collected with an Agilent 4294A Precision Impedance Analyzer from 40 Hz to 10 MHz.

2.3 Magnetic measurements.

Magnetization hysteresis (M-H) loops were recorded at room temperature utilizing a LakeShore 7407 vibrating sample magnetometer (VSM).

3.1 Crystal structure and phase evolution (XRD)

The XRD pattern (Figure 1) indicates that $BiFeO_3$ ceramics sintered at 800 ºC are single phase, matching the standard data (ICSD collection code 8823)[13]. The data were analyzed by Rietveld refinement using X'Pert HighScore Plus. All peaks were indexed to the rhombohedral perovskite structure, space group R3c, with no secondary phases detected. In Figure 1, the XRD patterns of $BiFe_{1-x}Y_xO_3$ ($x = 0$, 0.1, 0.2, 0.3, 0.4) are shown. With increasing Y^{3+} substitution at the B-site (Fe site), the $BiFeO_3$ reflections decrease in intensity, and additional peaks due to $Bi_{25}FeO_{40}$, $BiYO_3$, $YFeO_3$, and residual Y_2O_3 appear[23]. Because Y^{3+} is substantially larger than Fe^{3+} in octahedral coordination (Y^{3+} = 0.90 Å vs Fe^{3+} = 0.645 Å), extensive B-site incorporation is difficult, which explains the emergence of these secondary phases[24].

Rietveld analysis (Table 1) shows that the $BiFeO_3$ phase with rhombohedral R3c symmetry dominates for $x \leq 0.2$, with a gradual decrease of the lattice parameters and unit-cell volume (373.7 Å³ to 370.7 Å³) as Y content increases. For $x \geq 0.3$, additional reflections become prominent, and the diffraction is governed by the orthorhombic Pnma structure of $YFeO_3$, consistent with literature reports that Y substitution beyond 0.2 promotes multiphase formation, depending on the processing conditions [25]. The phase evolution therefore proceeds from single-phase R3c (x = 0.0-0.2) to mixtures in which Y-rich orthorhombic ferrite ($YFeO_3$) becomes dominant (x = 0.3-0.4). The initial lattice contraction up to x = 0.20 is attributed to limited B-site (Fe-site) Y^{3+} incorporation accompanied by microstrain. In contrast, higher nominal Y contents primarily yield Y-rich orthorhombic phases rather than further substitution into the $BiFeO_3$ lattice[26].

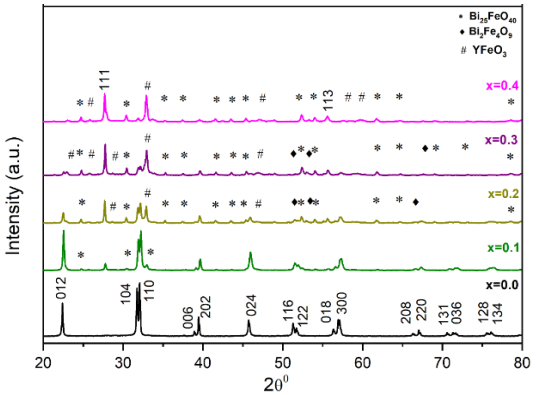

Fig. 1: XRD patterns of $BiFe_{1-x}Y_xO_3$ ceramics (x = 0.0-0.4) sintered at 800 ºC.

Table 1: Lattice parameters of $BiFe_{1-x}Y_xO_3$ ceramics (x = 0.0-0.4) as a function of composition

Y contents (x)	Phases & percentage (%)	Space group	Lattice parameters			Crystal system	V(Å^3)
			a (Å)	b(Å)	c (Å)		
0	$BiFeO_3$ 100%	R3c 161	5.578	5.578	13.870	rhombohedral	373.724
0.1	$BiFeO_3$ 85.8%	R3c 161	5.568	5.568	13.830	rhombohedral	371.419
0.2	$BiFeO_3$ 35.6%	R3c 161	5.566	5.566	13.820	rhombohedral	370.709
0.3	$YFeO_3$ 50.7%	P n m a 62	5.627	7.724	5.363	Orthorhombic	233.094
0.4	$YFeO_3$ 48.9%	P n m a 62	5.614	7.668	5.323	Orthorhombic	229.170

3.2 Microstructure analysis

Representative SEM micrographs of $BiFe_{1-x}Y_xO_3$ (x = 0.0-0.4) are shown in Figure 2. The undoped ceramic (x = 0) displays relatively large, equiaxed grains with rounded edges, indicating significant grain growth during sintering. When Y^{3+} is introduced (x = 0.1), the microstructure becomes more fragmented and faceted, indicating inhibition of grain coarsening. Further substitution (x = 0.2-0.3) produces a pronounced refinement of the microstructure: grains are smaller, more angular, and the intergranular porosity is reduced relative to the undoped sample. Analysis using quantitative means was achieved by measuring the equivalent diameter circle of at least 30 grains per composition via Image-J, average values are presented in Table 2 and displayed in Figure 2, demonstrating a decrease in grain size with increasing Y concentration.

At higher substitution (x = 0.4), the surface appears more compact and densely packed with fine particles. Local regions show a "melted-like" texture with nanometric debris, which may arise from (i) the formation of a Bi-rich transient liquid phase during sintering and/or (ii) the presence of Y-containing secondary phases pinning grain boundaries (solute-drag/Zener pinning), both of which suppress grain growth [27, 28]. The concomitant grain-size reduction and improved packing density at x = 0.40 are consistent with the densification trend inferred from the dielectric data (higher ε′ and lower tan δ at low frequency). In summary, a comparison of the micrographs for all compositions shows that Y^{3+} substitution effectively restrains abnormal grain growth, resulting in finer and more uniform microstructures. This aligns with previous findings on $BiFeO_3$ doping [29-31].

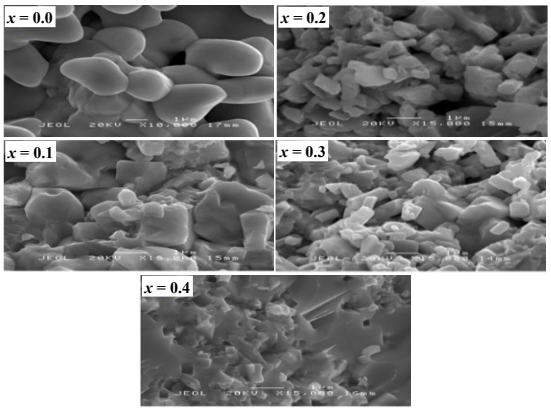

Fig. 2: SEM micrographs of $BiFe_{1-x}Y_xO_3$ ceramics for different substitution levels (x = 0.0-0.4).

Table 2: Average grain size of $BiFe_{1-x}Y_xO_3$ ceramics sintered at 800 °C

x (%)	Average grain size (µm)
0	2.04 ± 0.10
0.1	1.80 ± 0.20
0.2	0.54 ± 0.03
0.3	0.53 ± 0.05
0.4	0.45 ± 0.05

3.3 Dielectric Properties

Figure 3 presents the room-temperature frequency dependence of the real permittivity (ε'_r) for $BiFe_{1-x}Y_xO_3$ (x = 0.0-0.4) measured from 40 Hz to 10 MHz. For all compositions, ε'_r is high at low frequency (40 Hz-1 kHz) and decreases with increasing frequency, approaching a nearly constant value above 10 kHz [32]. This dispersion is characteristic of heterogeneous ferrites and is attributed to Maxwell-Wagner interfacial polarization and space-charge accumulation at grain boundaries and electrode interfaces, together with ionic/dipolar/electronic contributions. [33]. Among the series,x = 0.4 shows the largest ε'_r; at 1kHz, it increases from 26.5 (x = 0.0) to 104 (x = 0.4), consistent with the higher relative density observed by SEM. The intermediate values for x = 0.1 (26.2) and x = 0.2 (20.0) agree with prior reports for Y^{3+}-substituted $BiFeO_3$[18].

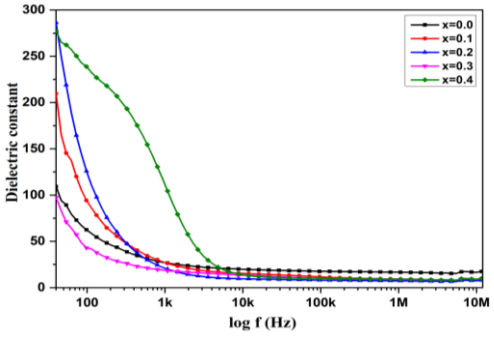

Fig. 3: Relative dielectric permittivity (ε'_r) versus frequency for $BiFe_{1-x}Y_xO_3$ ceramics (x = 0.0-0.4) at room temperature

Figure 4 shows the frequency dependence of the dielectric loss tangent (tan δ). For all compositions, tan δ decreases with frequency, consistent with space-charge relaxation: mobile charges can follow the field at low frequency but lag and relax at higher frequency. The undoped ceramic exhibits the most significant loss, attributable to oxygen-vacancy-assisted conduction, whereas Y^{3+} substitution progressively suppresses loss; at x = 0.4, $\tan\delta = 1.34 \times 10^{-4}$ at 1 kHz. A distinct high-frequency relaxation in x = 0.4 (inset, Fig. 4) is compatible with localized transport (e.g., polaron hopping), as reported for perovskites and ferrites (e.g., donor-doped $BaTiO_3$) [34]. These features indicate multiple relaxation channels involving grains, grain boundaries, and microstructural inhomogeneity; oxygen vacancies can also trap carriers and generate localized relaxation centers.

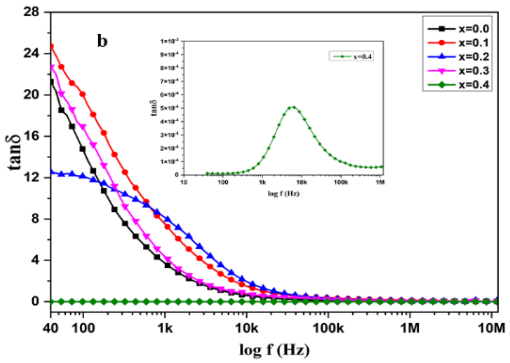

Fig. 4: Loss tangent (tanδ) versus frequency for $BiFe_{1-x}Y_xO_3$ ceramics (x = 0.0-0.4) at room temperature

At 1 kHz (Table 3), AC conductivity (σ_{ac}) which represents the alternating current conductivity initially increases modestly from 5.19×10^{-8} S.cm^{-1} (x = 0.0) to 9.63×10^{-8} S.cm^{-1} (x = 0.3), consistent with defect-mediated hopping, then drops sharply to 7.75×10^{-12} S cm^{-1} at x = 0.4, reflecting suppressed leakage due to reduced oxygen-vacancy conduction and the stabilization of insulating Y-rich secondary phases such as $YFeO_3$/$BiYO_3$. The quality factor improves concomitantly from 0.284 to 7462.7, evidencing low dielectric loss and efficient

energy storage. The combination of high ε'_r, ultralow σ_{ac}, and large Q at $x = 0.4$ favors impedance matching and is advantageous for microwave absorption and EMI-shielding applications.

Table 3: Dielectric parameters (ε'_r, tan δ, σ_{ac}, Q) at 1 kHz for $BiFe_{1-x}Y_xO_3$ ceramics (x = 0.0-0.4)

x	ε'_r	tanδ	σ_{ac} (S/cm)	Q
0.0	26.5	35.20×10^{-1}	5.19×10^{-8}	0.284
0.1	26.2	72.00×10^{-1}	1.05×10^{-7}	0.139
0.2	20.0	79.30×10^{-1}	8.82×10^{-8}	0.126
0.3	41.9	41.30×10^{-1}	9.63×10^{-8}	0.242
0.4	104.0	1.34×10^{-4}	7.75×10^{-12}	7462.7

3.4 Magnetic properties

Figure 5 shows the magnetization (M-H) hysteresis loops of $BiFe_{1-x}Y_xO_3$ ceramics (x = 0.0-0.4) measured at room temperature. The undoped BFO (x = 0.0) exhibits an almost linear M-H response with a very low saturation magnetization (M_S = 0.035 emu/g), which is characteristic of antiferromagnetic ordering. This non-hysteretic behavior reflects the long-wavelength cycloidal spin modulation in BFO, which averages the weak spin canting to yield nearly zero net magnetization [35]. A significant enhancement in M_S is observed at x = 0.2 (2.90 emu/g), whereas the coercivity H_C (16.40 Oe) remains minor (soft-magnetic character), exceeding earlier reported results[36-38]. This magnetic improvement can be attributed to the suppression of the spiral spin structure and lattice distortion, which enhance the Dzyaloshinskii-Moriya (DM) interaction and promote spin canting [39] At higher Y^{3+} concentrations ($x \geq 0.3$), M_S decreases due to the increased presence of nonmagnetic secondary phases such as $YFeO_3$, $Bi_{25}FeO_{40}$ and reduced long-range spin coherence, as indicated by the XRD/Rietveld phase analysis.

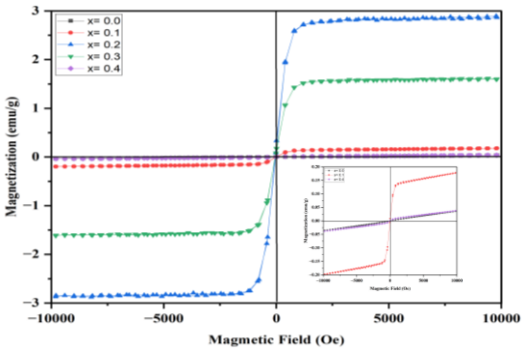

Fig. 5: Magnetization versus magnetic field for $BiFe_{1-x}Y_xO_3$ ceramics (x = 0.0-0.4) at room temperature. Inset: enlarged M-H loops for x = 0.0, 0.1, and 0.4

To measure the magnetic improvement, M_S (emu·g^{-1}) was calculated as the magnetic moment per formula unit (μB f.u.$^{-1}$) via the composition-dependent molar mass and standard cgs-unit conversion. The resulting values, shown in Figure 6, exhibit a maximum μB f.u.$^{-1}$ = 0.166 at x = 0.2, mirroring the M_S trend. The molar mass for each composition was calculated as

$$M_{molar}(x) = M_{Bi} + (1-x)M_{Fe} + xM_Y + 3M_O$$

and μB f.u.$^{-1}$ values were obtained using

$$\mu B \backslash f.u. = \frac{M_s \times M_{molar}(x)}{55385}$$

where 5585 is the standard conversion constant consistent with cgs units and Avogadro's number.

Assuming two antiparallel Fe^{3+} sublattices (m ≈ 5 μB), the canting angle (φ) that produces the measured net moment (m_{net}) was estimated from

$$m_{net} = 2m\sin(\emptyset/2)$$

$$\Rightarrow \emptyset = 2sin^{-1}\left(\frac{m_{net}}{2m}\right)$$

Table 3: Measured and calculated magnetic parameters of $BiFe_{1-x}Y_xO_3$ ceramics (x = 0.0-0.4) at room temperature.

x (Y)	Ms (emu·g^{-1})	Mr (emu·g^{-1})	Hc (Oe)	μB/f.u.	Canting Angle φ (°)
0.0	0.035	5.16×10^{-4}	93.13	0.00196	0.0225
0.1	0.190	6.50×10^{-3}	25.10	0.01076	0.1232
0.2	2.900	9.00×10^{-2}	16.40	0.16587	1.9008
0.3	1.600	4.70×10^{-2}	16.00	0.09246	1.0595
0.4	0.038	9.50×10^{-4}	60.00	0.00222	0.0254

The calculated parameters (Table 3) show the largest μB f.u.$^{-1}$ (0.166) and φ = 1.9° at x = 0.2, consistent with the optimized magnetic response. These results align with previous reports [40], indicating that moderate rare-earth substitution enhances magnetization through distortion-induced spin canting.

Figures **6** and 7 illustrate the variations of μB f.u.$^{-1}$ and φ with Y content. Both parameters peak at x = 0.2 and decline thereafter.

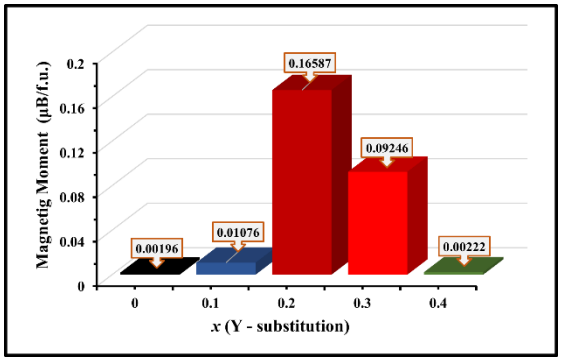

Fig. 6: Magnetic moment per formula unit (μB/f.u.) vs Y content x, derived from M_S

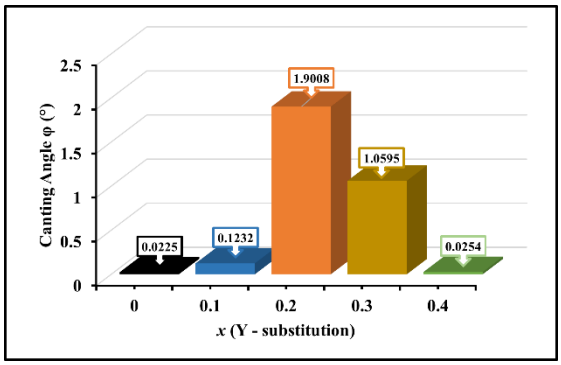

Fig. 7: Canting angle φ vs Y content x, estimated from μB/f.u. using the two-sublattice canting model.

Rietveld analysis reveals that the R3c BFO phase decreases from 100% at x = 0.0 to 36% at x = 0.2, while Y-rich orthorhombic phases become dominant at higher substitution levels. The magnetic enhancement at x = 0.2 is therefore primarily attributed to the intrinsic weak ferromagnetism of the R3c phase, reinforced by DM-interaction-driven canting and microstructural refinement that increases uncompensated boundary spins. The subsequent reduction in M_S, μB f.u.$^{-1}$, and φ for $x \geq 0.3$ correlates with the prevalence of nonmagnetic Y-based phases and diminished spin coherence within the residual BFO matrix[41].

4. CONCLUSION

Yttrium-substituted $BiFe_{1-x}Y_xO_3$ ceramics (x = 0.0-0.4) were synthesized by a solid-state route and show a composition-dependent structure property correlation. Rietveld analysis confirms R3c symmetry up to x = 0.2 and a rhombohedral to orthorhombic (Pnma) transition for $x \geq 0.3$, accompanied by grain refinement. Dielectrically, x = 0.4 delivers the best performance (ε'_r =104, tanδ = 1.34×10^{-4} at 1 kHz, $\sigma_{ac} = 7.75\times10^{-12}$ S cm^{-1}), indicating effective leakage suppression and favorable impedance matching. Magnetically, a maximum M_S = 2.9 emu g^{-1} at x = 0.20 (0.166 μB f.u.$^{-1}$; φ = 1.9°) is consistent with cycloid suppression and DM-induced spin canting, whereas higher Y content reduces M_S due to secondary phases. The key

novelty is the identification of two practical optima within one system, x = 0.2 for magnetic loss and x = 0.40 for low-loss dielectric matching, offering a composition-tunable route to EM absorption/EMI shielding.

The current study is limited by the lack of GHz-range measurements of complex permittivity (ε*(f)) and permeability (μ*(f)), as well as reflection loss (RL) data. Additionally, all measurements were conducted solely at room temperature. Prospective studies should focus on directly evaluating microwave absorption within the 2-18 GHz frequency band, consider the temperature dependent electromagnetic properties, and explore the design of graded or bilayer structures combining compositions around x = 0.2 and x = 0.4 to obtain larger broadband absorption efficiency.

ACKNOWLEDGEMENTS

The authors are grateful to the Department of Physics, Faculty of Science, Universiti Putra Malaysia, for the measurement facilities. Additional gratitude is extended to the Universiti Putra Initiative Grant, Grant No. (GP-IPS/2025/982400) for funding.

REFERENCES

1. N. Kumar, et al., Exploration of Eco-Friendly multifunctional material: Investigating the Structural, Electrical, and multiferroic properties of $Bi(Cd_2/5Ti_2/5Fe1/5)O_3$. Materials Science Engineering: B, 2025. 316: p. 118101.
2. N. Wang, et al., Structure, performance, and application of $BiFeO_3$ nanomaterials. J Nano-micro letters, 2020. 12(1): p. 81.
3. Y.-Q. Kang, et al., Microwave absorption properties of multiferroic $BiFeO_3$ nanoparticles. J Materials Letters, 2009. 63(15): p. 1344-1346.
4. N. Wang, et al., Structure, performance, and application of $BiFeO_3$ nanomaterials. Nano-micro letters, 2020. 12(1): p. 81.
5. K. Cao, et al., Fabrication of 3D micro-flower structured $BiFeO_3$ growing on rGO nanosheets for enhanced electromagnetic wave absorption. Chemical Engineering Journal, 2024. 496: p. 154184.
6. Y. Nassereddine, et al., Recent advances toward enhanced photocatalytic properties of $BiFeO_3$-based materials. Nanomaterials, 2023. 14(1): p. 51.
7. X. Zhang, et al., Effect of Eu substitution on the crystal structure and multiferroic properties of $BiFeO_3$. Journal of alloys compounds, 2010. 507(1): p. 157-161.
8. D. Kan, et al., Universal behavior and electric-field-induced structural transition in rare-earth-substituted $BiFeO_3$. J Advanced Functional Materials, 2010. 20(7): p. 1108-1115.
9. T.D. Rao, T. Karthik, and S. Asthana, Investigation of structural, magnetic and optical properties of rare earth substituted bismuth ferrite. Journal of Rare Earths, 2013. 31(4): p. 370-375.
10. C.-J. Cheng, et al., Microstructure-electromechanical property correlations in rare-earth-substituted $BiFeO_3$ epitaxial thin films at morphotropic phase boundaries. Applied physics letters, 2010. 97(21).
11. B. Xu, et al., Finite-temperature properties of rare-earth-substituted $BiFeO_3$ multiferroic solid solutions. Advanced Functional Materials, 2015. 25(4): p. 552-558.
12. A. Rabadanova, et al., Structure and dielectric properties of $Bi_{1-x}La_xFeO_3$ nanostructured ceramics. Ferroelectrics, 2021. 576(1): p. 1-7.
13. K.L. Da Silva, et al., Suppression of the cycloidal spin arrangement in $BiFeO_3$ caused by the mechanically induced structural distortion and its effect on magnetism. Frontiers in Materials, 2021. 8: p. 717185.
14. T. Wang, et al., Effect of rare-earth Nd/Sm doping on the structural and multiferroic properties of $BiFeO_3$

ceramics prepared by spark plasma sintering. Ceramics International, 2020. 46(10): p. 15228-15235.
15. S. Rani, et al., Structural, dielectric, and magnetic properties of Dy-substituted $BiFeO_3$ multiferroic ceramics. Journal of Materials Science: Materials in Electronics, 2023. 34(4): p. 258.
16. D. Karpinsky, et al., Evolution of the crystal structure and magnetic properties of Sm-doped $BiFeO_3$ ceramics across the phase boundary region. Ceramics International, 2021. 47(4): p. 5399-5406.
17. S. Sharma, A. Kumar, and O. Thakur, Investigations on structural, magnetic, and dielectric properties of Gd-substituted perovskite $BiFeO_3$ multiferroics. Journal of Materials Science: Materials in Electronics, 2023. 34(30): p. 2050.
18. R.M. Zahari, et al., Structural, magnetic and microwave absorption properties of $BiFe_{1-x}Y_xO_3$ ceramics synthesized by modified thermal treatment method. Journal of Materials Science: Materials in Electronics, 2021. 32(5): p. 5831-5848.
19. V. Singh, et al., Effect of Y^{3+} substitution on structural, electrical and optical properties of $BiFeO_3$ ceramics. 2014. 40(1): p. 1971-1977.
20. C.K. Lakshmi, et al., Systematic investigation of the influence of magnetic and non-magnetic ion substitutions in BiFeO3 under similar internal chemical pressure. Journal of Solid State Chemistry, 2024. 340: p. 125019.
21. I.A. Salmani, et al., Third-order optical nonlinearity and multiferroicity of nanoparticles thin films of isovalent rare earth Y^{3+} ion substituted $BiFeO_3$. Physica B: Condensed Matter, 2023. 655: p. 414750.
22. A. Tuluk, H. Brouwer, and S. van der Zwaag, Controlling the Oxygen Defects Concentration in a Pure $BiFeO_3$ Bulk Ceramic. Materials, 2022. 15(19): p. 6509.
23. T.-M. Pan, Y.-C. Chou, and J.-L. Her, Effect of Yb-doping on structural and electrical properties of $BiFeO_3$ thin films. Materials Chemistry Physics, 2022. 278: p. 125699.
24. J.M. Gómez, et al. *Structural study of yttrium substituted $BiFeO_3$*. in *Journal of physics: conference series*. 2016. IOP Publishing.
25. Y. Lin, Q. Jiang, and H. Deng, Preparation of Y^{3+} and transition metal ions codoped-$BiFeO_3$ with enhanced magnetism and photocatalytic properties. Journal of Solid State Chemistry, 2021. 303: p. 122450.
26. A. Kirsch, et al., High-entropy oxides in the mullite-type structure. Chemistry of Materials, 2023. 35(20): p. 8664-8674.
27. S. Manna, et al., Understanding and control of Zener pinning via phase field and ensemble learning. Computational Materials Science, 2023. 229: p. 112384.
28. S. Huang, et al., Enhanced piezoelectric properties by reducing leakage current in Co modified $0.7BiFeO_3$-$0.3BaTiO_3$ ceramics. Ceramics International, 2018. 44(8): p. 8955-8962.
29. V. Khomchenko, et al., Effect of Sm substitution on ferroelectric and magnetic properties of $BiFeO_3$. Scripta Materialia, 2010. 62(5): p. 238-241.
30. V. Khomchenko, et al., Doping strategies for increased performance in $BiFeO_3$. Journal of Magnetism and Magnetic Materials, 2009. 321(11): p. 1692-1698.
31. S. Zhang, et al., Phase evolution and magnetic property of $Bi_{1-x}Dy_xFeO_3$ ceramics. Materials Letters, 2009. 63(21): p. 1820-1822.
32. M. Lohchab, et al., Investigating the structural, electrical, and magnetic characteristics of Nd-doped BiFeO3 synthesized via the solid-state reaction method. Journal of Materials Research

Technology, 2024. 39(17): p. 2456-2468.
33. M. Luo, et al., Influence of Y-doping on structure, microwave dielectric and magnetic behaviors in $BiFeO_3$. Physica B: Condensed Matter, 2014. 450: p. 1-6.
34. T. Rosa, et al., Polaron-assisted dielectric relaxation processes in donor-doped $BaTiO_3$-based ceramics. Journal of Alloys Compounds, 2024. 1008: p. 176510.
35. S. Hussain, et al., Influence of rare earth ions (Dy^{3+}, Eu^{3+}, La^{3+}) on the ultraviolet-light photocatalytic activity and magnetic properties of $BiFeO_3$. Materials Chemistry Physics, 2022. 290: p. 126581.
36. L.M.S. Medina, et al., Structural, dielectric and magnetic properties of $Bi_{1-x}Y_xFeO_3$ ($0 \leq x \leq 0.2$) obtained by acid–base co-precipitation. Journal of alloys compounds, 2014. 592: p. 306-312.
37. K. Nalwa, A. Garg, and A. Upadhyaya, Effect of samarium doping on the properties of solid-state synthesized multiferroic bismuth ferrite. Materials Letters, 2008. 62(6-7): p. 878-881.
38. N. Sheoran, et al., Structural, optical, and multiferroic properties of yttrium (Y^{3+})-substituted $BiFeO_3$ nanostructures. Journal of Superconductivity Novel Magnetism, 2020. 33(7): p. 2017-2029.
39. J. Jeong, et al., Temperature-dependent interplay of Dzyaloshinskii-Moriya interaction and single-ion anisotropy in multiferroic $BiFeO_3$. Physical review letters, 2014. 113(10): p. 107202.
40. S. Alamri, et al., Enhanced microwave absorption performance of BiFeO3 nanopowders coated with Polyindole-PANI co-polymer in ku band frequency. Journal of Magnetism, 2022. 560: p. 169568.
41. A. Srivastava, et al., Magnetic and dielectric properties of La and Ni Co-substituted $BiFeO_3$ nanoceramics. Frontiers in Physics, 2020. 8: p. 282.

A Comparative Acoustic Characterisation Analysis of Malaysian Stingless Bee and Tualang Honeys

Anis Nazihah **Mat Daud**[1,2*], Nurhafizah **Hasim**[3], Sri **Maiyena**[1,4]

[1] Department of Physics, Faculty of Science and Mathematics, Universiti Pendidikan Sultan Idris, 35900 Tanjong Malim, Perak, Malaysia.
[2] STEM Nurturing Centre, Faculty of Science and Mathematics, Universiti Pendidikan Sultan Idris, 35900 Tanjong Malim, Perak, Malaysia
[3] Advanced Optical Materials Research Group, Faculty of Science, Universiti Teknologi Malaysia, 81310 UTM Johor Bahru, Johor, Malaysia.
[4] Department of Physics, Faculty of Education and Teacher Training, Mahmud Yunus Batusangkar State Islamic University, Indonesia.

*Corresponding author's phone: +6017-9055 337
E-mail: anis.md@fsmt.upsi.edu.my

Received: 28 Oktober 2025; Accepted: 25 December 2025

ABSTRACT

Malaysian stingless bee and Tualang honeys are highly valued for their therapeutic properties, yet limited studies have investigated their acoustic characteristics. This study aims to determine and compare the acoustic properties of two local honeys: Malaysian stingless bee and Tualang honeys using the ultrasonic technique. Both samples were collected from certified local sources. Their acoustic characterisation was measured using the ultrasonic pulse-echo technique under controlled room temperature. Findings indicated that Malaysian stingless bee honey demonstrated a lower longitudinal velocity but a higher attenuation coefficient compared to Tualang honey. It highlights the potential of ultrasonic characterisation as a rapid tool for honey authentication and quality control in the food industry.

Keywords—acoustic characterisation, stingless bee honey, Tualang honey, longitudinal velocity, attenuation coefficient

1.0 INTRODUCTION

Honey is a natural product highly valued for its nutritional and medicinal benefits. In Malaysia, stingless bee honey and Tualang honey are among the most consumed varieties. Stingless bee honey generally contains higher moisture levels and exhibits a lighter texture, whereas Tualang honey is typically darker, denser, and noted for its antioxidant content [1-2]. These compositional differences influence not only the sensory qualities of the honeys but also their stability, authenticity, and potential applications in functional foods.

Previous researches compared stingless bee honey and Tualang honey in term of their physicochemical properties [3-5], antibacterial properties [6], antioxidant properties [5, 7-8] and antifungal properties [9]. However, these approaches are often time-consuming and destructive.

Hence, we utilised the ultrasonic technique to measure the acoustic properties of Malaysian stingless bee and Tualang honeys in this study. The ultrasonic technique offers a rapid, non-invasive, and non-destructive alternative for analysing of liquid foods. The longitudinal velocity and attenuation coefficient of both samples were compared to provide insights into their physicochemical and structural differences.

2.0 MATERIALS

Malaysian stingless bee and Tualang honeys were collected from certified local sources in Perak. Both samples were stored at room temperature before their densities and acoustic properties were measured.

3.0 EXPERIMENTAL

The acoustic measurement system of honey samples employs the pulse-echo technique as shown in Fig. 1. The pulser/receiver generator (Olympus Panametric NDT model 5072PR) produces an electrical pulse that excites the transducer (Olympus Panametrics NDT 5 MHz) to create an ultrasound pulse. The pulse then propagates through the sample and is reflected back to its original path at the sample-air interface. Subsequently, the same transducer detects the reflected echo and then reconverts it back to an electrical pulse. Later, the pulse is amplified and conditioned using the pulser/receiver generator. Finally, the amplified pulse is displayed by a digital oscilloscope (Picoscope 3206D MSO), which is connected to a personal computer via USB connection for data processing and analysis.

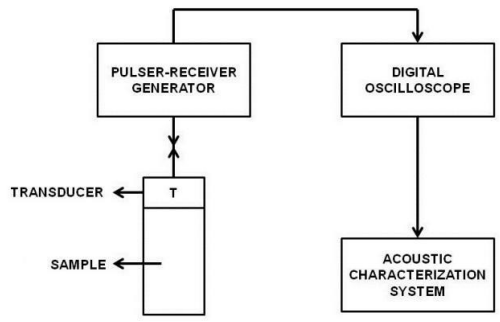

Fig. 1: Acoustic measurement system of honey samples.

Fig. 2 shows an example of a reflected signal displayed on the digital oscilloscope. The first and second reflected echoes at the sample–reflector interface are analysed to determine the acoustic properties of the sample.

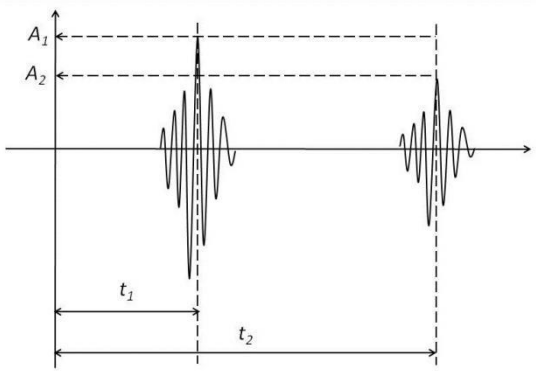

Fig. 2: The reflected signal at the sample–reflector interface.

There are two acoustic properties of honey samples were measured in this study; longitudinal velocity and attenuation coefficient. The longitudinal velocity in the sample, v_L, will be calculated from the thickness of the sample, d, the time of the first reflected echo, t_1, and the time of the second reflected echo, t_2, as shown in (1).

$$v_L = \frac{2d}{t_2 - t_1} \tag{1}$$

Meanwhile, the attenuation coefficient of the sample, α, is calculated from the amplitude of the first reflected echo, A_1, the amplitude of the second reflected echo, A_2, and the thickness of the sample, d, as shown in (2).

$$\alpha = \frac{20\, log_{10}\left[\frac{A_1}{A_2}\right]}{2d} \tag{2}$$

4.0 RESULTS AND DISCUSSION

The values of densities, longitudinal velocities and attenuation coefficient of Malaysian stingless bee and Tualang honeys are summarised in **TABLE I**.

TABLE I: Densities, longitudinal velocities and attenuation coefficients of honey samples

Sample	ρ (kg m^{-3})	v_L (ms^{-1})	α (dB cm^{-1} MHz^{-1})
Malaysian stingless bee honey	1390	2090	0.25
Tualang honey	1415	2130	0.12

According to **TABLE I**, the density and longitudinal velocity of Malaysian stingless bee honey were slightly lower compared to Tualang honey. It indicated that Malaysian stingless bee honey has higher moisture content compared to Tualang honey [10-11]. However, the attenuation coefficient of Malaysian stingless bee honey was higher than Tualang honey. It is associated with the lighter composition and higher sugar–water interactions, which contribute to stronger acoustic absorption [1-2]. Although the acoustic characterisation of honey remains relatively underexplored, ultrasonic technique has shown potential in food quality monitoring as non-invasive and rapid technique [12].

5.0 CONCLUSION

We have succesfully determine the longitudinal velocity and attenuation coefficient of Malaysian stingless bee and Tualang honeys using the ultrasonic technique. Findings indicated that the longitudinal velocity of Malaysian stingless bee honey was lower but its attenuation coefficient was higher than Tualang honey. This suggests that the ultrasonic technique provides a rapid, non-destructive method for honey authentication and quality assessment, with promising applications in food quality control.

ACKNOWLEDGEMENTS

This research was supported by the Ministry of Higher Education (MoHE) Malaysia through the Fundamental Research Grant Scheme- Early Career Researcher 2024 (Code: FRGS-EC/1/2024/STG07/UPSI/02/3). We also would like to acknowledge the facilities support from Department of Physics, Faculty of Science and Mathematics, Universiti Pendidikan Sultan Idris.

REFERENCES

1. L. C. Ng, S. B. Abd Razak, Rudiyanto, S. P. Tan, and F. T. Ahmad, “Low heating effects on the total microbial activity and physico-chemical properties of stingless bee (Heterotrigona itama) honey,” Malaysian Applied Biology, vol. 52, no. 1, pp. 43–52, 2023.
2. M. Shahbuddin, R. A. S. Raja Alias, D. Shahbuddin, and N. Ngah, “Elucidating the physicochemical properties of stingless bee honey as cryoprotectant and thermoregulated constituents,” Chemical and Natural Resources Engineering Journal, vol. 8, no. 1, pp. 1–10, 2024.
3. I. J. Fatima, A. B. Mohd Hilmi, I. Salwani, and M. Lavaniya, “Physicochemical characteristics of Malaysian stingless bee honey from Trigona species,” IIUM Medical Journal Malaysia, vol. 17, no. 1, pp. 187-191, 2023.
4. M. Majid, M. F. Abu Bakar, Z. Mian, F. Esa, and K. Y. You, “Variations of physicochemical properties of stingless bee honey from different botanical origin in state of Johor, Malaysia,” IOP Conference Series: Earth and Environmental Science, vol. 269, no. 1, pp. 012028, 2019.
5. N. I. I. Muhammad and N. M. Sarbon, “Physicochemical profile, antioxidant activity and mineral contents of honey from stingless bee and honey bee species,” Journal of Apicultural

Research, vol. 62, no. 2, pp. 394-401, 2023.
6. M. M. Aspar, R. Edros and N. A. Hamzah, "Antibacterial evaluation of Malaysian Kelulut, Tualang and Acacia honey against wound infecting bacteria," IOP Conference Series: Materials Science and Engineering, vol. 991, no. 1, pp. 012065, 2020.
7. Y. Ranneh, F. Ali, M. Zarei, A. M. Akim, H. Abd Hamid and H. Khazaai, "Malaysian stingless bee and Tualang honeys: A comparative characterization of total antioxidant capacity and phenolic profile using liquid chromatography-mass spectrometry," LWT, vol. 89, pp. 1-9, 2018.
8. K. A. Sakika, M. Z. Saiman, N. H. Zamakshshari, I. A. Ahmed, M. N. A. Nasharuddin and N. M. Hashim, "Analysis of antioxidant properties and volatile compounds of honeys from different botanical and geographical origins," Sains Malaysiana, vol. 51, no. 4, pp. 1111-1121, 2022.
9. A. Shehu, S. Ismail, M. A. K. Rohin, A. Harun, A. Abd Aziz, and M. Haque, "Antifungal properties of Malaysian Tualang honey and stingless bee propolis against Candida albicans and Cryptococcus neoformans," Journal of Applied Pharmaceutical Science, vol. 6, no. 2, pp. 044-050, 2016.
10. N. A. F. Ramlan, E. M. Azman, K. Muhammad, A. Z. Jusoh, N. A. Johari, Y. A. Yusof, and N. Zawawi, "Physicochemical homogeneity of stingless bee honey (Heterotrigona itama) produced in different regions of Peninsular Malaysia," Journal of the Science of Food and Agriculture, vol. 104, no. 3, pp. 1756–1767, 2023.
11. I. S. R. Sujanto, N. S. Ramly, A. Abd Ghani, J. Y. H. Tang, N. Alias, and N. Ngah, "The physicochemical properties and nutritional value of stingless bee honey at Gelam Forest in Telaga Papan, Terengganu, Malaysia," Journal of Agro-biotechnology, vol. 12, no. 2, pp. 108–120, 2021.
12. S. H. Tan, P. P. Liew, M. I. Solihin, S. K. Kong and K. A. Chun, "Physicochemical analysis and adulteration detection in Malaysian stingless bee honey using a handheld near-infrared spectrometer," Journal of Food Processing and Preservation, vol. 45, no. 7, pp. e15576, 2021.

Proceeding of the 9th International Symposium on Advanced Materials and Nanotechnology (iSAMN2025), October 29-30, 2025

Selective Growth and Characterization of Nanostructured Mo_6SnS_8 Chevrel Phase Thin Films: Structural, Optical, and Electrical Properties

S.M. **Aldosari**[1], Ftema W. **Aldbea***[2], A. **Boukhachem**[3]

[1] Innovation Parks, King Abdulaziz City for Science and Technology (KACST), Riyadh, 11442, Saudi Arabia
[2] Physics Department, Faculty of Science, Sebha University, Sebha, Libya
[3]Laboratory of Nanomaterials and Renewable Energy Systems, Research and Technology Center of Energy. Tunisia

* Corresponding author's phone: fte.aldbea@sebhau.edu.ly
Email: +218-911452162

Received: 01 October 2025; Accepted: 01 December 2025

ABSTRACT

The chevrel phase compound with the formula of $MnMo_6X_8$ is an important material that can be used for many applications, such as energy storage and electrocatalysis. Therefore, this work aims to produce Mo_6SnS_8 thin film using the spray pyrolysis technique and study its structural, optical, and electrical properties. The Mo6SnS8 ternary thin film has been prepared by the spray pyrolysis technique at a temperature of 250°C. Characterization via X-ray diffraction (XRD), spectrophotometry through reflectance and transmittance measurements, and electrical analysis via impedance spectroscopy were performed. X-ray analysis shows that the Mo6SnS8 material has a rhombohedral structure with a preferred orientation of the crystallites along the (110) direction parallel to the substrate plane. Optical measurements show a direct transition and energy gap of 3.60 eV. Electrical properties were measured using impedance spectroscopy technique over the frequency range 5 Hz–13 MHz at various temperatures. DC conductivity is thermally activated, showing a semiconductor behavior. A good semiconductor behavior observed for the $Mo6SnS_8$ film annealed at a low temperature.

Keywords— Thin film, spray pyrolysis, chevrel, semiconductor, XRD

1.0. INTRODUCTION

The chevrel phase with the formula of $M_xMo_6T_8$, where M is a metal; T = S, Se, or Te has received more attention because it exhibits a unique properties in science and technology fields [1]. Among the chevrel phase family, the molybdenum sulfide (Mo_6S_8) is one of the important compound where its crystal structure is related to $R\bar{3}$ space group with $a = b =$ 9.1833Å and c = 10.8716Å[2]. The Mo_6S_8 is considered an important material showing excellent physical and chemical properties. Therefore, it is a good candidate material to be suitable for energy storage, solar cells, and photocatalytic applications[1][3]. Many methods were used to prepare Mo_6S_8 material, such as sol- gel [4], hydrothermal [5], precipitation and spray pyrolysis [6]. In these methods, many elements were added to the Mo_6S_8 structure, such as Zn, Al, Cu, Mg, etc, in order to enhance its structural, optical and electrical properties [7][8][9]. Although many studies have been conducted on doped Mo_6S_8 with several elements, and they studied its physical and chemical properties, no study has been published about the spray pyrolysis of Mo_6SnS_8 thin film. In this work, the Mo_6SnS_8 thin film was prepared by using the spray pyrolysis and study its structural, optical and electrical properties

2.0. EXPERIMENTAL

The Mo_6SnS_8 thin film was deposited on a glass substrate at 250° C using 0.01 M of tin chloride hexahydrate ($SnCl_2$. $6H_2O$) and 610-2/7 M of Ammonium molybdate tetrahydrate [$(NH_4)_6Mo_7O_{24}.4H_2O$] and thiourea ($SC(NH_2)_2$, 20 10−2 M) aqueous solution. During the solution spraying, the nitrogen was used as carrier gas (pressure at 0.35 bar) through a 0.5 mm-diameter nozzle with a fixed nozzle-to-substrate plane distance of 27 cm and a flow rate was maintained at 4 mL/min. In addition, the substrate temperature was controlled by a thermocouple located on a metallic hot plate surface. After the deposition process, the coated substrate was kept cooling down naturally to room temperature.

2.1. Characterization

The structural measurements of the sample were performed using a Philips PW1710 X-ray diffractometer (XRD). This instrument uses CuKα radiation (λ = 0.154059 nm) and operates over a 2θ range between 10◦ and 70◦. The optical properties of the samples were measured using Schimadzu UV 3100 double-beam spectrophotometer, with the wavelength range of 300 - 2500 nm. The impedance measurements were recorded using the Hewlett–Packard HP4192 impedance analyzer. Where the real and imaginary components were measured at the temperature range of 295–355°C and in the frequency range (5 Hz–13 MHz).

3. RESULTS AND DISCUSSION

3.1 XRD analysis

Fig.1, shows the XRD pattern of Mo_6SnS_8 thin film. The sample has a single pure chevrel phase with the rhombohedral structure according to the JCPDS card no #01-08-1709[10]. The strong peak intensity due to enhance the crystallinity of the sample. Furthermore, the peak position is shifted to the right side which is a sign of the Sn incorporated into Mo_6SnS_8 structure[11]. The lattice parameters of the rhombohedral structure were determined using the unit cell software[12]. It is found that the lattice parameter values of Mo_6SnS_8 thin film were a= 9.466 Å and c= 10.736 Å. This value is close to the standard value of lattice parameters for pure Mo_6S_8 (a= 9.1833Å, and c= 10.8716Å) [13]. The cell volume value is about 833.205 $Å^3$. The large value of cell volume is attributed to the Sn entered into Mo_6S_8 structure.

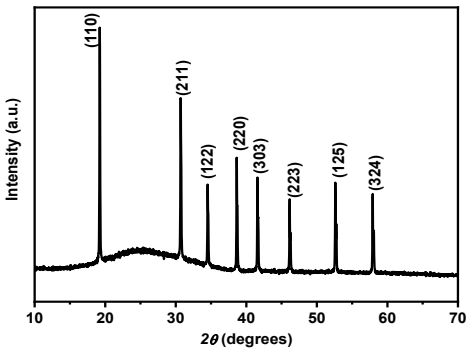

Fig.1: The XRD pattern of Mo_6SnS_8 thin film

3.2. Optical measurements

Fig. 2, shows the transmittance, reflectance and absorbance spectra of Mo_6SnS_8 thin film, which occurred below a wavelength value of 600 nm. It can be seen that, the sample showed transmittance, reflectance and absorbance values of ~ 16%, 15%, and 70%, respectively. The high absorbance value indicates that the sample is suitable for photocatalytic applications.

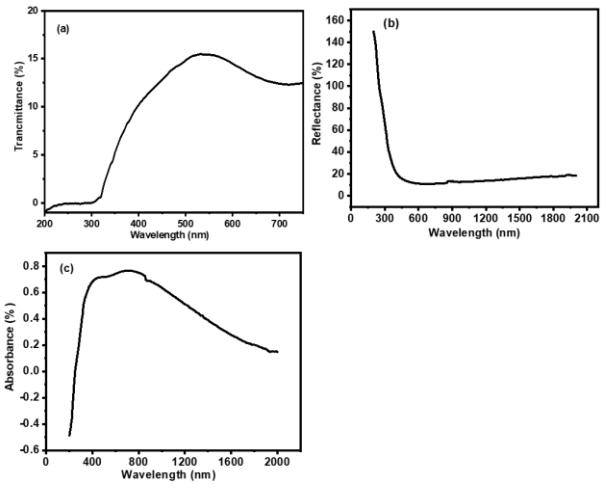

Fig 2: (a) transmittance, (b) reflectance and (c absorbance of Mo_6SnS_8 thin film

The absorption coefficient (α) is estimated from absorbance spectra using the formula[14]:

$$\alpha(\lambda) = ln\frac{(1-R(\lambda))^2}{T(\lambda)} \quad (1)$$

where R is the reflectance and T is the transmittance. The value of α was in the range of 10^6 cm^{-1} (Fig 3a), which is the same range as strong semiconductor materials with the direct band gap (α between 10^4- 10^6 cm^{-1})[15].

The energy gap (E_g) of the thin film was estimated using the formula[16]:

$$(\alpha h\nu) = A(h\nu - E_g)^n \quad (2)$$

where n has two values, $\frac{1}{2}$ for direct and n=1 for indirect energy gap, h is Planck's constant, and ν is the frequency. The Mo_6SnS_8 thin film has a direct E_g. Therefore, to determine the E_g value, the transition is allowed to find the best fit for the extrapolation for the x- axis. Then, the direct E_g value was estimated from the Tauc plot of $(\alpha h\nu)^2$ versus $h\nu$ (see Fig 3b). From the Figure it, can be seen that the sample has an energy gap value of about 3.60 eV, which is higher than 1.76 eV for $Ni_2Mo_6S_8$ [9]. The optical properties of the chevrel phase are still under investigation.

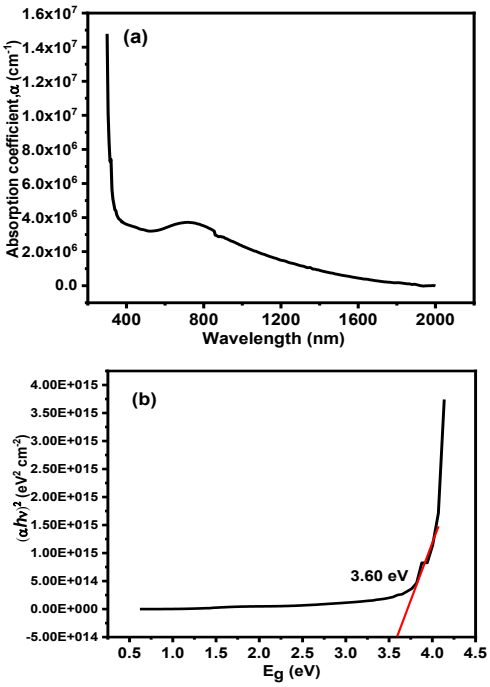

Fig 3: (a) absorption coefficient and (b) energy gap of Mo_6SnS_8 thin film

3.3. Electrical analysis

Fig 4 , shows the impedance analysis of the Mo_6SnS_8 thin film at the temperature ranges from 295 to 355 °C. Fig 4a shows the imaginary part (Z´´) against real part (Z´) (Nyquist plot). From the Figure, it can be seen that the semi-circles are shifted to the low frequency as the temperature is increased to 355°C due to a small contribution from impedance equipment[17]. Also, the single arc indicates that relaxation process occurred in the film; in this case, the parallel RC circuit was used [18]. Furthermore, the decrease in the semi-circles` diameters with increased temperature is a sign to enhance the electrical conductivity and the reduction in the bulk resistance [19]. The variation of the Z´´ with the frequency of the film at different temperatures is illustrated in Fig 4b. A high relaxation peak of the film appeared at a low temperature value of 295 °C. Then, this peak is decreased with increased the temperature, and it shifted to the higher frequency value, which referred to the thermal activation of local charge carriers and a temperature-dependent relaxation time[6].

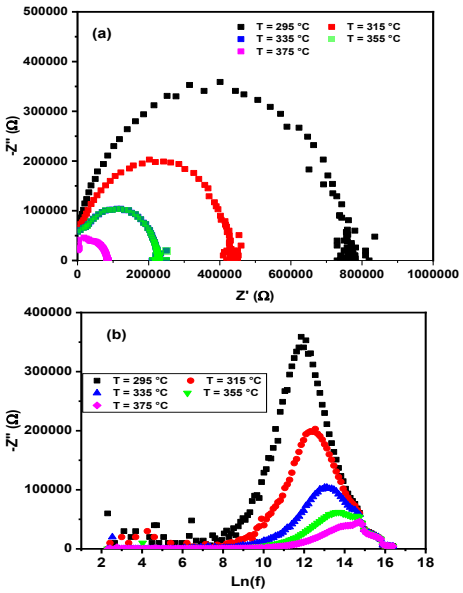

Fig 4: (a) variation of the real and imaginary parts (b) variation of imaginary component with the frequency at different temperature of Mo_6SnS_8 thin film

Fig. 5, shows the relation between ionic conductivity (ln σ) and the temperature (1000/T). The results show a linear drop and the regression value (R^2) of 0.99 near to unity, which matches with the Arrhenius law (Eq(3)[20]:

$$\sigma = \sigma_0 \exp\left(\frac{-E_a}{k_B T}\right) \quad (3)$$

Where σ is the ionic conductivity, σ_0 is the exponential factor, E_a is the activation energy (eV), k_B is the Boltzmann constant (8.617 x10^{-5} eV/K) and T is the absolute temperature (K).

The value of E_a was found to be about 0.88 eV, which means the ionic mobility is poor at lower temperatures as this value indicates the semiconductor behavior with a high activation energy[20][21].

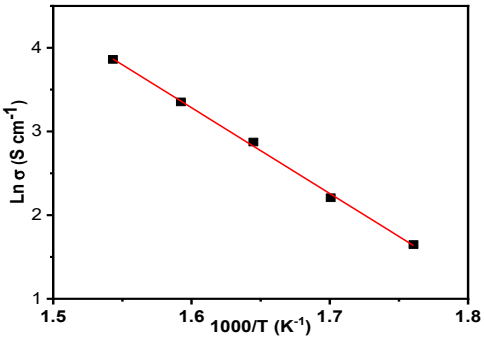

Fig 5: the relation between ionic conductivity (ln σ) and the temperature (1000/T)

The variation of ln (σ) against ln (f) (f was selected from 3 Hz to 13MHz) at different temperatures is shown in the Fig 6, where σ is the measured conductivity, which contains two terms, dc and ac conductivities, according to the following formula[22]:

$$\sigma = \sigma_{ac} + \sigma_{dc} \quad (4)$$

At low frequency values, σ is approximately independent; this might be related to the σ_{dc} contribution[22]. The conductivity observed to increase linearly in the higher frequency range. The mechanism of this behavior can be explained by correlated barrier hopping (CBH) model, where the ions mostly transfer through a material by hopping between sites. The hopping probability between nearby sites is correlated, resulting in a frequency-dependent AC conductivity[23].

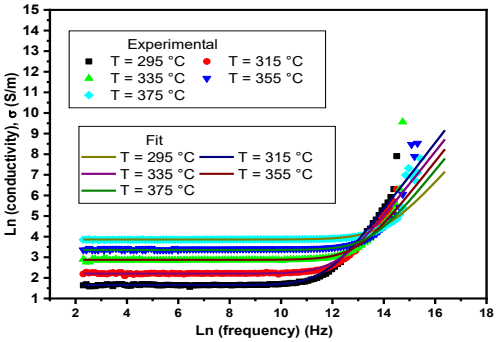

Fig 6: the plot of ln(σt) versus ln(f) at different temperatures for Mo_6SnS_8 thin film

Fig.7, illustrates the variation of the exponent s with the temperature. The s value was determined from the slope of logarithmic conductivity against frequency (it is not shown in this work). It can be seen that, the value of s decreased with the temperature. This gives an idea that the charge is being bound in traps-like manner[19]. The value of s is recorded to be -0.003, which is smaller than the value of the energy gap (weak charge bond). This result is reasonable due to the increase in conductivity[21].

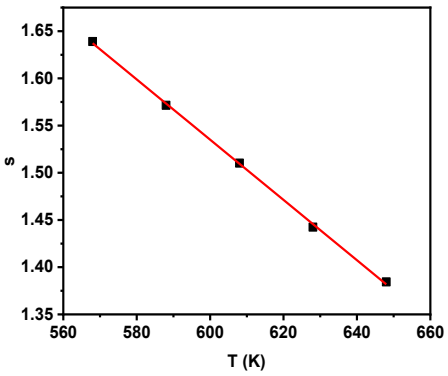

Fig 7: the plot of s versus T for Mo_6SnS_8 thin film

4.0 CONCLUSIONS

The Mo_6SnS_8 thin film was prepared using the spray pyrolysis technique at a temperature of 250 °C. The film has a

rhombohedral crystal structure with a preferred orientation of the crystallites along the (110) plane. The optical measurement of the thin film exhibits a strong absorption spectrum and a high direct energy gap. The electrical properties of the film illustrated a high activation energy and a strong semiconductor behavior. This unusual behavior will be investigated in the Future work

REFERENCES

[1] M. Liu *et al.*, "Chevrel phase: A review of its crystal structure and electrochemical properties," *Prog. Nat. Sci. Mater. Int.*, vol. 33, no. 1, pp. 8–15, 2023, doi: https://doi.org/10.1016/j.pnsc.2023.01.002.

[2] L. Geng, J. P. Scheifers, J. Zhang, K. N. Bozhilov, B. P. T. Fokwa, and J. Guo, "Crystal Structure Transformation in Chevrel Phase Mo6S8 Induced by Aluminum Intercalation," *Chem. Mater.*, vol. 30, no. 23, pp. 8420–8425, Dec. 2018, doi: 10.1021/acs.chemmater.8b03312.

[3] M. L. Agiorgousis, Y. Sun, D. J. West, and S. Zhang, "Material for Energy Generation and Storage Intercalated Chevrel Phase Mo 6 S 8 as a Janus Material for Energy Generation and Storage," 2018, doi: 10.1021/acsaem.7b00092.

[4] S. Boursicot, V. Bouquet, I. Péron, T. Guizouarn, M. Potel, and M. Guilloux-Viry, "ChemInform Abstract: Synthesis of Cu2Mo6S8 Powders and Thin Films from Intermediate Oxides Prepared by Polymeric Precursor Method.," *Solid State Sci.*, vol. 14, pp. 719–724, Jun. 2012, doi: 10.1016/j.solidstatesciences.2012.03.013.

[5] X. Xu, M. Zhang, J. Wu, Z. Shen, Y. Liu, and L. Wang, "Advanced Progress of Non-Stoichiometric Transition Metal Sulfides for Sensing, Catalysis, and Energy Storage," *Nanomaterials*, vol. 15, no. 16, p. 1237, 2025.

[6] P. Saha, P. H. Jampani, M. K. Datta, C. U. Okoli, A. Manivannan, and P. N. Kumta, " A Convenient Approach to Mo 6 S 8 Chevrel Phase Cathode for Rechargeable Magnesium Battery ," *J. Electrochem. Soc.*, vol. 161, no. 4, pp. A593–A598, 2014, doi: 10.1149/2.061404jes.

[7] P. Yu *et al.*, "The evolution of local structure of Mo6S8 during Li+ electrochemical storage studied by in-situ tender X-ray absorption spectroscopy," *Prog. Nat. Sci. Mater. Int.*, vol. 32, no. 6, pp. 739–744, 2022, doi: https://doi.org/10.1016/j.pnsc.2022.09.006.

[8] X. Qi *et al.*, "Surface Optimization of Mg Metal Electrodes by Tuning Pilling–Bedworth Ratio for Long-Life Mg Batteries," *Renewables*, vol. 3, no. 2, pp. 77–86, 2025, doi: 10.31635/renewables.025.20250008 1.

[9] M. Pawar, A. Annerino, J. Shell, and P.-I. Gouma, "Photocatalytic Desulfurization of Thiophene with Chevrel Phase Ni2Mo6S8 Synthesized by SHS," *ACS Omega*, vol. 9, no. 31, pp. 33935–33940, Aug. 2024, doi: 10.1021/acsomega.4c04213.

[10] K. M. Naik and S. Sampath, "Cubic Mo6S8-Efficient Electrocatalyst Towards Hydrogen Evolution Over Wide pH Range," *Electrochim. Acta*, vol. 252, pp. 408–415, 2017, doi: https://doi.org/10.1016/j.electacta.2017.09.015.

[11] F. W. Aldbea, N. B. Ibrahim, and M. Yahya, "Effect of adding aluminum ion on the structural, optical, electrical and magnetic properties of terbium doped yttrium iron garnet nanoparticles films prepared by sol-gel method," *Appl. Surf. Sci.*, vol. 321, 2014, doi: 10.1016/j.apsusc.2014.10.019.

[12] T. J. B. Holland and S. A. T. Redfern, "Unit cell refinement from powder diffraction data: the use of regression diagnostics," *Mineral. Mag.*, vol. 61, no. 404, pp. 65–77, 1997, doi: DOI: 10.1180/minmag.1997.061.404.07.

[13] M. S. Chae, J. W. Heo, S.-C. Lim, and S.-T. Hong, "Electrochemical Zinc-Ion Intercalation Properties and Crystal Structures of ZnMo6S8 and Zn2Mo6S8 Chevrel Phases in Aqueous Electrolytes," *Inorg. Chem.*, vol. 55, no. 7, pp. 3294–3301, Apr. 2016, doi: 10.1021/acs.inorgchem.5b02362.

[14] M. Allaham *et al.*, "Energy gap measurements based on enhanced absorption coefficient calculation from transmittance and reflectance raw data," *Phys. Scr.*, vol. 99, no. 2, pp. 1–9, 2024, doi: 10.1088/1402-4896/ad1cb8.

[15] H. J. Lee, M. M. A. Gamel, P. J. Ker, M. Z. Jamaludin, Y. H. Wong, and J. P. R. David, "Absorption Coefficient of Bulk III-V Semiconductor Materials: A Review on Methods, Properties and Future Prospects," *J. Electron. Mater.*, vol. 51, no. 11, pp. 6082–6107, 2022, doi: 10.1007/s11664-022-09846-7.

[16] H. H. Kusuma, M. K. Saidin, and Z. Ibrahim, "Optical properties of Ti: Al2O3 single crystal," *J. Fiz. UTM*, vol. 4, pp. 42–49, 2009.

[17] A. Huanosta, J. C. Alonso, and A. Ortiz, "Spectroscopic impedance studies of Al2O3 films deposited by spray pyrolysis," *Thin Solid Films*, vol. 401, no. 1, pp. 284–290, 2001, doi: https://doi.org/10.1016/S0040-6090(01)01621-2.

[18] A. Manan, G. S. Jahan, M. U. Rehman, and M. T. Lanagan, "Synthesis, dielectric and impedance spectroscopy study of temperature stable Ta2O5 modified 0.85BaTiO3-0.15Bi(Mg0.5Ti0.5)O3 ceramics," *Chem. Phys. Impact*, vol. 7, p. 100376, 2023, doi: https://doi.org/10.1016/j.chphi.2023.100376.

[19] M. N. Hafiza and M. I. N. Isa, "Conduction mechanism via correlated barrier hopping in EC-plasticized 2-hydroxyehyl cellulose-ammonium nitrate solid polymer electrolyte," *IOP Conf. Ser. Mater. Sci. Eng.*, vol. 440, no. 1, 2018, doi: 10.1088/1757-899X/440/1/012039.

[20] N. Kumar, S. K. Patri, and R. N. P. Choudhary, "Frequency-temperature response of a new multiferroic," *Process. Appl. Ceram.*, vol. 8, no. 3, pp. 121–125, 2014, doi: 10.2298/PAC1403121K.

[21] R. M. Rudenko, O. O. Voitsihovska, and V. N. Poroshin, "Sequential change of semiconductor mechanisms of electrical conductivity in ternary PVDF/polyaniline/MWCNT nanocomposite in the wide temperature range of 4.2–340 K," *Mater. Lett.*, vol. 350, p. 134976, 2023, doi: https://doi.org/10.1016/j.matlet.2023.134976.

[22] M. Jebli, C. Rayssi, J. Dhahri, and K. Khirouni, "Investigation of electrical properties and conduction mechanism using CBH model of

Ba0.97La0.02Ti1−xNb4x/5O3 (x = 0.00 and 0.02) compounds," *Appl. Phys. A*, vol. 126, no. 2, p. 109, 2020, doi: 10.1007/s00339-020-3298-x.

[23] P. Dhuria, S. S. Bhamra, and J. S. Hundal, "The study of Correlated Barrier Hopping (CBH) conduction mechanism and modulus spectroscopy of YFe0.5Co0.5O3 compound," *Phys. B Condens. Matter*, vol. 677, p. 415696, 2024, doi: https://doi.org/10.1016/j.physb.2024.415696.

Characterization of Biofilms Based on Agar, Gelatin, and Cornstarch Incorporating Glycerin as a Plasticizer

Nurul Jannah Ibrahim[1], Sitti Fatimah Mhd Ramle[1*]

[1]Faculty of Bioengineering Technology, Universiti Malaysia Kelantan, 17600 Jeli, Kelantan, Malaysia.

*Corresponding author's phone: +6019-413 8433
E-mail: fatimah.m@umk.edu.my* nurul.janna201208@gmail.com

Received: 30 October 2025; Accepted: 1 December 2025

ABSTRACT

This study explores the development and characterisation of biodegradable biofilms utilising agar, gelatin, and cornstarch as natural polymer bases, each integrated with 20% glycerin as a plasticiser to enhance flexibility and reduce brittleness. Preparation involved thermal processing (boiling) for a duration of 15–20 minutes. Agar solutions were boiled for 15 or 20 minutes before casting. All cast films were then left to dry for a few days at room temperature (20–25°C) until fully set. The resulting movies were systematically profiled for important performance parameters: moisture content (determined by gravimetric analysis post-drying), solubility (measured by mass loss post-immersion in water), biodegradability (measured by environmental degradation assays), and mechanical strength (analysed using tensile testing for stress-strain characteristics). Gelatin-glycerin films exhibited the lowest moisture content (15.38-16.09%) and highest tensile strength (6.34 MPa) with remarkable elongation at break (156.45%), indicating their strong potential for flexible wrapping, cosmetic layers, or biomedical scaffolds. Agar-based films exhibited balanced mechanical properties (4.75 MPa, 52.95% elongation), high water solubility (42.1-52.08%), and moderate moisture retention, making them suitable for edible coatings or semi-rigid packaging. Cornstarch films, though naturally biodegradable, demonstrated lower tensile strength (2.54 MPa) and reduced solubility and water absorption over time, making them suitable for disposable rigid biofilms. Overall, the incorporation of glycerin effectively improved plasticity across all formulations, and the data underscores the significance of polymer selection and thermal processing in tailoring biofilms for sustainable applications in food packaging, personal care, and eco-friendly materials.

Keywords — Water absorption; Mechanical; Moisture Content; Sustainable; Packaging

1.0 INTRODUCTION

The global reliance on petroleum-based plastics has led to escalating environmental concerns, particularly due to their persistence in ecosystems and their contribution to pollution. As sustainability awareness grows, the development of biodegradable alternatives has gained significant momentum. Biopolymer-based films derived from natural sources offer a promising solution, especially when formulated from agro-waste and renewable materials. Although these plastics significantly support the global economy, generating billions of dollars, their resistance to degradation poses a significant environmental challenge, resulting in severe ecological problems (Ahmad, 2018).

Agar, gelatin, and cornstarch were selected to represent the three major classes of biodegradable biopolymers (plant polysaccharide, animal protein, and seaweed polysaccharide, respectively) to facilitate a comprehensive comparative

study of how material source influences the mechanical properties, water sensitivity, and application potential of thermally processed films, ranging from low-cost, rigid packaging to highly flexible, elastic scaffolds. Agar, a polysaccharide extracted from red algae, forms transparent and flexible films with high solubility. Gelatin, a protein derived from collagen, provides excellent mechanical strength and elasticity. Cornstarch, a carbohydrate-based polymer, offers rigidity and water resistance but often requires plasticizers to improve flexibility.

Glycerin is widely utilized as a plasticizer, humectant, emollient, and solvent in food flavoring and coloring. Being highly hygroscopic, it can be incorporated into film-forming solutions to decrease film brittleness (Viera, 2011). Glycerin is commonly incorporated to enhance the mechanical properties and reduce brittleness of biofilms. Its compatibility with hydrophilic polymers makes it ideal for improving film flexibility and moisture retention. In this study, glycerin was incorporated at a fixed concentration of 20% (w/w) based on the total polymer mass across all three biopolymer formulations.

This study aims to develop and characterize biofilms based on agar, gelatin, and cornstarch incorporating glycerin, focusing on their moisture content, solubility, tensile strength, biodegradability, and surface morphology. By comparing the effects of polymer type and boiling duration, which significantly influence the molecular structure and density of the film, this research seeks to identify optimal formulations for sustainable packaging applications and contribute to advancing circular economy principles.

2.0 THEORY/LITERATURE REVIEW

Biopolymer-based biofilms, particularly those derived from agar, gelatin, and cornstarch, offer promising alternatives to petroleum-based plastics due to their biodegradability and film-forming capabilities. Agar's gel-forming polysaccharide structure supports high solubility and moderate strength, while gelatin's protein matrix provides superior elasticity and rapid environmental breakdown. Cornstarch, though cost-effective and biodegradable, requires plasticizer enhancement to overcome brittleness. Glycerin improves flexibility by disrupting hydrogen bonding and increasing polymer mobility. The role of polymer type and plasticizer concentration in tailoring mechanical, moisture, and degradation properties for sustainable biofilm applications (Fathiraja, 2022). However, in this study, the glycerin concentration was consistently fixed at 20% to isolate the effects of polymer type and boiling duration.

3.0 MATERIALS

In this experiment, agar (Food Grade, extracted out of algae (Japanese origin), gelatin (Food Grade, extracted out of fish), and cornstarch (Regular Food Grade) were dissolved in distilled water separately and mixed with 20% glycerin, vegetable-based, 99.5% purity (Food Grade), as a plasticizer. All solutions were prepared using an analytical balance and heated using a magnetic stirrer.

4.0 EXPERIMENTAL

The biofilms were prepared by dissolving each of the biopolymers separately agar (AG), gelatin (GG), and cornstarch (CG) in 100 mL of distilled water with glycerin used as the plasticizer at a constant proportion of 20% of the total polymer weight. All mixtures were heated using a magnetic stirrer hot plate to 60°C to allow complete dissolution. The solutions obtained were then boiled for 15 or 20 minutes to determine the effect of thermal processing time**.** Lastly, the warm solutions were solution-cast onto a silicone mould with 20mL of solution and left to dry

completely at room temperature (20–25°C) over several days.

4.1 Biofilm Formulation

Biofilm is produced by mixing agar (20%:20%), gelatin (50%:20%), and cornstarch (50%:20%). This mixture is suitable for each different material. Each formulation incorporates glycerin at consistent concentration of 20% based on the total polymer mass, serving as a plasticizer to enhance flexibility and reduce brittleness as shown in Fig. 1.

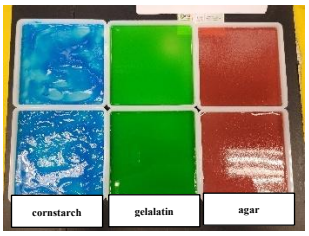

Fig. 1: Biofilm made from Cornstarch, Gelatin and Agar

To investigate the effect of thermal processing, the biofilm is subjected to two boiling durations 15 minutes and 20 minutes before casting. The variable aims to assess how boiling time influences the physicochemical characteristics of the film, including structural uniformity and mechanical strength.

4.2 Characterization Biofilm

Various physical and mechanical parameters were examined to evaluate the quality and functionality of the biofilms produced from agar, gelatin, and cornstarch with glycerin. Moisture content and water/alcohol solubility tests were conducted to determine the films' hydration and dissolution behaviours. Water absorption was assessed to determine the film's moisture-retention capacity. Biodegradability tests provided insight into the environmental impact of each formulation. Tensile strength analysis measured the films' mechanical durability which was recorded for comparative evaluation.

4.2.1 Moisture Content

Boiling time is crucial for modifying the molecular structure and moisture characteristics of biopolymer-based films. The content of moisture was calculated by weighing the sample of biofilm before and after 24 hours of oven drying at 85°C for 24 hours as shown in Table I. The moisture percentage was determined by using formula 1:

$$Moisture\ Content\ (\%) = ((\frac{(W1 - W2)}{W1}) \times 100)$$

4.2.2 Solubility of Water and Alcohol

Solubility was determined by weighing dried biofilm samples (W1) as indicated in Table II, immersed in 50 mL of distilled water and 3 mL of ethanol at room temperature after 24 hours, then filtering and air-drying the residue after another 24 hours (W2). The choice of solvents (both distilled water and ethanol) represents two different polarity conditions: water is a hydrophilic/aqueous environment (relevant to food packaging or edible use), and ethanol is a lipophilic/alcohol-rich environment (relevant to pharmaceutical or cosmetic use), to compare the dissolution behaviour of both biofilms comprehensively. The solubility (%) was determined based on formula 2:

$$Solubility\ (\%) = ((\frac{(W1 - W2)}{W1}) \times 100)$$

4.2.3 Water Absorption

Results indicate the absorption behaviour of biopolymer films made from agar, gelatin and cornstarch mixed with glycerin at 15 and 20 minutes of exposure, as indicated in Table III. The absorption of water was measured by drying the biofilm samples at room temperature for 24 hours

to record their initial weight (W1). The samples were again immersed in distilled water overnight, filtered and reweighed (W2). The percentage of absorption was determined by formula 3:

$$Water\ Abrp.(\%) = (\left(\frac{(W1 - W2)}{W1}\right) \times 100)$$

4.2.4 Biodegradability Test

The biodegradability of agar (AG), gelatine (GG), and cornstarch (CG) biofilms containing glycerine was evaluated in soil and wet sand environments, and Table IV showed different degradation patterns. To mimic natural soil biodegradation conditions typically found in composting or landfill settings, soil was used, and to mimic a moisture-saturated environment with specific microbial communities, wet sand (saturated with river water) was used, allowing a comparative evaluation of biodegradation behaviour in two environmentally relevant media. Biodegradability was evaluated by weighing dry biofilm samples (W1) and burying them in soil or wet sand for 1 week. The rest was then cleaned, dried and reweighed (W2). The percentage of biodegradation was calculated using formula 4:

$$Biodegradable(\%) = ((\frac{(W1 - W2)}{W1}) \times 100)$$

This study employs the acronym AG, GG, and CG to represent the three different biofilm formulations, all of which include Glycerin as a plasticizer. AG is the abbreviation of Agar-Glycerin formulation, GG is the Gelatin-Glycerin film, and CG is the Cornstarch-Glycerin biofilm.

5.0 RESULTS AND DISCUSSION

5.1 Moisture Content

Table I: Biofilm Moisture Content (%) Data analysis

Sampel	Data		
	W1	W2	Moisture Content%
AG 15	0.55	0.37	32.73
AG 20	0.84	0.6	28.57
GG 15	0.87	0.73	16.09
GG 20	1.56	1.32	15.38
CG 15	0.61	0.5	18.03
CG 20	0.84	0.68	19.04

Agar-based biofilms' moisture content decreased slightly from 32.73% after 15 minutes of boiling to 28.57% at 20 minutes. Agar's gel network tightens during prolonged boiling, potentially reducing its water-holding capacity by strengthening polymer interactions (Amira, 2023). This suggests that extended boiling time produces denser agar films with lower moisture affinity.

Gelatin films, on the other hand, showed the lowest moisture content overall, recording 16.09% at 15 minutes and 15.38% at 20 minutes. The decrease is marginal but reflects the compact nature of gelatin's protein matrix. Extended boiling may promote tighter crosslinking (Walid, 2021), further limiting water uptake. Cornstarch films recorded slightly increasing moisture levels of 18.03% at 15 minutes and 19.04% at 20 minutes. This suggests that longer boiling may expand starch granules or expose more hydrophilic sites, increasing water retention (Jatin, 2019).

Overall, gelatine films were the least moisture-retentive, regardless of boiling time; agar films were more sensitive to thermal treatment when plasticised, especially in terms of moisture absorption (Rusli, 2016). While starch-based films can

become more moisture-absorbent with thermal modification, depending on the extent of gelatinization and matrix porosity (Budsaereechai, 2021). These findings highlight how thermal processing time during film formation can fine-tune moisture behaviour across different biopolymers.

5.2 Solubility in water and alcohol

Table II: Solubility in Water and Alcohol (%) Data Analysis

Sampel	Solubility of Water		
	W1	W2	Solubility %
AG 15	0.38	0.22	42.1
AG 20	0.48	0.23	52.08
GG 15	0.57	0.44	22.8
GG 20	1.08	0.83	23.14
CG 15	0.45	0.33	26.66
CG 20	0.35	0.30	14.23
Sampel	**Solubility of Alcohol**		
AG 15	0.58	0.38	34.48
AG 20	0.41	0.25	39.02
GG 15	0.61	0.58	4.91
GG 20	0.92	0.83	9.78
CG 15	0.35	0.23	34.28
CG 20	0.78	0.75	3.84

The solubility profiles of agar (AG), gelatine (GG), and cornstarch (CG) biofilms in water and alcohol reveal distinct time-dependent behaviours influenced by polymer structure and glycerine plasticization. AG films exhibited the highest solubility in both solvents, increasing from 42.10% to 52.08% in water and 34.48% to 39.02% in alcohol over 15 to 20 minutes. This trend reflects agar's hydrophilic polysaccharide backbone and its susceptibility to matrix loosening, further enhanced by glycerine's facilitation of solvent permeation (Asma, 2016). GG films maintained low solubility across both media (water: 22.80–23.14%; alcohol: 4.91–9.78%), indicating a stable protein network with limited responsiveness, likely due to cross-linking that resists hydration and ethanol diffusion (Asma, 2016). CG films showed a marked decline in solubility over time (water: 26.66% to 14.23%; alcohol: 34.28% to 3.84%), suggesting retrogradation or crystallisation that restricts solvent access.

The discussion highlights how biofilm composition and exposure duration critically shape solubility behaviour. AG's increased solubility supports its use in time-sensitive applications such as edible wraps or drug carriers. GG's stability suits humid or alcohol-rich environments, while CG's declining solubility signals caution for long-term aqueous exposure. These findings reinforce Gholamreza et al. (2021), emphasizing the interplay of glycerine and polymer type in tailoring biopolymer performance for specific functional needs.

5.3 Water Absorption

Table III: Biofilm Water Absorption (%) Data analysis

Sampel	Data		
	W1	W2	Biofilm Water Absorption %
AG 15	0.72	1.68	133.3
AG 20	0.86	2.34	172.1
GG 15	0.77	13.91	171
GG 20	1.2	32.91	264
CG 15	0.73	1.51	106.8
CG 20	1.13	2.18	92.92

AG films showed consistently high absorption (146.67% to 153.33%), reflecting agar's hydrophilic polysaccharide structure and glycerines plasticizing effect (Rusli, 2016). GG films increased from 85.71% to 126.66%, suggesting a gradual loosening of the protein matrix and enhanced water uptake (Gholamreze, 2021). In contrast, CG films

declined from 172.72% to 166.66%, likely due to retrogradation or crystalline rearrangement that restricts water ingress (Gholamreze, 2021). The discussion highlights how biofilm composition and exposure time influence moisture responsiveness. AG and GG films are promising for biomedical or edible applications requiring high water absorption, while CG's behaviour suits applications requiring initial swelling ability with later structural integrity. These trends align with those of Gholamreza et al. (2021), emphasising the roles of plasticiser concentration and polymer type in shaping hydrophilic performance.

5.4 Biodegradable Test

Table IV: Biofilm Biodegradable Test (%) Data analysis

Sampel	Soil		
	W1	W2	Biofilm Biodegradable %
AG 15	0.62	0.26	58.06
AG 20	0.70	0.3	57.14
GG 15	0.78	null	0
GG 20	1	null	0
CG 15	0.93	0.58	37.63
CG 20	0.96	0.5	47.91
Sampel	**Sand**		
AG 15	0.73	0.3	58.9
AG 20	0.73	0.29	60.27
GG 15	0.78	null	0
GG 20	1.12	null	0
CG 15	0.68	null	0
CG 20	1.13	null	0

Fig. 2: Biodegradability Test Biofilm Before One Week in Soil and Sand

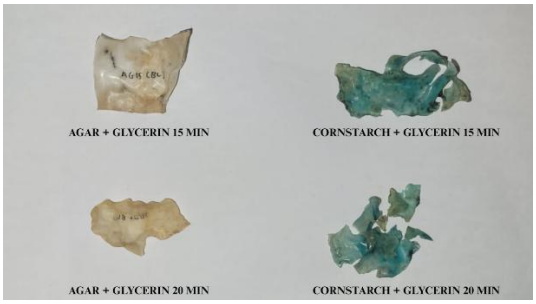

Fig. 3: Biodegradability Test Results of Biofilms Treated with Glycerin After One Week in Soil.

In soil, GG films showed complete decomposition within one week, indicated by "null" final weights, making them the most biodegradable. This high biodegradability is because gelatin is a protein-based matrix that is readily susceptible to rapid breakdown by the proteolytic microbial enzymes present in the soil AG films degraded moderately (58.06–57.14%) as a polysaccharide, agar is also biodegradable, but its gel-forming structure offers more structural integrity, leading to a slower degradation rate than the protein-based gelatin, while CG films showed lower biodegradability (37.63–47.91%), this lower performance is attributed to cornstarch's semi-crystalline nature. This arrangement and retrogradation possibility cause microbial enzymes to find it hard to penetrate the polymer chains and break them down, limiting access and resulting in the lowest rate of degradation. Visual observations (Figure 3) supported these findings, with AG films showing fragmentation and CG films retaining more structure, suggesting that exposure time of the film in the soil after one week

influences durability and microbial accessibility which can be seen in Fig. 3.

Fig. 4: Biodegradability Test Results of Biofilms Treated with Glycerin After One Week in Sand.

Under wet-sand conditions, GG and CG films again showed complete degradation, with "null" values indicating total breakdown rather than poor performance. AG films retained measurable residue but exhibited high biodegradability (58.9–60.27%), with more prolonged glycerine exposure accelerating deterioration (Figure 2). The saturated sand environment, rich in moisture from river water, likely enhanced microbial activity and enzymatic access, facilitating rapid decomposition. These results confirm that GG is highly suitable for applications requiring fast environmental breakdown, while AG offers stable yet effective biodegradability. CG's performance improves in moist conditions, suggesting its potential when paired with higher glycerine concentrations, as shown in Fig. 4.

It emphasizes the critical role of biofilm composition, glycerine concentration, and environmental moisture in determining biodegradation rates. Frequent rainfall and humid conditions during the soil test further accelerated microbial breakdown, especially for GG and CG films. These findings align with Gholamreza et al. (2021), highlighting how plasticizer integration and environmental factors shape biopolymer degradation and guide application-specific material selection.

5.5 Tensile Test

The mechanical performance of bioplastics formulated from agar (AG), gelatin (GG), and cornstarch (CG) with glycerin varies significantly due to differences in polymer structure and plasticizer interaction as shown in Table V.

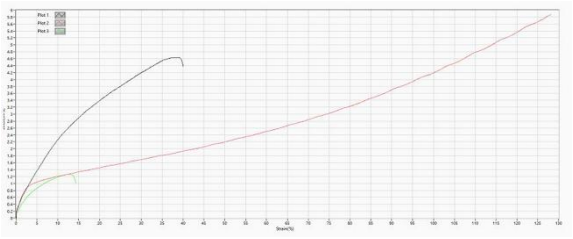

Fig. 5: Mechanical Performance Biofilm (Agar, Gelatin and Cornstarch) Boiling Point For 15 Minutes.

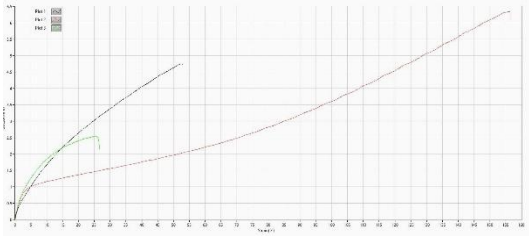

Fig. 6: Mechanical Performance Biofilm (Agar, Gelatin and Cornstarch) Boiling Point For 20 Minutes.

Fig. 7: Biofilm Before Tensile Test.

Fig. 8: Biofilm After Tensile Test.

Table V: Biofilm Tensile Test Data Analysis

Sampel	15 Minutes Boiling Point				
	Area (mm^2)	Peak Force (N)	T. Strength (MPa)	Elongation (%)	Yong's Modules (MPa)
AG 15	1.65	7.65	4.63	39.97	19.69
GG 15	2.55	14.96	5.87	128.13	2.85
CG 15	3.45	4.36	1.26	14.35	20.13
Sampel	**20 Minutes Boiling Point**				
AG 20	3.00	14.24	4.75	52.95	12.57
GG 20	5.40	34.24	6.34	156.45	2.64
CG 20	2.40	6.10	2.54	26.61	22.08

AG films demonstrated moderate tensile strength (4.63–4.75 MPa) and elongation (39.97–52.95%), balancing rigidity and flexibility. Agar's gel-forming polysaccharide backbone provides structural integrity, while glycerine disrupts intermolecular forces to reduce brittleness (Rusli, 2016).

GG films exhibited superior mechanical properties, with tensile strength ranging from 5.87 to 6.34 MPa and elongation from 128.13% to 156.45%, indicating high elasticity and softness. Gelatin's protein-based matrix, enhanced by glycerine, allows for excellent stretchability and moisture retention (Gholamreza, 2021). The low Young's modulus (2.85 MPa) confirms minimal stiffness, making GG ideal for cosmetic layers and flexible packaging.

In contrast, CG films showed the lowest tensile strength (1.26–2.54 MPa) and elongation (14.35–26.61%), with the highest stiffness (Young's modulus: 20.13–22.08 MPa), indicating brittleness and limited flexibility. Cornstarch's semi-crystalline nature resists plasticization, and glycerine alone cannot soften its matrix (Harussani et al., 2021). Overall, GG offers the best mechanical profile, AG provides moderate versatility, and CG suits rigid applications. These results underscore the need for tailored formulations to meet specific bioplastic performance demands.

5 CONCLUSION

This study demonstrates the potential of agar, gelatine, and cornstarch as biodegradable biofilm bases when plasticized with glycerine. Gelatine films exhibit superior mechanical strength and complete biodegradability, making them ideal for flexible, fast-degrading applications. Agar films offered balanced solubility and tensile properties, suitable for edible and semi-rigid packaging. Cornstarch films, while naturally biodegradable, showed limited flexibility and solubility, which is best suited for rigid disposables. The boiling duration influenced moisture content, water absorption, and surface morphology, highlighting the importance of thermal processing. These findings emphasise that polymer selection and glycerine integration are key to tailoring biofilms for sustainable packaging and environmental applications.

ACKNOWLEDGEMENTS

I would like to express sincere gratitude to Prof. Madya Ts. Dr Sitti Fatimah Binti Mhd Ramle for her invaluable guidance, support, and encouragement throughout this research. Her expertise and dedication greatly contributed to the development and refinement of this work. Appreciation is also extended to everyone who offered insight and assistance during this journey.

REFERENCES

Madarina, Amira, et al. "Effect of Glycerin as a Plasticizer on Flexural Strength in the Fabrication of Gypsum-Based Chip." *F1000Research*, vol. 12, 13 Nov. 2023, pp. 1460–1460, https://doi.org/10.12688/f1000research.139416.1.

Abotbina, Walid, et al. "Development and Characterization of Cornstarch-Based Bioplastics Packaging Film Using a Combination of Different Plasticizers." *Polymers (20734360)*, vol. 13, no. 20, 15 Oct. 2021, pp. 3487–3487, web.a.ebscohost.com/ehost/pdfviewer/pdfviewer?vid=1&sid=dab174a6-9f78-468a-85ab-0541ce4e13d0%40sdc-v-sessmgr02, https://doi.org/10.3390/polym13203487.

Patel, Jatin, et al. "Issue 3 Www.jetir.org (ISSN-2349-5162)." *JETIR1903D56 Journal of Emerging Technologies and Innovative Research*, vol. 6, 2019, www.jetir.org/papers/JETIR1903D56.pdf.

Fathiraja, Parthiban, et al. "Process Optimization and Characterization of Composite Biopolymer Films Obtained from Fish Scale Gelatin, Agar and Chitosan Using Response Surface Methodology." *Polymer Bulletin*, 20 Nov. 2022, https://doi.org/10.1007/s00289-022-04540-4.

Rusli, Arham, et al. "(PDF) Physical and Mechanical Properties of Agar- Based Edible Film with Glycerol Plasticiser." *ResearchGate*, 2016, www.researchgate.net/publication/305410349_Physical_and_mechanical_properties_of_agar_based_edible_film_with_glycerol_plasticizer.

Muñoz-Almagro, Nerea, et al. "Effect of sucrose substitution with stevia and saccharin on rheological properties of gels from sunflower pectins." *Elsevier.com*, 2025, linkinghub.elsevier.com/retrieve/pii/S0268005X2100326X.

Patel, Jatin, et al. "Agar-Agar Bioplastic Synthesis and Its Characterization." *JETIR1903D56 Journal of Emerging Technologies and Innovative Research*, vol. 6, no. ISSN-2349-5162, 2019, www.jetir.org/papers/JETIR1903D56.pdf.

Palanisamy, Chella Perumal, et al. "A Comprehensive Review on Corn Starch-Based Nanomaterials: Properties, Simulations, and Applications." *Polymers*, vol. 12, no. 9, 22 Sept. 2020, p. 2161, www.mdpi.com/2073-4360/12/9/2161/pdf#:~:text=Basic%20corn%20starches%20have%20a, https://doi.org/10.3390/polym12092161.

Procházková, Petra, et al. "Effects of Biodegradable P3HB on the Specific Growth Rate, Root Length and Chlorophyll Content of Duckweed, Lemna Minor." *Heliyon*, vol. 9, no. 12, 1 Dec. 2023, p. e23128, pubmed.ncbi.nlm.nih.gov/38076089/, https://doi.org/10.1016/j.heliyon.2023.e23128.

Saygin, Hasan, and Asli Baysal. "Biofilm Formation of Clinically Important Bacteria on Bio-Based and Conventional Micro/Submicron-Sized Plastics." *Bulletin of Environmental Contamination and Toxicology*, vol. 105, no. 1, 14 May 2020, pp. 18–25, https://doi.org/10.1007/s00128-020-02876-z.

Mirghani, Ruba, et al. "Biofilms: Formation, Drug Resistance and Alternatives to Conventional Approaches." *AIMS Microbiology*, vol. 8, no. 3, 2022, pp. 239–277, pmc.ncbi.nlm.nih.gov/articles/PMC9576500/, https://doi.org/10.3934/microbiol.2022019.

Favour Olaoye, Sabir Kashar. "Development of biodegradable polymers: exploring eco-friendly alternatives for packaging in the food industry." *Plasmas and Polymers*, 11 Dec. 2024,

www.researchgate.net/publication/386874653_development_of_biodegradable_polymers_exploring_eco-friendly_alternatives_for_packaging_in_the_food_industry.

Harussani, M. M., et al. "Determination of the Tensile Properties and Biodegradability of Cornstarch-Based Biopolymers Plasticized with Sorbitol and Glycerol." *Polymers*, vol. 13, no. 21, 27 Oct. 2021, p. 3709, mdpi-res.com/d_attachment/polymers/polymers-13-03709/article_deploy/polymers-13-03709.pdf, https://doi.org/10.3390/polym13213709.

Hernández, Valentina, et al. "Agar Biopolymer Films for Biodegradable Packaging: A Reference Dataset for Exploring the Limits of Mechanical Performance." *Materials*, vol. 15, no. 11, 1 Jan. 2022, p. 3954, www.mdpi.com/1996-1944/15/11/3954, https://doi.org/10.3390/ma15113954.

Kamar Shayah, et al. "Comparison of Different Materials Used in the Preparation of Household Bioplastics and Evaluation of a Mixture of Animal Gelatin and Cornstarch." *Syrian Journal for Science and Innovation*,Volume 3, No. Issue 1 - Volume 3, 23 Jan. 2025, journal.hcsr.gov.sy/archives/1506.

Neelam, Asia, and Omm-e-Hany. "A Study of the Thermal and Mechanical Properties of Gelatin-Based Bioplastics." *Book Publisher International (a Part of sciencedomain International)*, 28 Oct. 2022, pp. 57–69, https://doi.org/10.9734/bpi/cagees/v7/3787e.

Marzieh Bakeshlouy Afshar, et al. "Introducing Graphene Quantum Dots in Decomposable Wheat Starch-Gelatin Based Nano-Biofilms." *Scientific Reports*, vol. 14, no. 1, 24 Jan. 2024, https://doi.org/10.1038/s41598-024-52560-z.

Lee, Cindy Li Yin, and Wan Sieng Yeo. "A Basic Characterisation Study of Bioplastics via Gelatinization of Corn Starch." *Journal of Applied Science & Process Engineering*, vol. 8, no. 2, 31 Oct. 2021, pp. 820–833, https://doi.org/10.33736/jaspe.3445.2021.

Alipal, J. "A Review of Gelatin: Properties, Sources, Process, Applications, and Commercialisation." *Materials Today: Proceedings*, vol. 42, no. 1, 1 Jan. 2021, pp. 240–250, www.sciencedirect.com/science/article/pii/S2214785320406406, https://doi.org/10.1016/j.matpr.2020.12.922.

Tabassum, Asma. "Biofilms from Agar Obtained from an Agarophyte of Karachi Coast." *Biofilms from Agar Obtained from an Agarophyte of Karachi Coast*, vol. 25, no. 1&2, 25 Dec. 2016, www.researchgate.net/publication/324888685_biofilms_from_agar_obtained_from_an_agarophyte_of_karachi_coast.

Enhancing Microstrip Patch Antenna Performance via Magnesium Tailoring of Ni-Zn Ferrites Structure

Nurul Ainaa Najihah **Busra**[1], Rodziah **Nazlan**[1*], Mohamad Ashry **Jusoh**[1]

[1] Faculty of Industrial Sciences and Technology,
Universiti Malaysia Pahang Al-Sultan Abdullah
Lebuh Persiaran Tun Khalil Yaakob 26300, Kuantan,
Pahang, Malaysia

*Corresponding author's phone: +609-4315627
E-mail: rodziah@umpsa.edu.my

Received: 28 October 2025; Accepted: 8 January 2026

ABSTRACT

Microstrip patch antennas (MPAs) are favored for their compactness and ease of integration, especially in wireless communication. Incorporating nickel zinc ferrites (NZF) as the radiating patch enhances the MPA performance by improving both bandwidth and return loss. However, optimizing the NZF properties is challenging, particularly through the introduction of Mg dopants, which can further enhance the performance of MPAs. Mg-NZF with Mg = 0.0 to 0.6 concentrations were synthesized using the mechanochemical technique. The effect of Mg variations on the NZF was characterized by their structural, microstructural and magnetic properties. The performance of the Mg-NZF as a radiating patch in MPA was evaluated through return loss and bandwidth measurement in the X-band frequency. XRD analysis confirms a single-phase spinel structure regardless of Mg concentrations, with a slight lattice parameter ranging from 8.3818 to 8.4010 Å attributed to Mg incorporation. Two main bands near 569.42 cm^{-1} and 425.66 cm^{-1} correspond to intrinsic vibrations of tetrahedral and octahedral Fe^{3+}–O^{2-} complexes. EM measurements show that MPA with Mg = 0.4 achieved the highest negative return loss of -37.98 dB at a resonant frequency of 7.95 GHz and a bandwidth of 1.12 GHz. Mg substitution improved the saturation magnetization (62.07 emu/g at x = 0.4), which enhanced impedance matching and radiation efficiency, leading to the highest return loss (-37.98 dB) and bandwidth (BW) (1.12 GHz) at 7.95 GHz. This increase in M_s correlates with improved superexchange interactions between magnetic moments. The combination of NZF and Mg leads to significant improvements in the microstructure and magnetic properties, facilitating better tuning and efficiency in the MPA performance.

Keywords— microstrip patch antenna, nickel zinc ferrites, magnesium dopant, magnetic properties, return loss optimization

1.0 INTRODUCTION

Undoubtedly, one of the most significant technologies nowadays is wireless communication technology because it enables communication without physical cables, allowing people to connect regardless of location. In addition, it also offers lower infrastructure costs and integrates a broad range of services and applications to meet the needs of users [1]. The rapid development of wireless communication technologies in the last decade has led to a new age of connectivity, driven largely by the advancements in 5G network. Antenna plays a central role as a critical interface between radar and wireless communication systems and the external environment. It transmits and receives radio frequency signals across

diverse applications without noticeable interruptions or disruptions [2]. In order to accommodate the latest and most advanced technology, several electrical and microwave equipment are being updated daily in terms of both model and features. The evolution of wireless device models and trends, as well as the modifications of antennas, are all comparatively significant. The effectiveness of these systems is heavily influenced by the design and placement of antennas, as improper installation or positioning often leads to poor performance [3].

In modern microwave and wireless engineering, the growing demand for compact antenna systems has made antenna miniaturization become a significant research focus. Among the various antenna structures, microstrip patch antennas (MPAs) have gained a lot of attention because of their compact profile. In fact, MPA also considered as the modest form of the antenna arrangement which used the microstrip technique for fabrication purpose to keep the antenna size small and can be simply mounted on a circuit board [4]. Despite its compact size, MPA also offered distinct characteristics such as, low cost, light weight, low profile and patching in various geometric shapes.[5].

The strong and growing demand for antennas that can operate efficiently at high frequencies is driven by the need for higher data rates, wider bandwidth, and improved resolution in modern systems, and this demand has been increasing across several fields, including satellite systems, radar systems and Internet of Things (IoT). However, there are still a great deal of problems and limitations that must be dealt with; the narrow bandwidth and the efficiency of the radiation will be poor due to the small size of the antenna, leading to degradation in antenna performance. In the early development of antennas, metal was chosen as a radiating element because of its high conductivity and to maximise the radiation efficiency. While traditional materials offer stability, they may face limitations. Their inherently narrow frequency bandwidth makes them only effectively operate within a limited range of frequencies [6]. Besides, due to the intrinsic characteristics of metal, the traditional metal-based antennas are corroded easily, causing economic losses and degrading performance and lifespan. Several methods have been employed such as radome, sacrificial anodes protection and alloys with corrosion-resistance in order to reduce the corrosion of antenna. However, these approaches are often costly to implement and reduce metal conductivity, hence negatively impacting radiation efficiency [7].

Thus,it was necessary to investigate radiating patch materials with improved performance characteristics. To address these limitations, ferrite-based MPA is proposed as an alternative to the conventional metallic layer in the antenna patch. The study analyzes how Mg substitution in nickel zinc ferrite modifies the structural and magnetic properties of the material and evaluates the resulting impact on impedance matching and bandwidth enhancement in MPAs. The MPA design was developed for X-band applications due to this frequency range is relevant especially for satellite communication, Internet of Things (IoT) systems, and defense radar, where compact size, stable radiation characteristics, and reliable high-frequency performance are essential.

2.0 THEORY/LITERATURE REVIEW

Ferrite-based materials provide a low cost and stable alternative for patch fabrication [8].Spinel-type ferrite has increased tremendous interest among researchers due to its excellent magnetic and dielectric performance, along with its physical and chemical stability. Within the subclass of ferrites, Ni–Zn ferrites are considered the most adaptable ferrites as a result of their novel characteristics that make them ideal for high-frequency applications [9]. Ni-Zn ferrites are widely

utilized as core materials in numerous electromagnetic devices and extensive industrial applications, including inductors, microwave components, power supplies, transformers for both high and low frequencies and antenna rods [10]. These wide range of applications are owing to their high saturation magnetization, high magnetic permeability, good chemical stability, exceptional mechanical strength, high curie temperature (570 °C) and low losses [11]. Moreover, the high resistivity (10^6 Ω cm) of Ni-Zn ferrite make them a good candidate to be used in high frequency antennas in order to minimal the eddy current losses [12]. Beyond its excellent properties, Ni-Zn ferrites also offer great potential for enhancement due to their adaptable valence state, distinctive electronic configuration, and flexible structure, hence providing numerous opportunities for improvement [13]. Zhang [14] reported the $MgZnFe_2O_4$ have large magnetization values compared to $ZnFe_2O_4$, which basically approaches zero. Navneet *et al*. [15] discussed the magnetic moment measurements due to the incorporation of Mg in Ni–Zn spinel ferrites. The saturation magnetization first increases and then decreases with an increase in the concentration of Mg^{2+} ions. The values of coercivity decrease with an increase in Mg^{2+} concentration. With this motivation, it is expected that an appropriate amount of Mg^{2+} substitution can modify the overall ferrite structure, enhancing the permeability and magnetization of the sample, thereby achieving better impedance matching. Improved impedance matching will lead to superior antenna performance by reducing return loss, allowing the antenna to transmit signals more efficiently and at maximum strength.

3.0 MATERIALS

For the synthesis; Iron (III) oxide (Fe_2O_3) (96 %), Nickel (II) oxide (NiO) (99 %), Zinc oxide (ZnO) (99 %), Magnesium oxide (MgO) (99 %), α-terpineol (90 %), m-xylene (99 %) and linseed oil were procured from Sigma-Aldrich. All the chemicals and materials were used without further purification.

4.0 EXPERIMENTAL

4.1 Synthesis of Mg-NZF

Ferrite powders Mg-NZF, with the general formula $Ni_{0.3}Zn_{0.7-x}Mg_xFe_2O_4$ (x = 0.0, 0.2, 0.4 and 0.6) were synthesized using the mechanochemical technique [16]. Stoichiometric quantities of iron oxide, nickel oxide, zinc oxide and magnesium oxide that have been calculated with mol percentages were milled for 6 hours using a Cole-Palmer BM-450 SPEX equipped with a hardened steel vials and balls. The steel vial and grinding balls were used, and the ball-to-powder weights ratio of (BPR) 10:1. The milling was performed at 1450 rotation per minute (rpm) at room temperature in a deionized water medium. The obtained mixture was dried in the oven at 80 °C for 12 hours and then calcined at 800 °C for 2 hours in an air atmosphere. The calcined powders were milled again at 1450 rpm rotation speed for a milling time of 1 hour. The dry powders were granulated with 2 wt% PVA (Polyvinyl Alcohol) binder and pressed into toroidal shaped at a pressure of 5 tonnes. Subsequently, samples in powder and toroidal forms were underwent the conventional final-stage sintering process at 1200 °C for a duration of 8 hours in air, with a heating rate of 4 °C per minute.

4.2 Fabrication of Mg-NZF based patch antenna

The basic configuration of MPA generally consist of ground plane, dielectric substrate, radiating patch and feeding part. The ground plane is the lowest layer is often made of material that conducts electricity, whereas the substrate which is intermediate layer is most commonly from the material which has dielectric constant ε_r in the range of 2.2 to 12. The radiating patch is positioned on the top layer in antenna configuration and a microstrip feedline is

positioned centrally along the width of the rectangular patch and etched on the same substrate layer. The patch antenna is wider than the feed line. The feed dimensions are selected to provide an impedance close to 50 ohms, which enables impedance matching between the feed and the patch antenna. [17]. With proper matching, energy is coupled more efficiently to the patch, resulting in better antenna performance. MPA was fabricated using a screen-printing technique. The screen printing technique was chosen over 3D printing because it is low cost, high material utilization and suitability for large area mass production [18]. This technique offers ease of operation and provides superior compatibility that can be used for large scale production on different substrates, including fabrics and polymers [19]. The organic binder was firstly prepared by mixing 85.0 wt% linseed oil with 12.5 wt% m-xylene using magnetic stirrer at 250 rpm for 3 hours. Then, 2.5 wt% α-terpineol was added to the mix and then continued stirring for another 2 hours [20]. The prepared binder was added to the sample powder with different powder to binder weight ratios and mixed using a vortex mixer for 30 minutes to obtain a homogenous paste for thick film printing. The FR4 substrate was selected due to its low cost [21] and high mechanical strength [22]. The prepared thick film paste was printed screen printed onto the FR4 substrate using a silk-screen frame and squeegee, then underwent dried and fired at 200 °C for 30 minutes to ensure adhesion of the thick film paste onto the substrate. A subMiniature connector is then adhered to the patch antenna by using silver paste and copper tape for further measurement. The schematic diagram of the fabricated MPA and its specifications are given in Fig. 1 and Table 1, respectively.

4.3 Characterization

The structure of the sintered sample was measured by using Rigaku Miniflex II X-ray Diffractometer. Images of their microstructure were obtained using a scanning electron microscope (SEM, JEOL JSM-IT200). The Fourier transmission infrared (FTIR) measurements in the studied samples were carried out (contained within a KBr matrix) by Perkin Elmer Spectrum 100 Spectrometer in a region of wave number from 400–4000 cm^{-1} to determine the functional groups and bonds in all materials. Magnetic hysteresis loops were measured by using a vibrating sample magnetometer (VSM, Lake Shore 7410). The performances of the microstrip patch antenna were measured with return loss analysis using PNA N5227A Vector Network Analyzer.

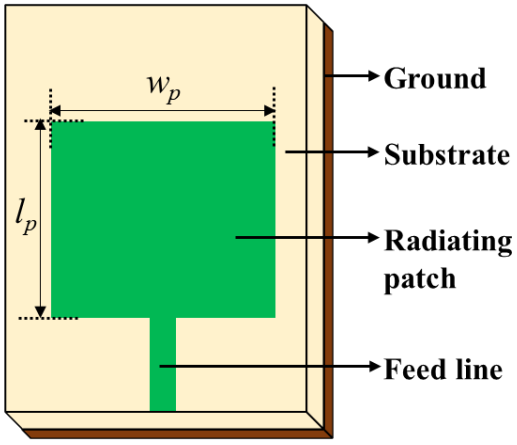

Fig. 1 Configuration of a rectangular MPA.

TABLE 1: Specifications of patch antenna

Parameter	Value
Dielectric constant, ε_r	4.3
Substrate thickness, h	1.6 mm
Patch width, w_p	15 mm
Patch length, l_p	11 mm

5.0 RESULTS AND DISCUSSION

5.1 XRD Analysis

Fig.2 shows the multi-plot of X-ray diffraction spectra of the sintered $Ni_{0.3}Zn_{0.7-x}Mg_xFe_2O_4$ (x = 0.0, 0.2, 0.4 and 0.6) samples at 1200 °C. The diffraction patterns are listed to (220), (311), (222), (400), (422), (333), (440), (620), (533) and (622) reflection planes, accordingly at 2θ values of 30.06°, 35.40°, 37.03°, 43.022°, 53.37°, 56.97°, 62.56°, 70.98°, 74.01° and 75.02°. The diffraction peaks found are

notable because they closely corresponding to the standard crystallographic phase as mentioned in reference code 98-006-8765 and also to those found in earlier research on spinel ferrites [21, 22]. The most intense (311) plane confirms the formation of a single-phase face centred cubic spinel. The samples do not exhibit any significant changes in peak position or additional impurity phase, which suggests that the Mg^{2+} is completely incorporated in the host nickel zinc ferrite lattice [25]. The *d* spacing, lattice constant and unit cell volume were calculated using the most prominent peaks (311) in each sample, as shown in Table 2. The lattice constant, *a* was determined via the following formula [26]:

$$a = d\sqrt{h^2 + k^2 + l^2} \quad (1)$$

where *d* is the interplanar spacing and *hkl* are the Miller indices of the lattice planes. The lattice constant for the (311) peaks of Mg-substituted NiZn ferrites as shown in Table 1, initially increased from 8.3891 Å to 8.3950 Å at (x = 0.2), then decrease in value of lattice parameters 8.3818 Å at (x = 0.4) and later increased to 8.4010 at (x =0.6) with increased concentration of Mg. The resultant variation in lattice parameter does not appear to be a simple linear function. Based on the fact that the radius of Mg^{2+} ions (0.72 Å) has a smaller ionic radius compared to that of Zn^{2+} ions (0.74 Å). The lattice parameter was expected to decrease with increasing magnesium substitution, following Vegard's law However, deviations from Vegard's law may occur due to the preferential occupation of Mg^{2+} ions at both tetrahedral and octahedral sites, which modifies the local lattice strain [27].

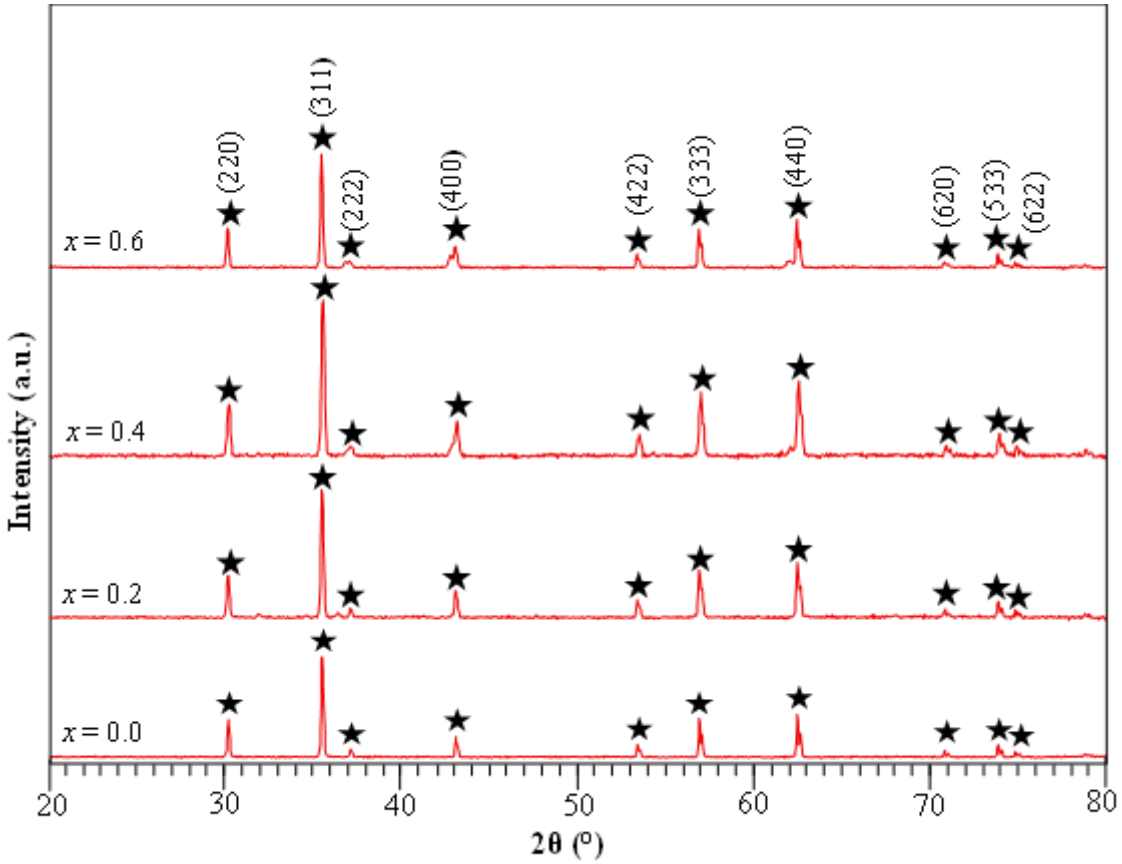

Fig.2: X-ray diffraction patterns for $Ni_{0.3}Zn_{0.7-x}Mg_xFe_2O_4$ (x = 0.0 to 0.6).

TABLE 2: Structural parameters based on XRD spectra for Mg substituted NZF

Mg concentration, *x*	Peak position (°)	Most intense phase	Space group	(hkl)	d-spacing	a (Å)
0.0	35.4915	$NiZnFe_2O_4$	Fd3m	311	2.52938	8.3891
0.2	35.4658	$MgNiZnFe_2O_4$	Fd3m	311	2.53115	8.3950
0.4	35.5228	$MgNiZnFe_2O_4$	Fd3m	311	2.52722	8.3818
0.6	35.4388	$MgNiZnFe_2O_4$	Fd3m	311	2.53302	8.4010

Vegard's law However, deviations from Vegard's law may occur due to the preferential occupation of Mg^{2+} ions at both tetrahedral and octahedral sites, which modifies the local lattice strain [27].

5.2 SEM Analysis

Scanning electron microscopy (SEM) was utilized to examine the microstructure and morphology of ferrites. Fig. 3 shows SEM image captured at 7000 x magnification with a 2 µm observation range, alongside histograms illustrating the particle size distribution. The magnesium concentration in Ni-Zn ferrites was found to significantly affect the particle size and structural shape. From the micrographs, it is obvious that the samples exhibit mostly polygonal shapes with flat and faceted faces. There are no obvious large pores or necks between grains, indicating sintering has progressed beyond initial neck formation and particle rearrangement. The microstructure seems uniform and dense, typical of a material after high temperature sintering where grain growth and densification are dominant. Moreover, the randomly selected 200 particles from the SEM images were represented as whole particles to measure the particle size distributions by using a J-image software. The effect of Mg^{2+} ion towards the particle size distribution can be observed in histograms in Fig 3. The average particle sizes of samples of obtained have ranges between 2.33 µm to 3.33 µm as Mg content increased from x = 0.0 to 0.4. As reported by [28], Mg acts as a sintering aid by promoting grain growth and enhancing densification. This aligns with the observed increase in particle size with higher Mg content and the microstructural evolution in the samples.

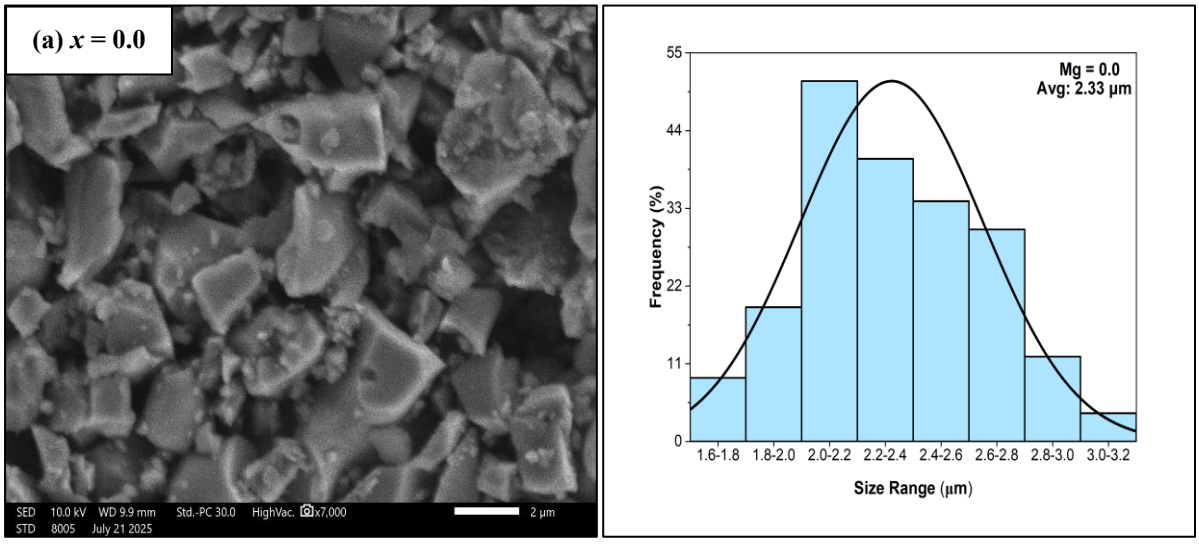

Fig.3: Continued

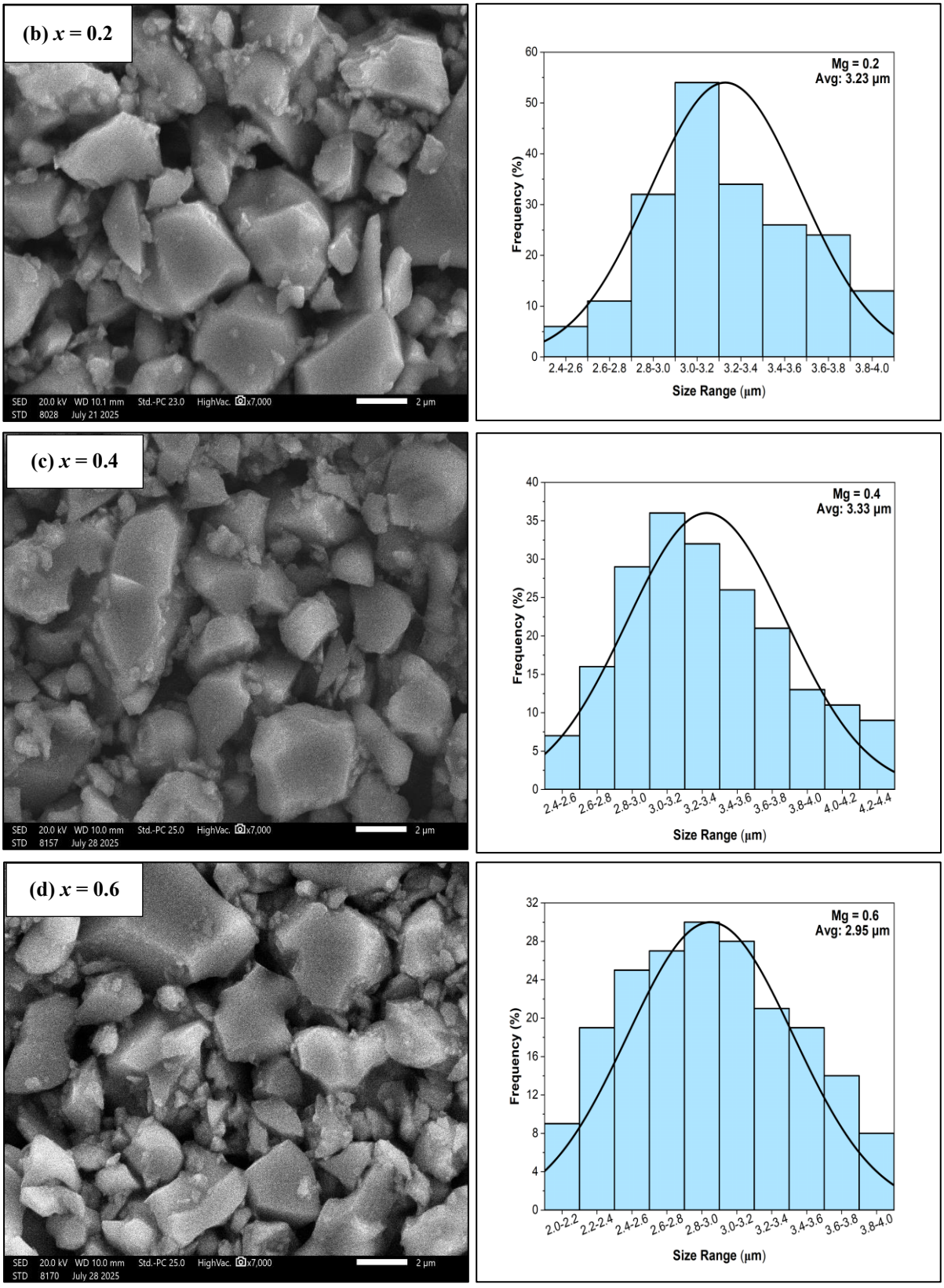

Fig.3: SEM micrographs under magnification of 7000× with corresponding histograms of particle size distribution of $Ni_{0.3}Zn_{0.7-x}Mg_xFe_2O_4$ samples sintered at 1200 °C.

5.3 FTIR Analysis

The analysis of chemical bonding of the sintered $Ni_{0.3}Zn_{0.7-x}Mg_xFe_2O_4$ samples has been carried out by using Fourier transform infrared spectroscopy (FTIR) [29]. Fig 4. shows the spectrum measured in the region of 4000-400 cm^{-1}. The FTIR spectra of all examined powder series exhibit two prominent absorption bands, v_1 (about 570 cm^{-1}) and v_2 (about 429 cm^{-1}) in the range of 400-600 cm^{-1}. These two absorption bands are defined as [23]:

$$v = \frac{1}{2\pi c}\sqrt{\frac{k}{\mu}} \qquad (2)$$

where v is the wavenumber, c is the speed of light, k is the force constant and μ represents the reduced mass of ions. The observed absorption band reveals the formation of a single phase spinel structure [30]. The absorption band at 569.42 cm^{-1} and 425.66 cm^{-1} is attributed to the intrinsic stretching vibration of Fe^{3+}–O^{2-} in tetrahedral and octahedral site respectively [31]. The v_2 band shifts shifts towards higher wavenumber side with increasing Mg^{2+} content, indicating reduced Fe-O bond length due to site substitution. This can be attributed to the fact that Mg^{2+} ions might be occupying the octahedral sites. As Mg^{2+} ions (0.72Å) have a larger ionic radius than Fe^{3+} ions (0.55Å), they push the Fe^{3+} ions towards oxygen ion resulting in decreased Fe^{3+}-O^{2-} bond length. Hence, the shorter the bond length corresponds to the stronger bond (larger k) which in turn may be responsible for the increase the fundamental frequency of vibration of the tetrahedral site [15]. In addition, an increase in force constants (k), reflects the stronger of bonding within the crystal lattice, particularly between the cations and oxygen ions [31]. The peaks present at 1380.53 cm^{-1} and 1622.66 cm^{-1} are attributed to carboxyl group (COO^-) and stretching of C-H bonds respectively. While the broad peaks at 3413.61 cm^{-1} were linked with stretching vibration of the O-H group in the samples [32].

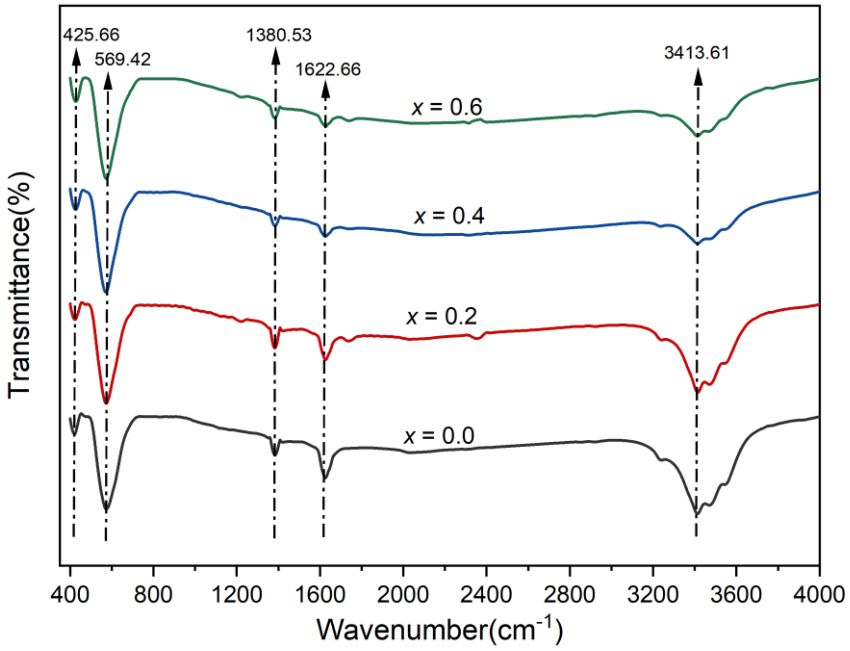

Fig 4: FTIR spectra of $Ni_{0.3}Zn_{0.7-x}Mg_xFe_2O_4$ (x = 0.0, 0.2, 0.4 and 0.6)

5.4 Magnetic Properties

The magnetic nature of the prepared Mg-NZF samples was analyzed using vibrating sample magnetometer (VSM) by applying a maximum magnetic field (±12 kOe) which indicates that the samples exhibited magnetic behavior. The room temperature of magnetization (M) versus magnetic field (H) curves (hysteresis loop) of prepared samples are displayed in Fig 5. The narrow breadth (S-shaped) of the hysteresis curve and small H_c values signify that this sample is a type of soft ferrite, which can be easily magnetized and demagnetized under low applied magnetic field [33]. Table 3 shows the quantitative results of saturation magnetization (M_s) and coercivity (H_c), which were determined to be in the range of (47.46–62.07) emu/g and (34.51–38.37) Oe respectively. Generally, magnetization increases as the applied magnetic field is raised, until it reaches a saturation point at higher fields where all magnetic moments are fully aligned. Beyond this saturation, increasing the magnetic field does not significantly increase the magnetization, as the material attains its maximum magnetic response. It was found that the saturation magnetization (M_s) increases up to 62.07 emu/g at a Mg concentration of $x = 0.4$. As the concentration is increased further to $x = 0.6$, the saturation magnetization value decreases to 54.32 emu/g. In Ni-Zn ferrites system, Zn^{2+} ions strongly prefer to occupy the tetrahedral (A) sites, while Ni^{2+} and Mg^{2+} ions mainly occupy the octahedral (B) sites. Fe^{3+} ions have an equal tendency to be distributed between both A and B sites. The saturation magnetization is influenced by the distribution of Fe^{3+} ions among the tetrahedral (A) and octahedral sites (B) [23]. By increasing the concentration of Mg^{2+} (0 μB) ions displace the Fe^{3+} (5 μB) ions from the A site to B site, eventually will enhances A-B super exchange effect and results in an increased value of M_s. Despite of cation distribution, the increased of grain size at $x = 0.4$ facilitated magnetic domain alignment, resulting in the highest magnetization (62.07 emu/g).

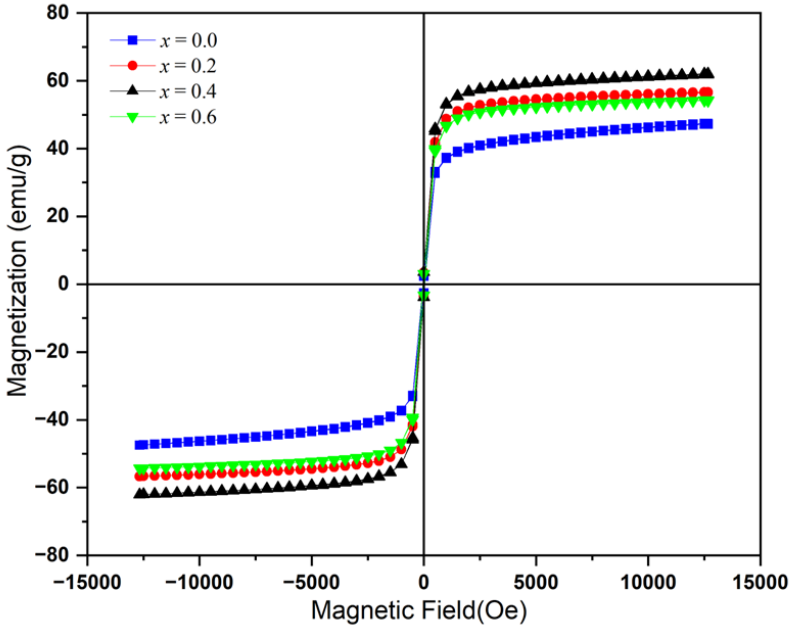

Fig 5: Magnetic hysteresis loop of $Ni_{0.3}Zn_{0.7-x}Mg_xFe_2O_4$ ($x = 0.0$, 0.2, 0.4 and 0.6)

TABLE 3: Variation of magnetic parameters with different Mg concentrations

Mg concentration, x	Saturation Magnetization, M_s (emu/g)	Remanence Magnetization, M_r (emu/g)	Coercivity, H_c (Oe)
0.0	47.46	2.43	34.51
0.2	56.70	3.44	38.37
0.4	62.07	3.73	38.06
0.6	54.32	3.18	37.42

5.5 Return Loss

The performance of an antenna depends on several performance metrics such as S-parameter (S_{11}) and bandwidth. The variations of return loss (RL) as a function of frequency of silver patch and Mg substituted NZF is depicted in Fig. 6. The values of RL at corresponding operating frequency and -10 dB bandwidth are tabulated in the Table 4. The RL indicates that how perform an antenna could transfer power from a source to the antenna [34]. From Fig. 6, it could be observed that, the silver sample exhibited a lowest negative return loss of -19.35 dB, indicating relatively poor impedance matching. Increasing concentration of magnesium from 0.0 to 0.4 significantly enhances the microwave absorption properties of the samples, which demonstrates a substantial increment of negative RL of the samples starting from -33.17 dB to -37.98 dB. It can be seen that each material has a strong ability to absorb microwaves. The antenna at $x = 0.4$ exhibits the highest negative return loss (-37.98 dB), which align with the output from SEM and saturation magnetization. The magnesium concentration in NZF was found to significantly influence the particle size and structural morphology. The increase in particle size may enhance the relative permeability, which in turn contributes to an increase in the net magnetic moment and consequently higher M_s. This improvement facilitates better impedance matching between the patch and the feed line. As a result, more efficient power transfer is achieved, leading to the observed higher negative RL. The measured bandwidths for

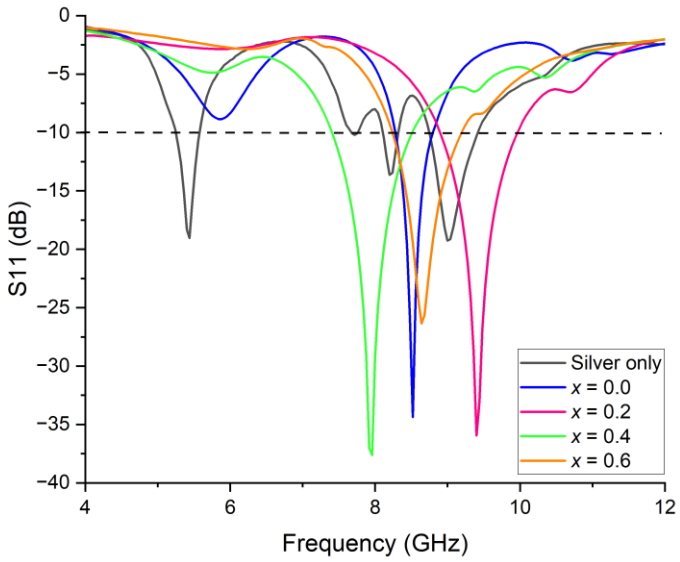

Fig 6: Return loss (S11) characteristics of $Ni_{0.3}Zn_{0.7-x}Mg_xFe_2O_4$ based MPAs; the –10 dB reference is shown by the dotted line

TABLE 4: Outcomes of the proposed MPA

Mg concentration, *x*	Frequency (GHz)	Return Loss (dB)	Effective Bandwidth at -10dB (GHz)
silver	9.02	-19.35	0.67
0.0	8.50	-33.17	0.49
0.2	9.42	-36.03	1.07
0.4	7.95	-37.98	1.12
0.6	8.65	-26.49	0.94

all samples are in the range of 0.49-1.12 GHz. The bandwidth was defined as the difference between the highest and lowest frequencies in a continuous band of frequencies. The bandwidth of the of Mg substituted NZF based patch antenna was measured at -10 dB, which meets the accepted antenna design standard as it indicates that the antenna reflects only 10% of the power while radiating at least 90% effectively [35]. The overall observations about the return loss and -10 dB % bandwidth, it is inferred that the x = 0.4 ferrite has potential to be used as a radiating patch for microstrip patch antenna.

6.0 CONCLUSION

This study concludes that magnesium substitute nickel zinc ferrite shows promising potential for developing microstrip patch antennas used in microwave antenna and wireless communication technologies. Conducting an in-depth investigation of Mg substituted NZF paste synthesized using the mechanochemical technique including examination of phase, functional groups, and morphology together with the magnetic nature of Mg substituted NZF shows the impact of substitution of magnesium in nickel zinc ferrite system. The optimal magnesium content at x = 0.4 resulted in a saturation magnetization of 62.07 emu/g, a return loss of –37.98 dB, and a bandwidth of 1.12 GHz, demonstrating a strong correlation between magnetic enhancement and antenna performance. These results highlight Mg substituted NZF as a potential ferrite material for improving patch antenna performance.

ACKNOWLEDGEMENTS

The authors gratefully acknowledge Universiti Malaysia Pahang Al-Sultan Abdullah (UMPSA) for their financial support under the Post-Graduate Research Scheme (PGRS230368). Appreciation is also extended to the Ministry of Higher Education for funding provided through the Fundamental Research Grant Scheme No. FRGS/1/2021/TK0/UMP/02/54 (University Reference RDU210152), which made this research possible.

REFERENCES

1. N. M. Sayem, A. K. M. Baki, F. Faysal, S. T. Mahmud, A. Jubayer, and T. A. Rifat, “Development of Novel and High Gain Microstrip Patch Antennas at Different Frequency Bands for 6G Applications,” Progress In Electromagnetics Research, vol. 137, pp. 263–275, 2023.
2. M. S. Rana et al., “At 28 GHz microstrip patch antenna for wireless applications: a review,” Telkomnika (Telecommunication Computing Electronics and Control, vol. 22, no. 2, pp. 251–262, 2024.
3. V K. Garg, “Chapter 10 Antennas, Diversity, and Link Analysis,” in Wireless Communications & Networking, pp. 287–316, 2007.
4. M. T. Islam et al., In: Proceedings of Second International Conference on Recent Advances in Materials and Manufacturing 2020, pp. 1502–1505.

5. S. K. Ezzulddin, S. O. Hasan, and M.M. Ameen, “Microstrip patch antenna design, simulation and fabrication for 5G applications,” Simul. Model. Pract. Theory, vol. 116, no. January, 2022.
6. S. Siragam, “Nanocomposite marvels: Miniaturized high bandwidth microstrip patch antenna for X-band applications,” Next Mater, vol. 5, no. July 2023, pp. 100243, 2024.
7. Y. Hui et al., “Graphene-Assembled Film-Based Reconfigurable Filtering Antenna with Enhanced Corrosion-Resistance,” Crystals, vol. 13, no. 5, 2023.
8. M. Zain Ul Abidin, M. Ikram, S. Moeen, G. Nazir, M. B. Kanoun, and S. Goumri-Said, “A comprehensive review on the synthesis of ferrite nanomaterials via bottom-up and top-down approaches advantages, disadvantages, characterizations and computational insights,” Coord. Chem. Rev, vol. 520, 2024.
9. Q. Yu, Y. Su, R. Tursun, and J. Zhang, “Synthesis and characterization of low density porous nickel zinc ferrites,” RSC Adv, vol. 9, no. 23, pp. 13173–13181, 2019.
10. H. Singh et al., “Ultrasonically assisted solvohydrothermal synthesis of nanocrystalline Zn-Ni ferrite advanced material for EMI shielding,” J. Alloys Compd, vol. 906, p. 164199, 2022.
11. R. Dosoudil, M. Soka, M. Usakova, E. Usak, V. Jancarik, and E. Dobrocka, “Magnetic and Structural Properties Analysis of Cerium Substituted Nickel-Zinc Ferrites,” IEEE Transactions on Magnetics, vol. 58, no. 2. 2022.
12. J. S. Ghodake, R. C. Kambale, T. J. Shinde, P. K. Maskar, and S. S. Suryavanshi, “Magnetic and microwave absorbing properties of Co^{2+} substituted nickel-zinc ferrites with the emphasis on initial permeability studies, ”Journal of Magnetism and Magnetic Materials, vol. 401, pp. 938–942, 2016.
13. S. F. Rafie, N. Abu-Zahra, and M. Sillanpää, “A comprehensive review of spinel ferrites and their magnetic composites as highly efficient adsorbents of rare earth elements,” Emerging Contaminants, vol. 11, no. 1, 2025.
14. Z. Zhang, “Study on the influence of magnesium doping on the magnetic properties of spinel Zn-Mg ferrite,” Materials Today Communications, vol. 26. 2021.
15. N. Singh, A. Agarwal, S. Sanghi, and P. Singh, “Effect of magnesium substitution on dielectric and magnetic properties of NiZn ferrite,” Phys. B Condens. Matter, vol. 406, no. 3, pp. 687–692, 2011.
16. M. Derakhshani, E. Taheri-Nassaj, M. Jazirehpour, and S. M. Masoudpanah, “Structural, magnetic, and gigahertz-range electromagnetic wave absorption properties of bulk Ni–Zn ferrite,” Sci. Rep, vol. 11, no. 1, pp. 1–13, 2021.
17. M. A. Saadi, E. Engineering, C. Seker, and E. Engineering, “Overview on Feeding Techniques of Microstrip Patch Antenna,” vol. 2, no. April, 2022.
18. S. H. Lin, C. Te Wu, Y. T. Yang, D. Z. Huang, J. Y. Wang, and J. J. Huang, “Design and fabrication of 5G silver thin film monopole antenna by screen printing process,” MRS Commun, vol. 15, no. 3, pp. 506–513, 2025.
19. K. Zhou, R. Ding, X. Ma, and Y. Lin, “Printable and flexible integrated sensing systems for wireless healthcare,” Nanoscale, vol. 16, no. 15, pp. 7264–7286, 2024.

20. I. H. Hasan et al., "Nickel zinc ferrite thick film with linseed oil as organic vehicle for microwave device applications," Mater. Chem. Phys., vol. 236, no. April, 2019.
21. G. Srinivasu, T. Gayatri, D. M. K. Chaitanya, and V. K. Sharma, "Influence of FR4 material substrate on diamond slotted ultra wideband antenna in 1.71 GHz to 12 GHz," Mater. Today Proc., vol. 45, pp. 5642–5648, 2021.
22. C. Balamurugan, T.S Arun Samuel, M. G. Raj S, P. Mary S, and S. Geege A, "Enhancing gain and bandwidth in a multiband microstrip patch antenna through L-slot and partial ground plane integration," Scientific Reports, vol. 15, no. 1, pp. 2–13, 2025.
23. J. Zhao et al., "Influence of Mg^{2+} replacement on the structure and magnetic properties of $Mg_xZn_{1-x}Fe_2O_4$ (x = 0.1–0.5) ferrites," J. Mater. Sci. Mater. Electron, vol. 32, no. 4, pp. 4008–4020, 2021.
24. N. Idayanti, Dedi, T. Kristiantoro, N. Sudrajat, D. Mulyadi, and A. Gustinova, "Effects of varying chemical composition with x = 0.1 - 0.7 on magnetic properties of soft ferrite $Ni_{1-x}Zn_xFe_2O_4$," IOP Conf. Ser. Mater. Sci. Eng, vol. 620, no. 1, pp. 0–8, 2019.
25. S. Joshi, M. Kumar, S. Chhoker, A. Kumar, and M. Singh, "Effect of Gd^{3+} substitution on structural, magnetic, dielectric and optical properties of nanocrystalline $CoFe_2O_4$," J. Magn. Magn. Mater, vol. 426, no. August 2016, pp. 252–263, 2017.
26. A. Sattar, B. Bofeng, M. Khalil, and M. Sajjad, "Detailed analysis of structural, optical and photo catalytic properties of spinel nickel doped magnesium zinc ferrites at different substitutions," Inorg. Chem. Commun, vol. 142, no. May, 2022.
27. A. M. Mohammad, S. M. Ali Ridha, and T. H. Mubarak, "Structural and Magnetic Properties of Mg-CoFerrite Nanoparticles," Digest Journal of Nanomaterials and Biostructures, vol. 13, no. 3, pp. 615–623, 2018.
28. S. Y. Lee, R. Nazlan, I. R. Ibrahim, and G. Bahmanrokh, "Influence of Mg and Ti substitutions on structural , microstructural, and magnetic characteristics of Ni-Zn ferrites," E3S Web of Conferences 681, vol. 03005, pp. 1–13, 2025.
29. S. Yonatan Mulushoa and N. Murali, "Comparison of Structural, dielectric and magnetic investigation of Cr^{3+} substituted Mg-Cu, Mg-Zn, and Mg-Ni ferrites system," Inorg. Chem. Commun, vol. 145, no. September, p. 110033, 2022.
30. O. H. Abd-Elkader, N. M. Deraz, and L. Aleya, "Effects of Zinc Substitution on the Microstructural and Magnetic Characteristics of Cubic Symmetry Nickel Ferrite System," Symmetry (Basel), vol. 15, no. 5, 2023.
31. J. Mazurenko et al., "Magneto-structural properties of Mg-substituted copper ferrite nanoparticles," Mater. Res. Express, vol. 11, no. 12, 2024.
32. A. Tariq et al., "Optimizing optical, dielectric, structural, and electrical properties in Cu-substituted Mg-Zn ferrite nanoparticles: Insights for sustainable energy and environmental solutions," J. Alloys Compd, vol. 1037, no. April, p. 182252, 2025.
33. S. Hasan and B. Azhdar, "Synthesis of Nickel-Zinc Ferrite Nanoparticles by the Sol-Gel Auto-Combustion Method: Study of Crystal Structural, Cation Distribution, and Magnetic Properties," Adv. Condens. Matter Phys, vol. 2022, 2022

34. M. D. Jahan, C. Das, and N. Sarker, "Design Analysis of a Micro-strip Patch Antenna for RFID, WiMAX and X-band Applications,"1st International Conference on Advances in Science, Engineering and Robotics Technology 2019, vol. 2019, no. Icasert, 2019.
35. M. A. Jusoh, N. I. E. Pamin, N. I. Z. Azman, R. Nazlan, and S. A. Harun, "Feasibility and performance of TiCN-based patch antennas for microwave antenna applications," J. Mater. Sci. Mater. Electron, vol. 35, no. 22, pp. 1–11, 2024.

Adulticidal and Antimicrobial Potential of *Citrus aurantifolia* Fruit Peel-Derived Bioinsecticides against *Aedes aegypti* Linnaeus (Diptera: *Culicidae*) and Pathogenic Microbes

Nabila Adlina **Nasruddin**[1], Nur Raihana **Ithnin**[1], Hidayatulfathi **Othman**[2], Zatul-'Iffah **Abu Hasan**[3], Norhanim **Kamaruddin**[1], Siti Farah **Musa**[1], Haniza **Hassan**[4], Ricca Rahman **Nasaruddin**[5], & Norashiqin **Misni**[1]

[1]Department of Medical Microbiology, Faculty of Medicine and Health Sciences, Universiti Putra Malaysia, 43400 Serdang, Selangor, Malaysia

[2]Centre for Toxicology and Health Risk Studies, Faculty of Health Sciences, Universiti Kebangsaan Malaysia, Jalan Raja Muda A. Aziz, 50300 Kuala Lumpur, Malaysia

[3]Faculty of Medicine and Health Sciences, Universiti Sains Islam Malaysia, Bandar Baru Nilai, 71800 Nilai, Negeri Sembilan, Malaysia

[4]Department of Human Anatomy, Faculty of Medicine and Health Sciences, Universiti Putra Malaysia, 43400 Serdang, Selangor, Malaysia

[5]Department of Biotechnology Engineering, Kulliyyah of Engineering, International Islamic University Malaysia, Kuala Lumpur 50728, Malaysia

*Corresponding author's phone: +603- 9769 2358
E-mail: norashiqin@upm.edu.my

Received: 12 September 2025; Accepted: 2 February 2026

ABSTRACT

Mosquito-borne diseases pose significant public health challenges, necessitating effective control strategies. Given the health risks associated with synthetic repellents, natural adulticides are crucial for mosquito management. This study investigated various form of *Citrus aurantifolia* Fruit Peel (CAFP)- derived bioinsecticides, including plant extract, essential oil, and silver nanoparticles (AgNPs) for its adulticidal against adult *Aedes aegypti*, as well as its antimicrobial property. WHO topical bioassay was used to test the efficacy of these adulticides, while histological analysis further assessed their toxic effects. The effect of LC_{90} of these adulticides were screened against *Escherichia coli*, *Staphylococcus aureus* and *Candida albicans* using disc diffusion method. All bioinsecticides demonstrated adulticidal activity against *Ae. aegypti*. Overall, the essential oil from the peel of *Citrus aurantifolia* showed prominent effect with LC_{50} and LC_{90} value of 11.82 % and 23.41 %, respectively, followed by AgNPs- CAFP with 11.28 % and 30.99 %, and lastly was CAFP- plant extract at 14.51 % and 31.19 %. The order of potency was as follows: essential oil > silver nanoparticles > plant extract. Histological abnormalities observed in thoracic muscles of treated mosquitoes explains the toxicity and subsequent mortality caused by these insecticides. Essential oil showed promising inhibitory activity against the bacterial strains, whereas AgNPs were effective in inhibiting fungi. These findings pave the way for the development of novel herbal intervention, optimizing the most effective forms for controlling dengue vectors. Moreover, the demonstrated antimicrobial activity of these bioinsecticides further supports their other potential as multi-purpose agents in public health management.

Keywords— nanoparticles; essential oil; plant extract; mosquito; histology

1.0 INTRODUCTION

Mosquitoes are among the deadliest creatures on earth that threaten health hazards in humans, posing nuisance problems and mechanically transmitting pathogens causing diseases. One of the most prominent vectors among these is the *Aedes* spp., which is in charge of spreading deadly diseases including dengue, Zika, and chikungunya. These mosquitoes, particularly *Ae. aegypti* and *Ae. albopictus* are difficult to control as they can grow their populations quickly and flourish in urban areas. The diseases they transmit place an immense burden on healthcare systems worldwide, leading to millions of cases and thousands of deaths each year. At present, there is no vaccine effectively safeguard against mosquito-borne illnesses, with the exception of yellow fever and Japanese encephalitis [1]. Thus, mosquito vector control was considered the best strategy for preventing disease. There are several strategies for controlling and managing mosquito vectors, but chemical control is the strategy that has been used worldwide and extensively in everyday life.

Although chemical insecticides applications were intensified are considered as a successful vector control, yet, their frequent application has negatively impacted human health, non-target organisms, and the emergence of resistance. The extensive use of pyrethroids inevitably elicit levels of resistance in *Ae. aegypti* [2]. Early detection of resistance could assist authorities in deciding well-suited control strategies to minimize operational failures of *Ae. aegypti* control. Hence, there is a need to find alternative adulticides from plant-based options which are effective, safe, eco-friendly, biodegradable, non-toxic to humans and inexpensive as an alternative to chemical insecticides.

Plant extracts and essential oils have shown dominant activity against mosquitoes and other insect pests as claimed by most of the literatures. They are highly promising as safe alternatives to chemical insecticides. Plant extracts and essential oils are safe for human health and the environment, as they have been declared to be low-risk active substances by European Food Safety Authority (EFSA) [3]. They do not pollute the environment but rapidly degrade in soil and water. Moreover, it is difficult for mosquito vectors to develop resistance towards them [4].

Citrus aurantifolia (Christm.) commonly known as lime, is a small evergreen tree belonging to the Rutaceae family. Its fruit, known for its tart flavor, is widely used in culinary applications, beverages, and traditional medicine. The fruit peel, in particular, is rich in essential oils that contain bioactive compounds such as limonene, flavonoids, and terpenes, which have been found to possess various biological activities, including insecticidal, antimicrobial, and antioxidant properties [5,6,7]. These characteristics make *C. aurantifolia* an attractive candidate for use in pest control and other therapeutic applications.

Despite the growing body of literature highlighting the efficacy of various *Citrus* spp., particularly in the context of insecticidal properties, few of the research has primarily focused on the use of *Citrus aurantifolia* Fruit Peel (CAFP) essential oil as an adulticide. A critical gap remains in comparing the efficacy of *C. aurantifolia* Fruit Peel in various forms of adulticides against adult *Ae. aegypti* including the new rising adulticides in the form of silver nanoparticles (AgNPs) synthesized using this peel. Furthermore, the application of AgNPs synthesized using *C. aurantifolia* Fruit Peel against adult mosquitoes using standardized methods such as the WHO topical bioassay has not yet been explored in the existing literature.

In view of this, the present study seeks to address this knowledge gap by comparing the efficacy of various adulticidal forms derived from *C. aurantifolia* Fruit Peel (CAFP), including essential oil, plant extract, and silver

nanoparticle, using the WHO topical bioassay. To the best of our knowledge, this is the first study to evaluate the efficacy of AgNPs synthesized using plant based against adult mosquitoes, focusing using WHO topical bioassay method, as well as the histotoxic assessment. Additionally, this study is also the first study to directly compare these three forms of *C. aurantifolia* as adulticides, namely the plant extract, essential oil and silver nanoparticles, by providing novel insights into their relative effectiveness and potential applications in mosquitoes control. Thus, the study aims to conclude which adulticides are most effective in controlling *Ae. aegypti* adults, whether in the form of plant extract, essential oil or AgNPs. Additionally, the study evaluates their antimicrobial efficacy against pathogenic microbes. This comparison will not only clarify the most potent form but also provide valuable guidance for the development of sustainable pest control strategies, including broad-spectrum insecticides or also known as multipurpose agents, effective against both insect and microbes.

2.0 MATERIALS & METHODS

Extraction of aqueous fruit peel extract and essential oil

The fruit peels of *C. aurantifolia* was purchased from Chemical Engineering Pilot Plant (CEPP), Universiti Teknologi Malaysia, Malaysia, in the form of extract powder. Voucher specimens (KM 0115/24) were deposited in Institute of Bioscience, Universiti Putra Malaysia and authenticated by the Biodiversity Unit, Dr. Khairil Mahmud. 1 Gram of fruit peel powder was mixed with 100 mL of ultra-pure water and stirred. The mixture was boiled for 20 min at 60°C. The suspension thus obtained was cooled, filtered through Whatman filter paper No. 1 (25 µm). The extract was then freeze-dried using a Freeze Dryer (Labconco, USA) to obtain a powder form, for easier preparation of various concentrations to dilute with the solvent. It was stored under refrigeration for future use. The essential oil was extracted from the same batch of peel material by The Element Sdn. Bhd. (Kedah, Malaysia) using an automated cold-pressing machine.

Biosynthesis of silver nanoparticles

Silver nanoparticles used in this study were synthesized following the optimized protocol reported in our previous study [8]. The concentration of 4 mM aqueous solution of $AgNO_3$ was prepared using ultra-pure water and used for the synthesis of silver nanoparticles with the help of CAFP as a stabilizing and reducing agent. 10 mL of this extract was mixed with 30 mL of 4 mM of $AgNO_3$ solution, and kept in a water bath (70 °C; 4h). The formation of AgNPs then was confirmed as the colour changes into reddish brown colour. Then, AgNPs were centrifuged at 40,000 rpm for 15 min and washed to discard clear supernatant solution (to remove unwanted metabolites or so-called unbound plant extract residue). The pellet was then obtained and dried using a Freeze Dryer (Labconco, USA), forming a powder. The physicochemical characterization of the synthesized AgNPs, including UV–Vis spectroscopy, FTIR analysis, and FESEM imaging, has been previously reported in our earlier study [8]. In the present work, additional analyses including Dynamic Light Scattering (DLS) and High-Resolution Transmission Electron Microscopy (HR-TEM) were performed to further characterize the nanoparticles used in this biological evaluation.

High resolution transmission electron microscope (HR-TEM)

The sizes and morphology of the synthesized AgNPs were analyzed using a High-Resolution Transmission Electron Microscope (HR-TEM). The morphological analysis of the synthesized AgNPs was carried out following the methods described previously [43], with a few modifications. A dried powder of AgNPs was prepared by dispersing about 2

mg of the powder in acetone and ultrasonicating it for 5 min. The sample was placed on a copper grid coated with carbon film and dried at room temperature for 15 min. The HR-TEM measurements were performed on a F.E.I Technai G2 F20S-TWIN (Hillsboro, United States). The average diameter and shapes of AgNPs were determined from the HR-TEM micrographs, while the distribution of the nanoparticles was determined by counting the approximate number of nanoparticles on the micrograph. The photomicrograph obtained was analyzed using Image J (version 1.5 NIH) and Origin Lab software (Version 2022). The results of the average size and distribution of the nanoparticle were presented in a histogram.

Dynamic Light Scattering (DLS) and Particle Size

The average particle size, distribution, and zeta potential (ZP) of synthesized AgNPs were determined using a Zetasizer (Nano ZS-90 Malvern Instruments, Malvern, United Kingdom). The analysis was conducted following the method previously described [44], with some modifications. The synthesized AgNPs powder aliquot was dispersed in 15 mL of deionized water and sonicated for 15 min. Three millilitres of the solution were filtered through a 0.20 µm pore-sized syringe, and then the solution was analyzed. The average particle size distribution and ZP were determined by measuring the dynamic fluctuation of the light intensity of the colloidal particles. The measurement of the average hydrodynamic diameter of the particles, peak values in the hydrodynamic diameter distribution, and polydispersity index (PDI) were recorded and analyzed using Zeta Sizer software (version 7.11). All measurements were carried out in triplicate with a temperature equilibration time of 1 min at 25 °C. The results were presented in the graph showing the peaks and values.

Insecticides preparation

All form of *Citrus aurantifolia*-based adulticides such that the plant extracts, essential oil, and silver nanoparticles were formulated into the same concentrations viz: 0.5%, 5%, 10% and 18% for ease of the comparison. The CAFP- plant extract was prepared by combining with 0.1% acetone as a solvent or diluent to obtain the desired concentration. Similar to the preparation of CAFP- plant extract, the essential oil was mixed with 0.1% acetone, but with an additional one drop of Tween 80 as an emulsifying agent, preventing the oil from separation phase. Meanwhile for AgNPs-CAFP, this formulation was prepared by agitating the silver nanoparticle powder with 0.1% acetone using a sonicator (Clifton, United Kingdom).

Mosquitoes rearing

An established laboratory colony of *Ae. aegypti* (susceptible strain) which originated from Institute for Medical and Research (IMR) of Malaysia were reared under controlled conditions at the insectarium of Department of Medical Microbiology, Universiti Putra Malaysia. The conditions were maintained at 27 ± 1 °C, with 75 ± 5% humidity under light 12:12 h (day and night). Nulliparous 3-5 days old, non-blood-fed adult female Ae. aegypti mosquitoes were used for testing the effects of CAFP- plant extract, CAFP-essential oil and AgNPs- CAFP.

Topical application bioassay

The process of WHO Topical Application Bioassay was based on the recent study with slight modifications [9]. Female adult *Ae. aegypti* mosquitoes were aspirated out of the cage in groups of 25 and subsequently transferred into individual plastic cup designated for each of the concentration. These cups were then securely enclosed with netting and placed in a freezer (0 °C) for precisely 5 min 30 seconds to induce a state of stun through temperature shock. This duration

significantly influenced the mosquitoes' condition, as exposure for less than 6 min at 0 °C resulted in a brief recovery period, while exceeding 6 min led to thermal mortality. After the mosquitoes were sufficiently knocked down, each cup of mosquitoes was weighed to the nearest 0.1 g precision using an analytical scale. The mosquitoes were immediately transferred onto a Petri dish lined with filter paper and positioned on ice to ensure their immobilization. The entire procedure for transferring mosquitoes used an insecticide- free paintbrush, instead of forceps, aiming to minimize stress and physical damage to the insects which can lead to bias in result. Mosquitoes were thereafter dosed with 1 µl of control or adulticide solutions using a Multipette® Plus (Eppendorf, Germany). After dosing, the mosquitoes were poured back into their respective plastic cups, provided with 10% sucrose solution. Mortality was assessed 24 hr later. At the end of a 24 hr recovery period, the mosquitoes were considered dead if they showed no sign of movement such as lying on the bottom of the plastic cup and not responding to mechanical stimulation. Six replicates for each form of adulticides were conducted from different rearing batches. All treatments were treated in a similar manner in all forms of adulticides including the controls. Percent mortality was corrected by using Abbott's formula. Permethrin was used as a positive control, while for the negative control, 0.1 % acetone and 4 mM of (corresponding to the concentration used during nanoparticle synthesis) were employed. These dead mosquitoes from the treatments and controls were then collected for further histological and microscopy analysis.

The percentage mortality was calculated thus:

$$\text{Percentage mortality} = \frac{\text{Total number of dead mosquitoes}}{\text{Total number of mosquitoes}} \times 100$$

Histological analysis

The dead adult *Ae. aegypti* mosquito was preserved in 10% formaldehyde for histological analysis 24 hr post testing with the treatments. The samples were then processed using an overnight automatic tissue processor (Leica TP1020, German) with a succession of ethyl alcohol and washed with xylene. It was then embedded in paraffin wax using histoembedder tissue (Leica EG1160, German). They were trimmed and sectioned using a microtome (Leica RM2235 cwEU, German) at a thickness level of 20 um and 4 um respectively. All tissue blocks should be stored in the freezer before trimming and sectioning (Fig. 1). Trimming and sectioning should be performed immediately after removing the blocks from the freezer to ensure the tissue remains intact and does not become shredded. After sectioning, the paraffin ribbon was floated onto the surface of a warm water bath for fishing technique. The tissue then was air-dried and stained using standard technique of Hematoxylin and Eosin (H&E) staining with an automated slide stainer (Tissue-Tek Prisma®Plus Sakura, Japan). Following this, examination of tissue was conducted using a light microscope (Olympus CX33, Japan) at 600X magnification and photomicrographs were taken using a digital camera.

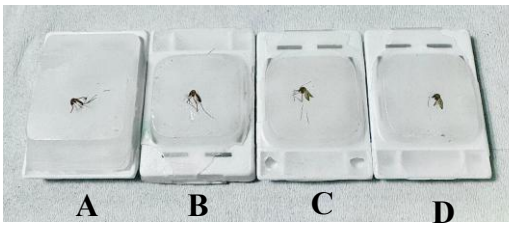

Fig. 1: Tissue blocks of adult *Ae. aegypti* after treatment with various form of adulticides after trimming process using microtome. (A) Negative control (B) Treatment with CAFP- plant extract (C) Treatment with CAFP- essential oil (D) Treatment with AgNPs- CAFP.

Antimicrobial disc diffusion assay: growth inhibition

A disc-diffusion assay was carried out according to the National Committee for Clinical Laboratory Standards Guidelines and previous study with small modifications [6,42]. he disk diffusion assay was conducted to assess the antimicrobial activity of various forms of CAFP, namely, plant extract, essential oil, and AgNPs against common microorganisms, including *Staphylococcus aureus* ATCC 27853 (a Gram-positive bacterium), *Escherichia coli* ATCC 25922 (a Gram-negative bacterium), and *Candida albicans* ATCC 60193 (a fungus). A representative microorganism from each category was selected to assess antimicrobial activity according to the LC_{90} value concentration for each treatment. The bacterial and fungal inoculum was prepared from an overnight culture on Mueller Hinton Agar (HiMedia, India) and Sabouraud Dextrose Agar (Oxoid®, United Kingdom) respectively. Colonies were directly suspended in 0.90% sterile saline solution to achieve a turbidity equivalent to the 0.5 McFarland standard (approximately 1.5x 10^8 CFU/ml), and this was compared with a commercialized McFarland standard. Aliquots (100 ul) of the suspensions were spread over the agar surface using a sterile cotton swab in order to get a uniform microbial growth. Under aseptic conditions, sterile paper discs (Whatman No. 1, 6 mm in diameter) were placed on the agar surface and immediately impregnated with 10 µL of LC_{90} concentration of the respective treatments. Blank paper discs (Liofilchem, Italy) were used as the negative control. As for reference control, Ciprofloxacin antibiotic disc (Oxoid®, United Kingdom) was used for the *S. aureus* and *E. coli*, whereas Fluconazole (Oxoid®, United Kingdom) antifungal disc was used for the *Candida albicans*. The plates were incubated at 37˚C for 24 hr for bacterial strains and 25 ˚C for 2 days for fungi, after which zones of inhibition were observed, measured and interpreted. After incubation, the inhibition zones were measured in mm. All experiments were carried out in six replicates and the mean ± SD values were presented. The scale of measurement was as follows: no inhibition zone < 12 mm, moderate inhibition zone 12- 20 mm and strong inhibition≥ 20 mm (disc diameter included) and. It is important to note that a fresh stock suspension was prepared each time, and all experimental conditions mentioned above were maintained constant under aseptic conditions.

Statistical analysis

Data were presented as means ± standard deviation (SD) of six replicates. Mean adult mortality and the effect of concentrations were calculated using the software IBM® statistical package for social sciences (SPSS) version 29, with a probit regression analysis for calculating LC_{50} and LC_{90} at a 95% confidence limit, and other statistics such as upper confidence limit (UCL) and lower confidence limit (LCL) also were obtained. To determine the most effective adulticides in vary concentrations, two-way ANOVA followed by a post hoc, Tukey test to determine the differences between each of the treatments.

3.0 RESULTS AND DISCUSSION

High-Resolution Transmission Electron Microscope (HR-TEM)

The High-Resolution Transmission Electron Microscope (HR-TEM) micrograph (Fig. 2) showed the size, shape, and distribution of biosynthesized AgNPs. The micrograph indicates nearly all the biosynthesized AgNPs were spherical in shape and the size of the particles ranges between 7.08- 28.15 nm, with an average mean particle size of 18.22 ± 5.43 nm. The HR-TEM micrograph (Fig. 3) showed spherical-shaped biosynthesized AgNPs at different magnifications of x25,000 and ×100,000. This is consistent with previous

findings that used plant extract in the synthesis of AgNPs [43, 45].

extract for AgNPs synthesis found that the AgNPs displayed spherical shape with size

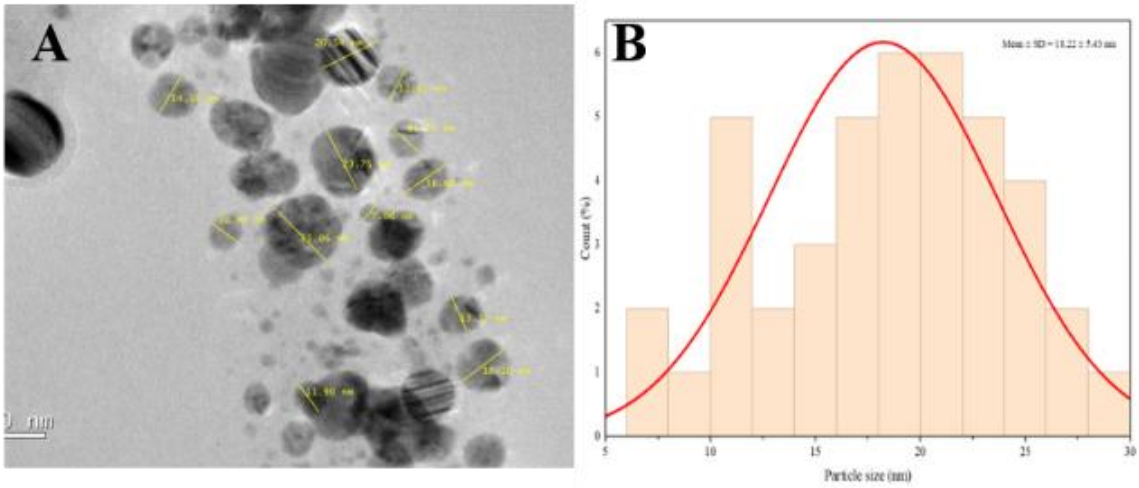

Fig. 2: (A) HR-TEM micrograph of AgNPs showing scattered, and spherical shape nanoparticles (B) HistoGram of average particle size of AgNPs (×100, 000 magnification).

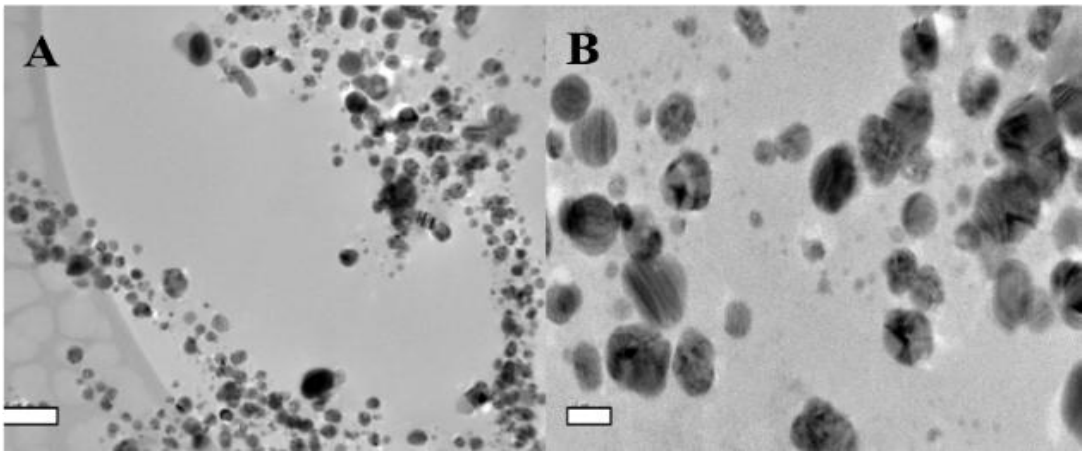

Fig. 3: HR-TEM micrograph of biosynthesized AgNPs showing spherical shaped nanoparticle under two different magnifications (A) ×x25,000 (B) × 100,000

Consistent spherical morphology has also been widely reported for AgNPs synthesized using *Citrus* peel extracts across different *Citrus* spp.. For instance, it is reported AgNPs synthesized using the peel extract of *Citrus tangerine* that is spherical, with average sizes of 10-70 nm [46].

Similarly, HR-TEM and FESEM from biosynthesis of AgNPs using *Citrus sinensis* peel extract revealed that the AgNPs are polydispersed and spherical in shape, with an average size of 10 ± 1 nm for the synthesis at 60 °C [47]. Likewise, a study employing *Citrus grandis* peel ranging from 20-30 nm [48]. Although AgNPs synthesized from different *Citrus* spp. consistently exhibit spherical morphology, variations in this particle size can be attributed to differences in synthesis parameters such as reaction temperature, plant extract concentration, $AgNO_3$ concentration, and pH [49]. These factors influence nucleation and growth processes during green synthesis, resulting in size variation when similar *Citrus* spp. peel extracts are employed.

Dynamic Light Scattering (DLS) Analysis

Dynamic light scattering (DLS) was employed to analyse the polydispersity index (PDI), hydrodynamic size, and zeta potential of AgNPs. The PDI serves as a key indicator of nanoparticle size distribution uniformity [50]. It provides insight into the degree of size variation within a sample, where values below 0.1 indicate a highly monodisperse system, while those above 0.4 reflect significant polydispersity. A PDI within the range of 0.1 to 0.4 represents a moderately polydisperse nanoparticle population [51].

In this study, the PDI values of AgNPs- CAFP was recorded as 0.665, demonstrating a highly polydisperse (Fig. 5).. This high PDI value signifies greater heterogeneity in particle size distribution. Thus, this finding is in line with the result obtained in the UV-Vis and HR-TEM micrograph, where the broad peak of surface plasmon resonance peak observed in the UV–Vis spectrum suggests polydispersity, and the HR-TEM micrographs reveal nanoparticles with slightly varied sizes.

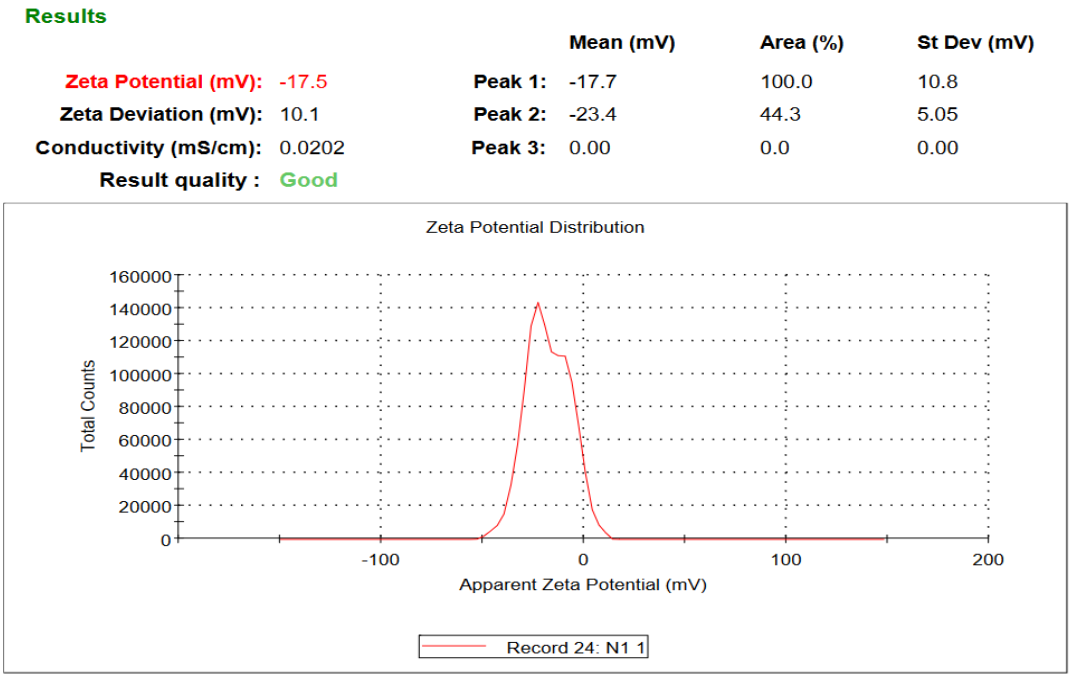

Fig. 4: Zeta Potential (ZP) of the AgNPs biosynthesized using CAFP extract

The possible reasons for the discrepencies observed in sizes of AgNPs could be method of synthesis used, variations in phytochemical compositions and uncontrolled nucleation, which can lead to the formation of AgNPs with diverse size distributions [52]. In fact, many studies point out that AgNPs produced using plant extracts often show a broad size distribution (polydisperse) due to the complex mixture of phytochemicals in the extract acting as reducing and capping agents [53, 55]. Hence, a PDI value below 0.7 is generally considered acceptable for plant- mediated AgNPs associated due to the complex plant extracts [56].

This finding is in line with several studies using *Citrus* peel in AgNPs synthesis. For instance, *Citrus unshiu* peel-mediated AgNPs reported a polydispersity (varied and broad size distribution), with a relatively high PDI value of 0.578 [57]. However, study using *Citrus microcarpa* peel extract which yielded a much low PDI value of 0.363, reflecting moderate polydisperse of AgNPs [58]. Similarly, *Citrus sinensis* peel–mediated synthesis of

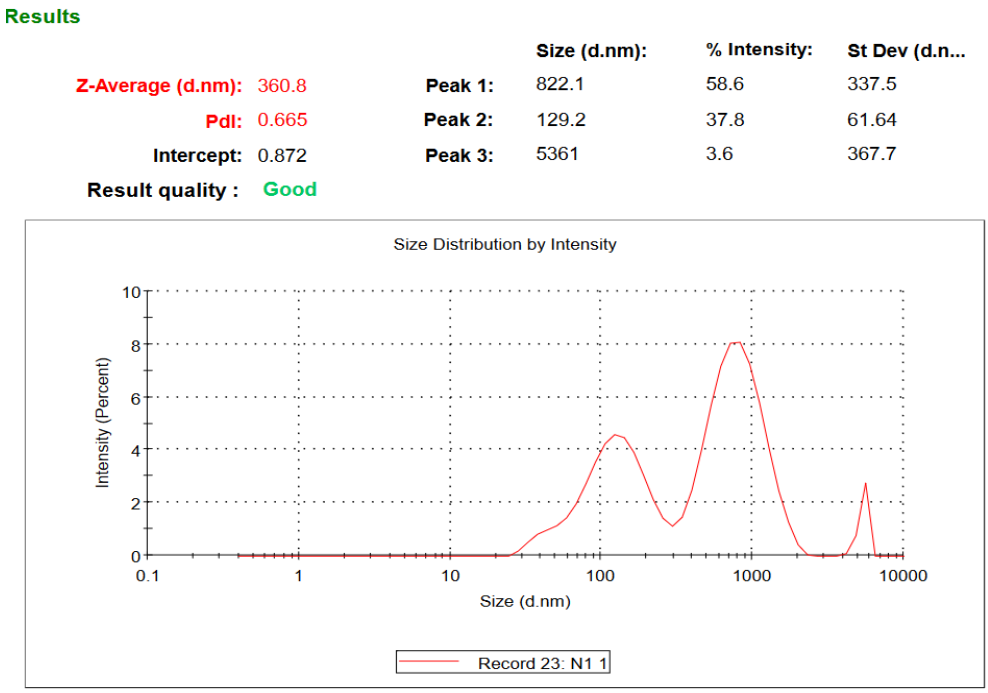

Fig. 5: Particle size distribution by intensity of AgNPs biosynthesized using CAFP extract

AgNPs yielded a PDI of 0.497 in DLS characterization, indicating moderate polydispersity [59]. Although these studies report different PDI values across *Citrus* spp., all values remain below 0.7, supporting the good quality of AgNPs which were commonly observed in plant-mediated AgNPs biosynthesis [56].

PDI remains a crucial parameter for evaluating nanoparticle uniformity and its implications for functional performance [60]. While monodisperse nanoparticles are often preferred for drug delivery systems and biomedical applications, polydisperse AgNPs on the other hand been reported to exhibit enhanced insecticidal activity. This enhanced efficacy is attributed to the presence of nanoparticles with varied sizes that can act through multiple mechanisms simultaneously, including cuticular penetration, varied surface reactivity, and prolonged interaction with insect tissues. Smaller nanoparticles may penetrate the cuticle more effectively, while larger particles may contribute to sustained toxicity through prolonged surface contact and gradual release of active nanoparticles [61].

The HR-TEM analysis confirms the PDI results, showing that AgNPs-CAFP has a significant polydispersed size distribution. Since PDI values above 0.4 indicates high polydispersity, the HR-TEM images support this finding by visually showing some variation in particle sizes. This suggests that factors like nanoparticle formation and interactions in the solution may influence their dispersion.

DLS measures the hydrodynamic size, including the particles, hydration shell, and surfactant coating. DLS often reports larger sizes than HR-TEM, which may be due to the influence of Brownian motion, which reflects actual particle size without the hydration layer [62]. Additionally, DLS measures particles in solution, where they may aggregate, while HR-TEM measures dried samples, providing more precise size estimates [63].

The hydrodynamic diameter of AgNPs- CAFP in this study is 360.8 nm. This finding is consistent with previous reports on fruit peel–mediated green synthesis of AgNPs, which demonstrate a

wide variation in hydrodynamic sizes. For instance, AgNPs synthesized using *Citrus sinensis* (orange) peel extract exhibited an average hydrodynamic diameter of 211.7 nm, while *Citrus microcarpa* peel–mediated AgNPs showed a size of approximately 235 nm [58, 59]. In contrast, pomegranate peel–mediated AgNPs displayed a much broader size distribution, with a mean hydrodynamic diameter of 624 nm [20]. The variation in hydrodynamic sizes could be due to the measured particles size which includes biomolecules that surrounds the surface of the silver particles and possible nanoparticle agglomeration (Brownian motion) in aqueous suspension.

Zeta potential (ZP) values provide an indication of nanoparticle colloidal stability. Nanoparticles with ZP values between 0 and ±10 mV are considered highly unstable, whereas values ranging from ±10 to ±20 mV indicate relative stability. ZP values between ±20 and ±30 mV suggest moderate stability, while values exceeding ±30 mV are generally associated with highly stable nanoparticle suspensions [19]. In this study, we obtained the ZP value of -17.5 mV, which indicates that the synthesized AgNPs are relative colloidal stability due to the presence of electrostatic repulsion between particles (Fig. 4). The negative zeta potential values are attributed to negatively charged compounds from *C. aurantifolia* peel extract acting as a capping agent [57, 13].

These findings align with previous studies reporting comparable zeta potential values for fruit peel–mediated AgNPs. For instance, *Citrus sinensis* peel–mediated AgNPs exhibited a zeta potential of −18.2 mV, corresponding to relative stability [59], while *Citrus unshiu* peel–mediated AgNPs showed a zeta potential of −24.6 mV, indicating moderate stability [54]**.** In addition to *Citrus* spp., AgNPs synthesized using pomegranate peel demonstrated a zeta potential of −20.1 mV, which also reflects moderate colloidal stability [20]**.** Hence, these results confirm that the zeta potential value obtained in the present study falls within the range commonly reported for fruit peel–mediated AgNPs which generally possess relative to moderate stability.

Adulticidal activity using WHO Topical Bioassay

The results of three forms of CAFP i.e., plant extract, essential oil and AgNPs against female *Ae. aegypti* adults after 24 hr of exposure were provided in Fig. 6 and Table I. Percentage of mortality were directly proportional to concentration. During the first hour of exposure to these treatments, it is visually observed that the mosquitoes initially showed episodes of excitement and then collapsed, displaying unusual behavior, erratic or unable to fly in coordinated manner in this recovery period. Plus, several of them (mainly at the highest concentration) remain static or moribund on filter paper of petri dish with symptoms of convulsion and paralysis prior to death.

The adulticidal activity of the CAFP was found to be form dependent. In general, all three forms exhibited effectiveness against female *Ae. aegypti* adults with results varying according to the concentration utilized. The adulticidal activity of CAFP against adults of *Ae. aegypti* 24 hr post exposure showed that essential oil was the most toxic form compared to the other forms. At the highest concentration of 18%, mortality percent of adult *Ae. aegypti* from CAFP- plant extract was 57.33%, 65.33% for AgNPs- CAFP and 70.67% mortality for CAFP- essential oil (Fig. 6), although no significant difference was observed between the adulticides at this concentration (p= 0.127).

Exposure to 4 mM $AgNO_3$ solution resulted in 0% mortality across all replicates, indicating no observable adulticidal activity under the tested conditions. The absence of mortality in the $AgNO_3$ treated group suggests that free Ag^+ ions alone did not contribute to adulticidal activity. Therefore, the enhanced bioactivity observed in the AgNPs- CAFP is likely attributable to nanoparticle

formation or synergistic interactions between silver and phytochemicals present in the plant extract.

The LC_{50} values of CAFP adulticides were recorded as 14.51%, 11.28% and 11.82% for CAFP- plant extract, AgNPs- CAFP and CAFP- essential oil respectively (Table 1), with a significant difference observed among adulticides (p= 0.042). Post hoc Tukey's test analysis further revealed a significant difference between the CAFP- plant extract and AgNPs- CAFP (p= 0.035), while no significant differences were observed between the CAFP- plant extract and CAFP- essential oil (p = 0.141), or between the CAFP- essential oil and AgNPs- CAFP (p= 0.736).

Meanwhile, the LC_{90} values were 31.19%, 30.99% and 23.41% for CAFP- plant extract, AgNPs- CAFP and CAFP- essential oil respectively, although no significant difference were observed among them (p= 0.080). These differences were also statistically significant (p = 0.014). Tukey's test analysis revealed a significant difference between the CAFP- plant extract and CAFP- essential oil (p = 0.012), whereas comparisons between the CAFP- plant extract and AgNPs-CAFP (p = 0.564), as well as between the CAFP- essential oil and AgNPs-CAFP (p = 0.089), did not yield significant differences.

Based on the adulticidal activity of CAFP- derived adulticides against adult *Ae. aegypti* mosquitoes, the order of effective percentage mortality can be arranged as follows, CAFP- essential oil > AgNPs-CAFP > CAFP- aqueous plant extract.

This present finding was in agreement with the previous report

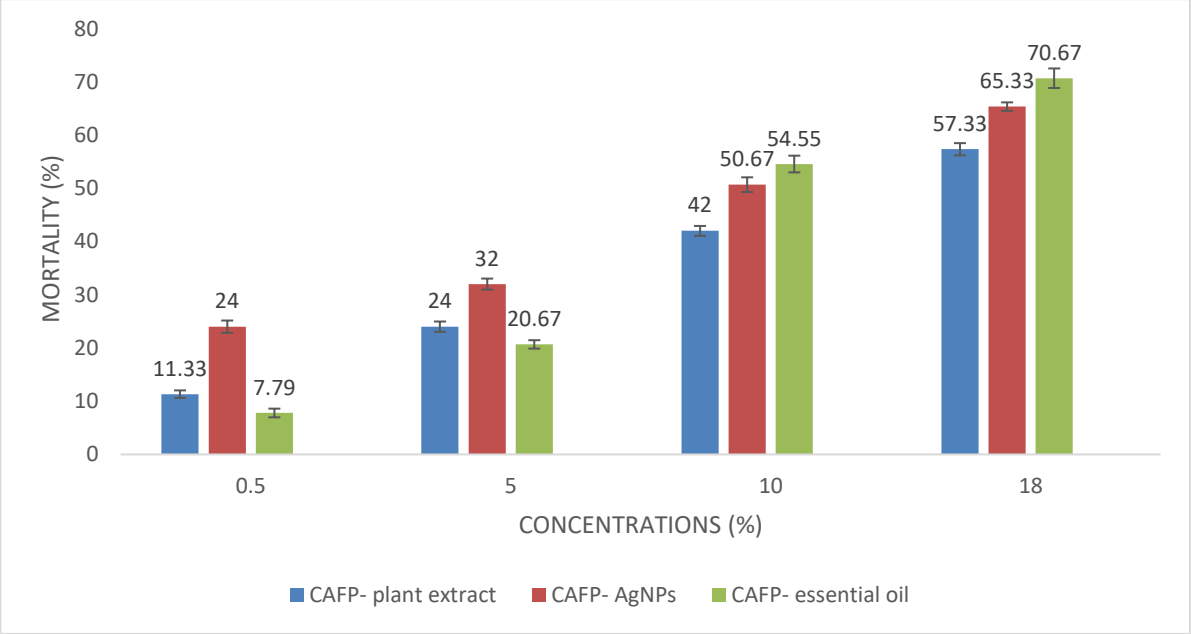

Fig. 6: Percent mortality of *Ae. aegypti* adults to four different concentrations of CAFP- plant extract, AgNPs-CAFP and CAFP- essential oil extracted from *C. aurantifolia* 24 hr after exposure. Data are presented as the mean ± standard error. All means obtained after 6 replicates. Vertical line denotes standard errors of the mean, while the numerical values displayed above each bar corresponds to the specific mortality percentages recorded.

TABLE I. Various forms of adulticides derived from *Citrus aurantifolia* Fruit Peel (CAFP) against female adults of *Ae. aegypti*, 24 hr post-exposure.

Adulticide	Conc. (%)	% Mortality (Mean ± S.D.)	LC_{50} (LCL-UCL)	LC_{90} (LCL-UCL)	Slope ± S.E.	$\chi 2$
CAFP-plant extract	0.5	11.33ab ± 1.72	14.51a (10.94 ± 21.80	31.19a (23.0 ± 57.65)	0.39 ± 0.94	1.316
	5	24a ± 2.37				
	10	42a ± 2.26				
	18	57.33a ± 2.80				
AgNPs-CAFP	0.5	24b ± 2.83	11.28ab (7.27 ± 18.50)	30.99a (21.93 ± 67.10)	0.34 ± 0.89	0.237
	5	32a ± 2.53				
	10	50.67a ± 3.39				
	18	65.33a ± 1.97				
CAFP-essential oil	0.5	7.79a ± 2.0	11.82b (9.33 ± 15.27)	23.41a (18.84 ± 33.41)	0.36 ± 1.51	1.527
	5	20.67a ± 1.94				
	10	54.55a ± 3.84				
	18	70.67a ± 4.50				
Positive control (Permethrin)		100	-	-	-	-
Negative control (acetone)		0	-	-	-	-
Negative control (4 mM $AgNO_3$)		0	-	-	-	-

Different superscript letters indicate significant differences ($p< 0.05$; One-way ANOVA with Tukey's post hoc test). For LC_{50} and LC_{90}, comparisons were made among adulticides; for mortality, comparisons were made among adulticides at the same concentration. Values with the same letter are not significantly different.

whereby claiming that CAFP-EO possesses potential adulticidal activity against adult *Ae. aegypti*, with 44% percent mortality at 0.1% concentration 24 hr after treatment using method of WHO tube susceptibility test [5]. A study using CDC bottle bioassay assessed the adulticidal activity of essential oils from *C. aurantifolia* peels against *Anopheles gambiae* mosquitoes proved that the EO exhibited concentration-dependent knockdown and adulticidal effects, with LC_{90} value of 1.84% [11].

However, the present study demonstrated that relatively higher concentrations (≥10%) of CAFP- EO are required to achieve more than 50% mortality at 24 hr post-exposure, as well as high LC_{90} value needed for CAFP-EO using the WHO topical application bioassay compared to previous studies. Nevertheless, this variation in results is probably due to differences in laboratory methodologies. Moreover, phytochemical composition, plant parts used, geographical origin and seasonal variation of the plant material, as well as differences in mosquito species tested also can influence the overall bioactivity [5, 12]. To date, there appear to be limited published studies where EOs and crude plant extracts have been directly compared for adult mosquito toxicity using WHO topical application bioassay in the literature, hence comparison with previous study is limited.

In comparing effectiveness of nanoparticles with aqueous plant extract, our finding demonstrated that AgNPs-CAFP presented better adulticides effect compared with the CAFP- plant extract. This current result is also comparable to earlier reports which conducted a comparison study of adulticidal effect between AgNPs and using plant extract only, on adult mosquitoes using WHO tube susceptibility test. For instance, maximum efficacy was observed with AgNPs synthesized using leaf aqueous extracts of *H. indicum* against the adult *Ae. aegypti* with $LD_{50} = 0.00296\%$ and $LD_{90} = 0.00543\%$, whereas for the treatment of *H. indicum* extract only, the value were much higher with $LD_{50} = 0.01235\%$ and $LD_{90} = 0.02192\%$. Hence, this signifies that AgNPs synthesized using plant extract was more effective in giving high mortality rate of adult *Ae. aegypti* compared to the plant extract only [14]. In other words, AgNPs required a significantly lower concentration to achieve high adulticidal efficacy against *Ae. aegypti*, indicating enhanced potency compared to the crude extract alone.

Other article also reported similarly whereby the AgNPs synthesized using *Chomelia asiatica* plant extract against adult *Ae. aegypti* was efficient in giving high mortality rate compared to the result of the plant extract only [15]. The maximum efficacy for AgNPs - *Chomelia asiatica* plant extract was observed at (LD_{50}= 0.00292%; LD_{90}= 0.00528%), whereas the plant extract only was at (LD_{50}= 0.01728%; LD_{90}= 0.03102%). Multiple studies confirmed that silver nanoparticles synthesized via plant extracts demonstrate significantly greater adulticidal activity than the crude extracts themselves, due to the attribution of their nanoscale size, greater penetration and ability to induce oxidative stress in mosquito cells causing cytotoxic effect.

The literature offers no publication on the toxicity of green synthesis of AgNPs against any adult mosquito spp., measured by topical application. While these studies highlight the potential of *Citrus* spp. in mosquito control, they may not have employed the WHO topical bioassay method. Thus, to our knowledge, this is the first report of AgNPs using plant extract overall against adult mosquitoes testing for WHO Topical Bioassay.

Collectively, these findings emphasize that the observed efficacy of plant-based adulticides are not solely dependent on the form of plant extract or the mosquito spp. tested, but is also significantly influenced by the methodological parameters employed in the assay. Factors such as the mode of exposure and bioassay type can markedly affect the LC values and mortality outcomes, thereby underscoring the importance of standardized protocols in evaluating botanical insecticides.

Variation in the activity of the three form of adulticides from the same plant against the adult stage of *Ae. aegypti* was another finding of the current study which may arise due to the difference in components in them. Chemically, essential

oils, are highly concentrated with only volatile aromatic compounds, whereas plant extract, contains a wider range of compounds including both volatile and non-volatile ones. In contrast, AgNPs are just particles of silver that range in size from 1 to 100 nanometers (nm). Different forms of adulticides from the same plant may act differently in regards to their mode of action. Essential oils and plant extract may act in a similar mode of actions with compounds playing roles in toxicity.

Overall, based on order or potency of CAFP- derived adulticides against adult *Ae. aegypti* mosquitoes are CAFP- essential oil > AgNPs- CAFP > CAFP- aqueous plant extract.

Penetration and Mechanism of action

CAFP- essential oil in the current study was the most effective form of adulticide compared to the CAFP- plant extract and AgNPs- CAFP, achieving the highest mortality number of adult *Ae. aegypti*. This is because essential oil is easily absorbed through the exoskeleton of adult mosquitoes due to its lipophilic nature. The exoskeleton of mosquitoes is composed largely of lipids, and many essential oil components are lipophilic (fat-soluble). This allows essential oils to dissolve and penetrate more readily into the cuticular layers, which are mainly composed of waxy substances. Lipophilic molecules are more likely to traverse this hydrophobic barrier such as those in essential oils traverse this hydrophobic barrier more effectively than hydrophilic agents like aqueous plant extracts or water-based nanoparticles.

However, little is known about the mode of adulticidal activity of plant extract and silver nanoparticles since this study is the first to report on the effect of AgNPs and plant extract on adult mosquitoes using WHO Topical Application Bioassay Test.

Given that the mosquito's water-resistant exoskeleton presents a significant barrier to penetration by water-based solvents, thus, the only way aqueous plant extract and AgNPs can enter the mosquito's body is through intersegmental membranes or cuticular sutures at the pronotum, which enables the toxins to be absorbed. It is hypothesized that only small amounts of AgNPs manage to enter the mosquito's body via these pathways causing histological changes as observed, while others accumulate on the surface of the exoskeleton [24], but still exerting histotoxic effects on the outer cuticular layer of mosquito. AgNPs has shown to be ineffective and hard in penetrating the human epidermal skin past beyond the stratum corneum [25].

In the present study, we hypothesize that a similar pattern of AgNPs penetration may apply to mosquito tissue, with difficulty of these nanoparticles to fully penetrate the exoskeleton as they are from water-based solvent. This limited penetration likely contributes to the reduced efficacy of AgNPs relative to essential oils as the total amount of AgNPs is not being fully absorbed compared to the essential oil. Prior studies have demonstrated that silver nanoparticles, particularly those exceeding 40 nm in diameter, struggle to pass through the stratum corneum and enter the skin. Meanwhile, for nanoparticles with a diameter less than 40 nm have been reported successfully penetrates the skin [23].

Therefore, in the present study, the synthesized AgNPs had an average diameter of 18.22 ± 5.43 nm as determined by HR-TEM analysis, with single spherical shape confirmed by FESEM [8]. Given their relatively small size, these nanoparticles may possess an enhanced ability to interact with and potentially penetrate the mosquito cuticle; however, direct evidence of transcuticular penetration was not established in this study. Further ultrastructural investigations scanning electron microscope (SEM) or transmission electron microscopy (TEM) are necessary to dig into the route of how AgNPs causing toxic to tissue.

The shape of nanoparticles also affects the tissue penetration capabilities. Spherical nanoparticles tend to penetrate deeper into the skin compared to ellipsoidal or rod-shaped particles. Studies have observed that spherical particles are located deeper in the epidermis and dermis, whereas ellipsoidal particles remain primarily in the stratum corneum and epidermal layers. Additionally, nanorods, despite their unique properties, have shown only penetrating a limited depth, at the outermost layers of the tissue [23]. Hence, size and shape significantly influences their ability to penetrate biological tissues.

Understanding the mechanisms by which these nanoparticles induce toxicity is crucial for developing effective mosquito control strategies. Metal nanoparticles exert toxic effects on adult mosquitoes through multiple mechanisms, including (1) oxidative stress, (2) cytotoxicity, and (3) genotoxicity. Certain metal nanoparticles (NPs) have been shown to generate DNA oxidation, mutations, decreased cell viability, distorted morphology, induced necrosis and apoptosis, and decreased proliferation [21]. In the present study, it was hypothesized similarly, whereby upon topical exposure with AgNPs, they interact with mosquito cells, leading to distorted morphology of the smooth muscle tissue, resulting in cellular dysfunction and increased mortality.

The nanoparticles has disrupt cell membranes, hindering essential cellular processes, and triggering apoptosis (programmed cell death). Silver and copper oxide NPs, have also been associated with DNA damage [21]. Additionally, a smaller size of nanoparticles means a greater surface area to volume ratio of nanoparticles, thus enhancing their chemical reactivity and biological activity, contributing to ROS production [22].

Unlike AgNPs which exert toxic effects through oxidative stress, cytotoxicity and genotoxicity, the biological activity of essential oil and plant are largely attributed to their major components. Although in some circumstances, major components may not always account for the total activity, the interaction of both major and minor components could somehow resulted in synergistic or antagonistic effects [16].

The present study demonstrated a tissue alteration in the thorax of the mosquitoes treated with essential oils and plant extract, as they were abundant with limonene (major compound), which belong to the monoterpenes group. This confirms with various studies reported that *d*-limonene as the predominant component, accounting for the major % area in *C. aurantifolia* fruit peel when analyzed using GC-MS in their respective studies designed for their own respective experiment [5, 6]. Using other insects, one research concluded that the application of *d*-limonene can led to significant mortality rate of bedbugs [17]. *d*-limonene effectively removes the waxy layer of an insect's respiratory system, leading to suffocation when applied directly [18]. In fact, *d*-limonene has been the most used botanical insecticide in California in the past decade (averaging >20,000 kg per year) [3].

Even though extracts from plants constitute a rich source of bioactive compounds that are biodegradable into non-toxic products, it is to note that essential oils are much more concentrated with compounds. Hence, this may explain the result from the present study, which shows that essential oils can cause a high mortality rate in adult *Ae. aegypti* compared to the plant extract, due to the concentrated compounds essential oils they contain, which are toxic or irritating to insects.

Effect of the adulticides on the histological changes.

Mosquito bodies are composed of three segments: the head, thorax, and abdomen. However, the histological studies in this research focused specifically on the thorax (pronotum) for several reasons: first, the treatment was applied directly to the pronotum area; second, the pronotum is a

crucial region for flight, as it contain flight muscles necessary for the mosquito to survive and obtain food; third, the head and abdomen part were rupture due to effect from the adulticide hence cannot be viewed.

Normal anatomy of untreated adult mosquito using H&E staining results were shown at 40X magnification in Fig. 7, comprising intact thoracic muscles, esophageal ganglions and intestinal tract. Nuclei and nucleoli stained blue-violet, while cytoplasm as well as extracellular matrix were colored in varying shades and intensities of pink in all specimens examined.

There were no signs of damage or disorientation in the smooth muscle at the thorax region of the control adult in Fig. 8(A). In contrast, *Ae. aegypti* adults treated with the three adulticides all showed similar alterations with the damage or deformation to most of the thoracic smooth muscle (or known as flight muscle), as shown in Fig. 8(B)- 8(D). The damage was observed solely in the thorax region of the adult mosquito.

An earlier study comparing the histological effects of gold nanoparticles and essential oil, both derived from *Artemisia vulgaris* leaf extract onto larvae stage of mosquito, demonstrated histological alterations in the digestive tract and midgut of third and fourth instar *Ae. aegypti* larvae following treatment [24]. Several histopathological alterations were observed in adult *Aedes* mosquitoes, including compound eyes degeneration, muscular damage with cellular infiltration, gut epithelial degeneration and necrosis, pyknotic nuclei in the malpighian epithelium, and ovarian cell degeneration were observed when treated with purple and white flower of *Ageratum conyzoides* Weed Extracts [16]. Another study also using a *Citrus* spp., namely, *Citrus sinensis* essential oil revealed obvious alterations in the cuticle, muscles, and midgut tissues including changes on the ultrastructural level of the third instar larvae of *Culex pipien* [26]. Although none of the studies mentioned above specifically attributed histotoxic effects to the treatment of AgNP, essential oils, or plant extracts derived from *Citrus* spp. specifically on the adult stage, the mechanisms observed are hypothetically similar to those in the current study, where histotoxicity was induced by various forms of adulticides derived from *C. aurantifolia* fruit peel.

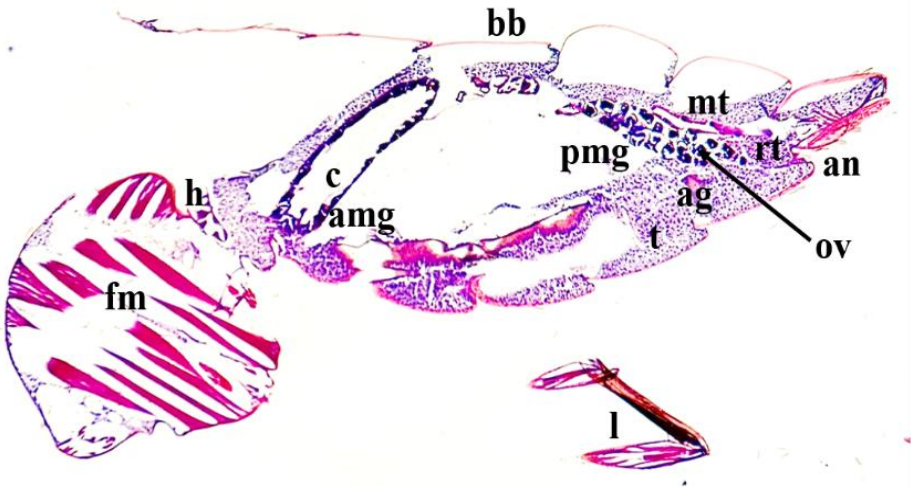

Fig. 7: Normal anatomy of untreated adult *Ae. aegypti*. Longitudinal section of a female. Hematoxylin and Eosin (H&E) staining of (an) anus; (ag) abdominal ganglia; (bb) bursh border; (c) cardia; (fm) flight muscle; (h) heart; (l) legs; (amg) anterior midgut; (pmg) posterior midgut; (mt) Malpighian tubules; (ov) ovary; (rt) rectum; (t) trophocytes, at 40X magnifications under light microscope.

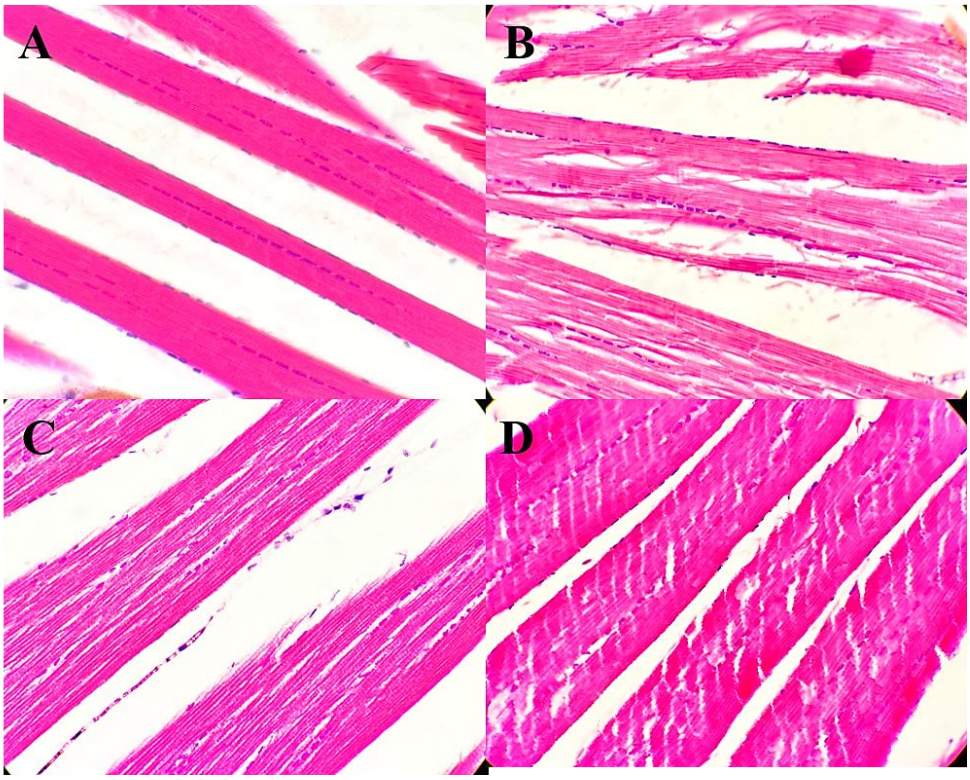

Fig. 8: Histological changes of the thorax of adult *Ae. aegypti* after treatment with various forms of adulticides derived from *Citrus aurantifolia* Fruit Peel (CAFP) at 600X magnification under light microscope. (A) Negative Control (B) Treatment with CAFP- plant extract (C) Treatment with AgNPs- CAFP (D) Treatment with CAFP- essential oil.

Despite the variation in the results using various forms of adulticides, they all still showed considerable mortality on *Ae. aegypti* mosquitoes, which is considered to be successful in managing the dengue vector. The thoracic smooth muscles are important organs that play a critical role in flight and the movement of the wings. It is essential for their ability to fly, survive and engage in reproductive activities. The thorax is made up of two primary parts: flight muscles and a thin-walled ellipsoidal or box-shaped exoskeletal cuticle where flight muscles attach [27]. As such, this cuticle is made up of chitin, water, and proteins, structured into different layers such as the endocuticle, exocuticle, and epicuticle [28]. Damage to these muscles could have created discomfort or difficulty in controlling the flight thereby leading to mortality [29].

Effect of LC_{90} value from different adulticides on the antimicrobial study

Disc diffusion assay, or known as the Kirby-Bauer test, is used to monitor antimicrobial resistance. Since the LC_{90} values that caused mortality in adult *Ae. aegypti* were obtained from each adulticide, thus, we intend to further investigate these LC_{90} values to evaluate their effects on common bacterial and fungal strains that are implicated in disease causation. In this study, AgNPs are effective in inhibiting the bacterial growth whereas CAFP- essential oil effective against fungal growth.

For comparison purpose, the antimicrobial activity of three different form of plant based adulticides against two bacterial and a fungal strain are summarized in Table II. The results represent the diameter of inhibition zone including diameter of paper disk (6 mm). A variation in antimicrobial properties of the analyzed adulticides were observed in the

study. Overall, CAFP- plant extract failed to inhibit all of the tested strains, both bacteria and fungi. However, LC_{90} concentration of AgNPs- CAFP showed consistently moderate antimicrobial activity (growth inhibition zone between 12- 20 mm) against both the bacterial spp. tested, whereas CAFP- essential oil showed an antifungal activity.

Previous studies have identified limonene as a major component of citrus oil, with evidence supporting its potent anti- *Candida* activity. This compound has been shown to inhibit *Candida albicans* growth by cell wall damage induced oxidative stress that leads to DNA damage. This cascade of events subsequently modulates the cell cycle and triggers apoptosis via nucleolar stress and a metacaspase- dependent pathway [30]. Although essential oil is hydrophobic and can penetrate the cell membrane of Gram-positive bacteria, thereby exerting their antibacterial effects through disruption of enzyme production, alterations in membrane functionality, and protein denaturation [31], this was not observed in our study, whereby it only susceptible to *C. albicans* but not to both of the tested bacterial strains, namely, *S. aureus* and *E. coli*.

Even though earlier study have reported that CAFP-EO (lime peel) exhibits stronger antimicrobial activity than grapefruit EO and orange peel EO against *S. aureus* (15 mm), *E. coli* (12 mm), and *C. albicans* (17 mm) [6], our study showed no antimicrobial activity when used CAFP-essential oil against the tested bacterial strains. This is perhaps due to several factors, including low concentrations, inadequate composition and bacterial resistance. The effectiveness of essential oils depends heavily on optimizing these variables. Studies have shown that at lower concentrations, essential oils may not exhibit significant inhibitory effects, and higher concentrations being required to inhibit microbial growth [32]. Essential oils consist of a complex mixture of volatile compounds, and the antimicrobial activity depends on the types and quantities of bioactive compounds like phenols, terpenes, aldehydes, and alcohols. Not all

TABLE II. Antimicrobial activity of three different forms of adulticides using *Citrus aurantifolia* Fruit Peel (CAFP) determined by disc diffusion assay.

Adulticides (LC_{90} Concentration)	*S. aureus*	*E. coli*	*C. albicans*
CAFP- plant extract (31.19%)	NI	NI	NI
CAFP- essential oil (23.41%)	NI	NI	12.0 ± 1.414
AgNPs- CAFP(30.99%)	11.83 ± 1.169	7.33 ± 0.516	NI
Permethrin (0.04%)	NI	NI	NI
Reference control[a]	32.0 ± 3.098	32.83 ± 0.408	20.50 ± 1.517
Blank disc[b]	NI	NI	NI

[a]Ciprofloxacin (5 µg) for bacterial and Fluconazole (25 µg) for fungal as a positive reference standard;
[b]Blank disc as a negative control;
NI- No zone of inhibition; Results were expressed as mean inhibition zone (mm) ± S.D of six replicates

essential oils contain sufficient quantities of compounds with antimicrobial activity, such that, phenolic compounds contribute significantly to antimicrobial action [33]. However, it is to take note that the evaporation of the essential oil and their constituents can affect the doses applied to paper discs and thus the result. Hence, additional studies using liquid culture assays to determine the minimum inhibitory concentrations (MIC) are necessary.

In present study, AgNPs- CAFP showed moderate antimicrobial activity (growth inhibition zone 12- 20 mm) against both the bacterial spp. tested, namely, *E. coli* and *S. aureus*. Other study also reported similarly whereby AgNPs synthesized from various extracts of *Citrus* fruit peels, including *C. aurantifolia*, exhibited notable antibacterial properties, with greater zone of inhibition in Gram-positive bacteria compared to Gram-negative. Specifically, inhibition zones measured in that study were 12.7 mm for *E. coli* and 13.3 mm for *S. aureus* [7]. These differences are largely attributed to variations in cell wall structure and composition, which influence how AgNPs may interact with the bacteria. The antibacterial effect for these particles might be due to the ability of the AgNPs to to disrupt cell membrane permeability, formation of free radicals, and interaction with thiol groups, prevent DNA replication, affect cellular signaling, and prevent biofilm formation [34].

The inhibitory activity of AgNPs against Gram-positive and Gram-negative bacteria is a controversial issue. A growing body of evidence reported that AgNPs are claimed to be more effective against Gram-negative bacteria [36, 37, 56]. This is because Gram-negative have a thinner peptidoglycan layer surrounded by an outer membrane containing lipopolysaccharides. The unique composition of this outer membrane can make them more susceptible to the disruptive effects of AgNPs [38]. However, interestingly, it seems that it has become a debate since few studies have claimed otherwise such that Gram-positive bacteria also is equally susceptible towards AgNPs [39]. Nevertheless, these variations in reported susceptibility between Gram-positive and Gram-negative bacteria are most likely attributable to differences in the physicochemical characteristics of the synthesized AgNPs.

The antimicrobial activity observed in the present study may be associated with the physicochemical characteristics of the synthesized AgNPs, including- particle size, shape and surface charge are also known to influence biological interactions and antimicrobial efficacy [38]. Smaller nanoparticles generally exhibit enhanced bioactivity due to their larger surface area, which facilitates greater silver ion release and direct interaction with microbial membranes [64]. A study demonstrated size-dependent biological effects in hepatic (HepG2) cells, showing that smaller AgNPs (10 nm) could enter the nucleus, whereas larger AgNPs (60 nm) remained aggregated in the cytoplasm [65]. In the present study, the AgNPs had an average size of 18.22 ± 5.43 nm, suggesting the same that AgNPs may penetrate bacterial cell walls and membranes, thereby contributing to their antimicrobial activity.

Nanoparticle shape morphology also influences antimicrobial activity. Synthesized AgNPs can be in various shapes, including spherical, triangular, cubic and rod-shaped [66]. A comparative study of synthesized AgNPs in three shapes showed that the highest bactericidal activity was observed in spherical forms, followed by disc-shaped and then triangular nanoparticles [67]. In the present study, FESEM analysis revealed that the synthesized AgNPs were predominantly spherical in shape, indicating that their morphology may have contributed to the enhanced antimicrobial activity observed.

Additionally, surface charge and colloidal stability also influence nanoparticle–bacteria interactions, such that a positively charged AgNPs exhibit

stronger interactions with bacterial cell membranes that contain lipopolysaccharides (LPS) and techoic acid, which are negatively charged [68]. Although the AgNPs synthesized in the present study with zeta potential (−17.5 mV) displayed a negative surface charge, the value was not highly negative. Thus, the observed antimicrobial activity may not be solely attributed to surface charge but rather to the combined effects of size, morphology, and surface characteristics.

In order to interpret the mechanism of AgNPs' antimicrobial activity, four different types of mechanisms have been proposed: (1) AgNPs' interaction with cell membranes, which alters membrane permeability and disrupts respiratory chain enzymes; (2) AgNPs' gradual diffusion into cells, which may negatively impact cellular enzyme activity and limit the transcription process by conjugation of silver particles to DNA; (3) Subcellular components leakage due to nanoparticles' interaction with the plasma membrane, which results in cell death; and (4) Free radical generation when the cell membrane is effected by silver ions [35].

Results of the current study also revealed that CAFP- plant extract did not display any inhibitory effect against the tested organisms, implying that any activity exhibited is attributed solely to AgNPs but not the plant extract which is used in the phytosynthesis. This is similar to the previous study whereby the *Citrus limon* peels extract alone does not inhibit bacterial growth when compared to the AgNPs-synthesized with *C. limon* [40]. This conclusion is drawn from a direct comparison of the antimicrobial effects of the AgNPs and the plant extract alone against these bacteria. In other words, the plant extract alone is ineffective in inhibiting bacterial growth unless it is in the form of AgNPs.

Moreover, in terms of CAFP- plant extract, one study claimed that both *Citrus sinensis* and *Citrus aurantifolia* peel extract, when prepared with ethanol, exhibited antibacterial property with moderate zone of inhibition against *S. aureus* and *E. coli* when used with much more higher concentration compared to the current study [20]. In addition, a study from Algeria also found that both leaf and peel extracts of *C. aurantifolia* extracted from ethanol and methanol exhibited significant antibacterial activity against multidrug-resistant *S. aureus* strains and *E. coli*, with inhibition zones ranging from 16.00 mm to 22.00 mm [41]. All of these previous study using *C. aurantifolia* peel aqueous extract that showed susceptibility against *S. aureus* and *E.coli* was due to the alcohol solvent used for the extraction. However, in the present study, water, a non-alcoholic solvent, was employed for the extraction of the plant material.

Different solvents target different compounds based on their polarity, thus, isolating a variety of compounds from plants. In this case, using water as a solvent for *C. aurantifolia* extraction in the formulation of CAFP- plant extract is not effective in inhibiting the growth of bacteria and fungi, as it fails to extract the targeted compounds that may act as antimicrobial agents. The antimicrobial potency of lime fruit is influenced by the solvent used, suggesting that certain active compounds in lime exhibit significant antimicrobial and antifungal effects, but are only released or extracted out with a specific solvent. Although water is the universal and most common solvent for preparing herbal extract. However, some bioactive compounds in plants are insoluble in water, meaning that methods such as preparing hot tea or boiling the plant in water may not effectively extract these components. Hence, the discrepancies may be attributed to factors such as differences in extraction methods, solvent types, plant cultivar variations, or experimental conditions.

4.0 CONCLUSION

In conclusion, the present study provides strong evidence supporting the

efficacy of lime peel extract of *Citrus aurantifolia* as an adulticidal agent against adult *Ae. aegypti* mosquitoes, with histological alterations further confirming its activity. Overall, all forms of adulticide demonstrated significant adulticidal effects, with the potency of *C. aurantifolia* fruit peel varying across different formulations. The order of potency was as follows: essential oil > silver nanoparticles > plant extract. The encouraging mosquito adulticidal activity of these three forms of adulticides might pave the way for the development of novel herbal mosquito formulations, optimizing the most effective form against *Ae. aegypti*. Moreover, the demonstrated antimicrobial properties of these bioinsecticides highlight their broader potential as multi-functional agents in integrated public health strategies. Overall, these findings suggest that lime peel could be effectively incorporated into vector control proGrams. However, to ensure more convenient outcomes, further field trials and a comprehensive analysis of the mode of action are recommended.

ACKNOWLEDGEMENTS

The authors acknowledged Universiti Putra Malaysia for awarding the IPM research grant (GP-IPM/2022/9736100) to support this research, as well as the Graduate Research Fellowship (GRF) program for aid in financial assistance and tuition fee waiver throughout the study. We wish to thank Universiti Putra Malaysia (UPM) for providing us with the facility to carry out the present study. The authors thank Mrs. Juita Chupri from Histology department UPM and Mrs. Wan Suhana Wan Mohd Shafie from Microbiology department UPM for their technical support and guidance, as well as providing the necessary facilities for histology and microbiology work.

REFERENCES

1. Centers for Disease Control and Prevention, CDC Health Information for International Travel 2024. Oxford University Press. 2024.
2. Z. H. Amelia-Yap, C. D. Chen, M. Sofian-Azirun, and V. L. Low, “Pyrethroid resistance in the dengue vector *Aedes aegypti* in Southeast Asia: Present situation and prospects for management,” Parasites and Vectors, vol. 11, no. 332, 2018.
3. M. B. Isman, “Botanical insecticides in the twenty-first century - fulfilling their promise?,” Annual Review of Entomology, vol. 65, pp. 233–249, 2020.
4. R. Pavela, F. Maggi, R. Iannarelli, and G. Benelli, “Plant extracts for developing mosquito larvicides: From laboratory to the field, with insights on the modes of action,” Acta Tropica, vol. 193, pp. 236–271, 2019.
5. R. Sarma, K. Adhikari, S. Mahanta, and B. Khanikor, “Insecticidal activities of *Citrus aurantifolia* essential oil against *Aedes aegypti* (Diptera: Culicidae),” Toxicology Reports, vol. 6, pp. 1091–1096, 2019.
6. I. O. Mohammed, A. A. Alrasheid, and S. M. Hussein Ayoub, “GC-MS analysis and study of the antimicrobial activity of *Citrus paradisi*, *Citrus aurantifolia*, and *Citrus sinensis* peel essential oils as hand sanitizer,” International Journal of Microbiology, vol. 2024, 2024.
7. S. A. Alsakhawy, H. H. Baghdadi, M. A. El-Shenawy, and L. S. El-Hosseiny, “Antibacterial activity of silver nanoparticles phytosynthesized by *Citrus* fruit peel extracts,” Bionanoscience, vol. 12, no. 4, pp. 1106–1115, 2022.
8. N. A. Nasruddin, N. R. Ithnin, H. B. Othman, Z. I. Abu Hasan, and N. Misni, “Green synthesis of silver nanoparticles using aqueous fruit peel extract of *Citrus aurantifolia*:

Optimization, its characterization and stability test," Sains Malaysiana, vol. 53, no. 5, pp. 1119–1131, 2024.
9. B. M. Jensen, R. A. Althoff, S. E. Rydberg, E. N. Royster, A. Estep, and S. Huijben, "Topical application bioassay to quantify insecticide toxicity for mosquitoes and fruit flies," Journal of Visualized Experiments, no. 179, 2022.
10. R. A. Althoff and S. Huijben, "Comparison of the variability in mortality data generated by CDC bottle bioassay, WHO tube test, and topical application bioassay using *Aedes aegypti* mosquitoes," Parasites and Vectors, vol. 15, no. 1, p. 476, 2022.
11. D. D. Ignareki, G. A. F. Dadji, E. N. Baudelaire, A. Dicko, L. Younoussa, D. W. Wangrawa, *et al*., "Adulticidal activities and synergistic effects of *Citrus aurantiifolia* peels and *Hyptis spicigera* leaves essential oils against *Anopheles gambiae* s.l. (Diptera: Culicidae)," *Int. J. Curr. Sci. Res. Rev.*, vol. 7, no. 3, Mar. 2024, doi: 10.47191/ijcsrr/V7-i3-53.
12. P. Wu, X. Tang, R. Jian, J. Li, M. Lin, H. Dai, *et al.*, "Chemical composition, antimicrobial and insecticidal activities of essential oils of discarded perfume lemon and leaves (*Citrus limon* (L.) Burm. F.) as possible sources of functional botanical agents," *Front. Chem.*, vol. 9, p. 679116, 2021, doi: 10.3389/fchem.2021.679116.
13. I. Pinzaru et al., "Stable PEG-coated silver nanoparticles – A comprehensive toxicological profile," *Food Chem. Toxicol.*, vol. 111, pp. 546–556, 2018, doi: 10.1016/j.fct.2017.11.051.
14. K. Veerakumar, M. Govindarajan, M. Rajeswary, and U. Muthukumaran, "Low-cost and eco-friendly green synthesis of silver nanoparticles using *Feronia elephantum* (Rutaceae) against *Culex quinquefasciatus*, *Anopheles stephensi*, and *Aedes aegypti* (Diptera: Culicidae)," *Parasitol. Res.*, vol. 113, no. 5, pp. 1775–1785, 2014, doi: 10.1007/s00436-014-3823-y.
15. U. Muthukumaran, M. Govindarajan, M. Rajeswary, K. Veerakumar, A. Amsath, and K. Muthukumaravel, "Adulticidal activity of synthesized silver nanoparticles using *Chomelia asiatica* Linn. (Family: Rubiaceae) against *Anopheles stephensi*, *Aedes aegypti* and *Culex quinquefasciatus* (Diptera: Culicidae)," *Int. J. Zool. Appl. Biosci.*, vol. 1, no. 2, pp. 118–129, 2016.
16. A. R. Pintong, S. Ampawong, N. Komalamisra, P. Sriwichai, S. Popruk, and J. Ruangsittichai, "Insecticidal and histopathological effects of *Ageratum conyzoides* weed extracts against dengue vector, *Aedes aegypti*," *Insects*, vol. 11, no. 4, p. 224, 2020, doi: 10.3390/insects11040224
17. S. Mursiti, N. A. Lestari, Z. Febriana, Y. M. Rosanti, and T. W. Ningsih, "The activity of D-limonene from sweet orange peel (*Citrus sinensis* L.) extract as a natural insecticide controller of bedbugs (*Cimex cimicidae*)," *Orient. J. Chem.*, vol. 35, no. 4, pp. 1420–1425, 2019.
18. S. A. Muhammad, I. Muhammad, and A. W. Fatima, "Review on some plants as bio-pesticides," *Int. J. Contemp. Res. Rev.*, vol. 8, no. 7, pp. 20186–20191, 2017.76, 2022.
19. S. N. Kane, A. Mishra, and A. K. Dutta, "Enhancement of the stability of silver nanoparticles synthesized using aqueous extract of *Diospyros discolor* Willd. leaves using polyvinyl alcohol," *J. Phys.: Conf. Ser.*, vol. 755, no. 1, 2016, doi: 10.1088/1742-6596/755/1/011001.
20. S. M. Farouk et al., "Biosynthesis and characterization of silver nanoparticles from *Punica granatum* peel waste and its application to inhibit foodborne pathogens," *Sci. Rep.*, vol. 13, no. 1, p. 19469, 2023.

21. A. B. Seabra and N. Durán, "Nanotoxicology of metal oxide nanoparticles," Metals, vol. 5, no. 2, pp. 934–975, 2015.
22. A. Nel, T. Xia, L. Mädler, and N. Li, "Toxic potential of materials at the nanolevel," Science, vol. 312, pp. 622–627, 2006.
23. A. Vogt, B. Combadiere, S. Hadam, K. M. Stieler, J. Lademann, H. Schaefer, et al., "40 nm, but not 750 or 1,500 nm, nanoparticles enter epidermal CD1a+ cells after transcutaneous application on human skin," Journal of Investigative Dermatology, vol. 126, no. 6, pp. 1316–1322, 2006.
24. B. Sundararajan and B. D. Ranjitha Kumari, "Novel synthesis of gold nanoparticles using *Artemisia vulgaris* L. leaf extract and their efficacy of larvicidal activity against dengue fever vector *Aedes aegypti* L.," Journal of Trace Elements in Medicine and Biology, vol. 43, pp. 187–196, 2017.
25. P. Filipe, J. N. Silva, R. Silva, J. L. Cirne De Castro, M. Marques Gomes, L. C. Alves, et al., "Stratum corneum is an effective barrier to TiO2 and ZnO nanoparticle percutaneous absorption," Skin Pharmacology Physiology, vol. 22, no. 5, pp. 266–275, 2009.
26. R. M. Azmy, E. G. E. El Gohary, D. A. M. Salem, M. A. Abdou, M. S. Salama, D. M. Mahmoud, "Biochemical and histopathological effect of the essential oil of *Citrus sinensis* (L.) Osbeck on larvae of *Culex pipiens* Linnaeus, 1758 (Diptera: Culicidae)," Aquatic Insects, vol. 42, no. 1, pp. 78–90, 2021.
27. J. W. S. Pringle, "The excitation and contraction of the flight muscles of insects," The Journal of Physiology, vol. 108, no. 2, pp. 226–232, 1949.
28. J. F. V. Vincent and U. G. K. Wegst, "Design and mechanical properties of insect cuticle," Arthropod Structure and Development, vol. 33, no. 3, pp. 187–199, 2004.
29. R. Chapman, The Insects: Structure and Function. Cambridge University Press. 1998.
30. A. Thakre, G. Zore, S. Kodgire, R. Kazi, S. Mulange, R. Patil, et al., "Limonene inhibits *Candida albicans* growth by inducing apoptosis," Medical Mycology, vol. 56, no. 5, pp. 565–578, 2018.
31. G. W. Hou and T. Huang, "Essential oils as promising treatments for treating *Candida albicans* infections: research progress, mechanisms, and clinical applications," Frontiers in Pharmacology, vol. 15, 2024.
32. S. Burt, "Essential oils: Their antibacterial properties and potential applications in foods - A review," International Journal of Food Microbiology, vol. 94, pp. 223–253, 2004.
33. H. J. D. Dorman and S. G. Deans, "Antimicrobial agents from plants: antibacterial activity of plant volatile oils," Journal of Applied Microbiology, vol. 88, 2000.
34. M. K. Rai, S. D. Deshmukh, A. P. Ingle, and A. K. Gade, "Silver nanoparticles: The powerful nanoweapon against multidrug-resistant bacteria," Journal of Applied Microbiology, vol. 112, pp. 841–852, 2012.
35. L. Rizzello and P. P. Pompa, "Nanosilver-based antibacterial drugs and devices: Mechanisms, methodological drawbacks, and guidelines," Chemical Society Reviews, vol. 143, pp. 1501–1518, 2014.
36. M. C. D. Niluxsshun, K. Masilamani, and U. Mathiventhan, "Green synthesis of silver nanoparticles from the extracts of fruit peel of *Citrus tangerina*, *Citrus sinensis*, and *Citrus limon* for antibacterial activities," Bioinorganic Chemistry and Applications, vol. 2021, 2021.
37. C. Huo, M. Khoshnamvand, P. Liu, C. G. Yuan, and W. Cao, "Eco-friendly

approach for biosynthesis of silver nanoparticles using *Citrus maxima* peel extract and their characterization, catalytic, antioxidant and antimicrobial characteristics," Materials Research Express, vol. 6, no. 1, 2019.
38. H. O. Khalifa , A. Oreiby, T. Mohammed, M. A. Abdelhamid, E. N. Sholkamy, H. Hashem, and R. M. Fereig, "Silver nanoparticles as next-generation antimicrobial agents: Mechanisms, challenges, and innovations against multidrug-resistant bacteria," *Front. Cell. Infect. Microbiol.*, vol. 15, p. 1599113, 2025, doi: 10.3389/fcimb.2025.1599113.
39. H. Moreno P., F. da Costa-Issa, A. Rajca-Ferreira, M. Pereira, and T. Kaneko, "Native Brazilian plants against nosocomial infections: A critical review on their potential and the antimicrobial methodology," Current Topics in Medicinal Chemistry, vol. 13, no. 24, pp. 3040–3078, 2013.
40. M. M. Alkhulaifi, J. H. Alshehri, M. A. Alwehaibi, M. A. Awad, N. M. Al-Enazi, N. S. Aldosari, et al., "Green synthesis of silver nanoparticles using *Citrus limon* peels and evaluation of their antibacterial and cytotoxic properties," Saudi Journal of Biological Sciences, vol. 27, no. 12, pp. 3434–3441, 2020.
41. L. Benredjem, "Antibacterial properties of leaves and peels extracts of *Citrus aurantifolia* cultivated in Algeria against multi-drug resistant *Staphylococcus aureus* originating from raw milk," *Trop. J. Nat. Prod. Res.*, vol. 7, no. 10, 2023.
42. Clinical and Laboratory Standards Institute (CLSI), *Performance Standards for Antimicrobial Susceptibility Testing*, CLSI supplement M100, 33rd ed., CLSI, Wayne, PA, USA, 2023.
43. N. Ahmad and S. Sharma, "Green synthesis of silver nanoparticles using extracts of *Ananas comosus*," *Green Sustain. Chem.*, vol. 2, pp. 141–147, 2012, doi: 10.4236/gsc.2012.24020.
44. O. Erdogan, M. Abbak, M. Demirbolat, and F. B. Id, "Green synthesis of AgNPs via *Cynara scolymus* leaf extracts: Characterization and anticancer potential with photodynamic therapy in MCF7 cells," *PLoS ONE*, vol. 14, no. 6, pp. 1–15, 2019.
45. D. Elumalai, M. Hemavathi, C. Vijayalakshmi, and P. Kunyil, "Evaluation of phytosynthesized silver nanoparticles from leaf extracts of *Leucas aspera* and *Hyptis suaveolens* and their larvicidal activity against malaria, dengue and filariasis vectors," *Parasite Epidemiol. Control*, vol. 2, no. 4, pp. 15–26, 2017, doi: 10.1016/j.parepi.2017.09.001.
46. M. Carmalita, D. Niluxsshun, K. Masilamani, and U. Mathiventhan, "Green synthesis of silver nanoparticles from fruit peel extracts of *Citrus tangerina*, *Citrus sinensis*, and *Citrus limon* for antibacterial activities," *Bioinorg. Chem. Appl.*, 2021.
47. S. Kaviya, J. Santhanalakshmi, and V. B., "Green synthesis of silver nanoparticles using *Polyalthia longifolia* leaf extract along with D-sorbitol: Study of antibacterial activity," *J. Nanotechnol.*, 2011.
48. N. S. Jalani et al., "Biosynthesis of silver nanoparticles using *Citrus grandis* peel extract," *Malays. J. Anal. Sci.*, vol. 22, no. 4, pp. 676–683, 2018, doi: 10.17576/mjas-2018-2204-14.
49. F. Eker, E. Akdaşçi, H. Duman, M. Bechelany, and S. Karav, "Green synthesis of silver nanoparticles using plant extracts: A comprehensive review of physicochemical properties and multifunctional applications," *Int. J. Mol. Sci.*, vol. 26, no. 13, p. 6222, 2025.
50. V. Sivasakthi et al., "Characterization of silver nanoparticles using *Ixora brachiata* Roxb. and its biological

application," *Curr. Res. Green Sustain. Chem.*, vol. 5, 2022, doi: 10.1016/j.crgsc.2021.100257.
51. H. K. Ardani et al., "Enhancement of the stability of silver nanoparticles synthesized using aqueous extract of *Diospyros discolor* Willd. leaves using polyvinyl alcohol," *IOP Conf. Ser.: Mater. Sci. Eng.*, vol. 188, 2017, doi: 10.1088/1757-899X/188/1/012056.
52. N. Tarannum and Y. K. Gautam, "Facile green synthesis and applications of silver nanoparticles: A state-of-the-art review," *RSC Adv.*, vol. 9, no. 60, pp. 34926–34948, 2019.
53. K. Ranoszek-Soliwoda et al., "The synthesis of monodisperse silver nanoparticles with plant extracts," *Colloids Surf. B Biointerfaces*, vol. 177, pp. 19–24, 2019.
54. L. Mafhala et al., "Antibacterial and cytotoxicity activity of green synthesized silver nanoparticles using aqueous extract of naartjie (*Citrus unshiu*) fruit peels," *Emerg. Contam.*, vol. 10, no. 4, p. 100348, 2024.
55. N. Stozhko et al., "Green silver nanoparticles: Plant-extract-mediated synthesis, optical and electrochemical properties," *Physchem*, vol. 4, no. 4, pp. 402–419, 2024.
56. Y. Khane et al., "Green synthesis of silver nanoparticles using aqueous *Citrus limon* zest extract: Characterization and evaluation of their antioxidant and antimicrobial properties," *Nanomaterials*, vol. 12, no. 12, p. 2013, 2022.
57. A. W. Qing, K. Chen, Y. Wang, X. Liu, and M. Lu, "Green synthesis of silver nanoparticles by waste tea extract and degradation of organic dye in the absence and presence of H_2O_2," *Appl. Surf. Sci.*, 2017, doi: 10.1016/j.apsusc.2017.07.007.
58. J. W. Gong, M. M. Nadzir, and K. Rangasamy, "Green synthesis of silver particles using *Citrus microcarpa* peel extract," *Malays. J. Anal. Sci.*, vol. 24, no. 5, pp. 791–799, 2020.
59. B. Mickky et al., "Orange peel-mediated synthesis of silver nanoparticles with antioxidant and antitumor activities," *BMC Biotechnol.*, vol. 24, no. 1, p. 66, 2024.
60. K. Nahar et al., "Green synthesis of silver nanoparticles from *Citrus sinensis* peel extract and its antibacterial potential," *Asian J. Green Chem.*, vol. 5, pp. 135–150, 2021, doi: 10.22034/ajgc.2021.113966.
61. A. Shudeer et al., "Nanotechnology in insect pest management: Advances, challenges, and future perspectives," *Int. J. Adv. Biochem. Res.*, vol. 8, SP-9, pp. 20–31, 2024, doi: 10.33545/26174693.2024.v8.i9Sa.2046.
62. X. F. Zhang, Z. G. Liu, W. Shen, and S. Gurunathan, "Silver nanoparticles: Synthesis, characterization, properties, applications, and therapeutic approaches," *Int. J. Mol. Sci.*, vol. 17, no. 9, 2016, doi: 10.3390/ijms17091534.
63. R. Yadav and S. Preet, "Comparative assessment of green and chemically synthesized glutathione capped silver nanoparticles for antioxidant, mosquito larvicidal and eco-toxicological activities," *Sci. Rep.*, vol. 13, no. 1, pp. 1–13, 2023, doi: 10.1038/s41598-023-35249-7.
64. B. Khan, M. Nawaz, R. Hussain, G. J. Price, M. F. Warsi, and M. Waseem, "Enhanced antibacterial activity of size-controlled silver and polyethylene glycol functionalized silver nanoparticles," *Chem. Pap.*, vol. 75, pp. 743–752, 2021, doi: 10.1007/s11696-020-01335-7.
65. M. N. Fernández, R. Muñoz-Olivas, and J. L. Luque-Garcia, "SILAC-based quantitative proteomics identifies size-dependent molecular mechanisms involved in silver nanoparticles-induced toxicity," *Nanotoxicology*, vol. 13, pp. 812–826, 2019, doi: 10.1080/17435390.2019.1579374.

66. B. Khodashenas and H. R. Ghorbani, “Synthesis of silver nanoparticles with different shapes,” *Arab. J. Chem.*, vol. 12, pp. 1823–1838, 2019, doi: 10.1016/j.arabjc.2014.12.014.
67. J. Y. Cheon, S. J. Kim, Y. H. Rhee, O. H. Kwon, and W. H. Park, “Shape-dependent antimicrobial activities of silver nanoparticles,” *Int. J. Nanomedicine*, vol. 14, pp. 2773–2780, 2019, doi: 10.2147/IJN.S196472.
68. D. Franco, G. Calabrese, S. P. Guglielmino, and S. Conoci, “Metal-based nanoparticles: Antibacterial mechanisms and biomedical applications,” *Microorganisms*, vol. 10, p. 1778, 2022, doi: 10.3390/microorganisms10091778.

iSAMN 2025

9TH INTERNATIONAL SYMPOSIUM ON ADVANCED MATERIALS & NANOTECHNOLOGY

Organised by:
Institute of Nanoscience and Nanotechnology (ION2),
Universiti Putra Malaysia (UPM).

eISSN 2811-4655
9 772811 465002

Agriculture • Innovation • Life
With Knowledge We Serve

upm.edu.my